Structural characterization of
α-synuclein aggregates seeded by patient material

Dissertation
to acquire the doctoral degree in mathematics and natural sciences
'Doctor rerum naturalium'
at the Georg-August-Universität Göttingen

in the doctoral program of Biology
at the Georg-August University School of Science (GAUSS)

participating in the International PhD Program in
Molecular Biosciences and Biomedicine
of the Universidad Nacional de Rosario in Argentina
and the Georg-August-Universität Göttingen

Submitted by

Timo Strohäker

from Herrenberg

Göttingen, 2018

Thesis Committee

Prof. Dr. Markus Zweckstetter
Structure Determination of Proteins Using NMR, Max-Planck-Institute for Biophysical Chemistry, Göttingen
Translational Structural Biology in Dementia, German Center for Neurodegenerative Diseases, Göttingen

Prof. Dr. Tiago Outeiro
Department of Experimental Neurodegeneration, University Medical Center (UMG) Göttingen

Dr. Claudio Fernández
Max-Planck Laboratory for Structural Biology, Chemistry and Molecular Biophysics of Rosario (LMPbioR), CONICET IIDEFAR, Universidad Nacional de Rosario (UNR), Rosario (Argentina)

Members of the Examination Board

Reviewer: Prof. Dr. Markus Zweckstetter
Second Reviewer: Dr. Claudio Fernández

Further members of the Examination Board:

Prof. Dr. Holger Stark
Department Stark, Structural Dynamics, Max-Planck-Institute for Biophysical Chemistry, Göttingen

Dr. Mauricio Menacho Márquez
Max-Planck Laboratory for Structural Biology, Chemistry and Molecular Biophysics of Rosario (LMPbioR), CONICET IIDEFAR, Universidad Nacional de Rosario (UNR), Rosario (Argentina)

Dr. Sebastian Kügler
Department of Neurology, Viral Vectors Lab, University Medical Center (UMG) Göttingen

Date of the oral examination: **December 14, 2018**

Affidavit

I hereby declare that the doctoral thesis entitled "Structural characterization of α-synuclein aggregates seeded by patient material" has been written independently, with no other sources and aids than quoted.

……………………..
Timo Strohäker

Göttingen, November 2018

Acknowledgements

I would like to thank Prof. Markus Zweckstetter for giving me the chance to work on this exciting and challenging research project and for the constant help and guidance that he has provided me with at all stages of my doctoral studies as well as his openness and support to let me join the binational doctoral program. It was more than a pleasure to work in such an international and diverse research group having access to outstanding equipment and addressing highly relevant scientific questions.

I would also like to thank Dr. Claudio Fernández for his supervision and scientific input as well as the extraordinary research experience that I enjoyed during my stay at his group at the Max Planck Laboratory of Rosario (LMPbioR) in Argentina. My time in this beautiful country was something truly special. I would also like to thank him for his extraordinary commitment to solving all obstacles related to the exchange program.

Thank goes as well to Prof. Tiago Outeiro and Prof. Holger Stark for their scientific advice and support.

In addition, I would like to show my gratitude to Prof. Seung-Jae Lee and Dr. Byung Chul Jung of the Department of Biomedical Sciences of the Seoul National University College of Medicine, Prof. Marina Bennati and Dr. Shu-Hao Liou of the EPR spectroscopy group of the MPIBPC in Göttingen, Dr. Stefan Becker, Karin Giller and Kerstin Overkamp of the Department of NMR-based Structural Biology of the MPIBPC in Göttingen as well as Prof. Glenda M. Halliday and Prof. Woojin Kim of the Brain and Mind Centre of the University of Sidney for their scientific contributions.

A very big thank goes to all these brilliant, interesting and highly skilled people that I have met during all those years and that I have had the luck to share some time with. I feel deeply thankful to all of you. Your help and instructions, the constant support, the fruitful scientific discussions, your encouragements and recommendations altogether have enabled me to achieve my goals and shaped me during the time as a doctoral student and as a person in general. Thank you for making my life inside and outside the lab so worthwhile. I would like to specially mention Hessam, Filippo, Andrés B., Taekyung, Javier, Yunior, Hari, Piotr, Garima, Martin, Aldo, Frederik, Luis, Adriana, Juan Carlos, Dirk, Kris, Mariusz and Lukasz, Sol, Conny, Alain, Antonia, Susmitha, Pijush, Marija, Maria, Tina, Mauge, Caterina, Gonzalo, Marco, Andrés T. and Franco.

Abstract

Neurodegenerative diseases share a common underlying pathologic hallmark, the appearance of insoluble protein aggregates in diverse tissues of the nervous system. For many neurodegenerative diseases a common temporal and spatial spreading of the pathology is proposed in analogy to prion disease and discussed under the term "prion-like". For many diseases the major component of the insoluble protein aggregates is known and aggregation into higher molecular weight amyloid fibrils with intermolecular β-sheet rich cores can be studied *in vitro*. The aggregation process involves the templated misfolding and aggregation of native monomeric proteins, involving severe conformational changes.

An important family of neurodegenerative diseases is caused by the misfolding and aggregation of the protein α-synuclein, the so-called synucleinopathies. α-synuclein, which *in vivo* forms disease-specifically the main component of intracellular inclusions such as Lewy bodies in neurons and cytoplasmatic inclusions in glial cells, undergoes *in vitro* dramatic conformational changes from a monomeric intrinsically disordered state over transient oligomeric β-sheet rich species into highly ordered α-synuclein fibrils.

α-synuclein pathology in patients is diverse and there are clinically distinct disease entities with defined pathologic phenotypes among those Parkinson's disease (PD), dementia with Lewy bodies (DLB) and multiple system atrophy (MSA) are the best characterized. Similar to prion diseases, key differences within the broad clinical representation of synucleinopathies are thought to be structurally encoded by distinct protein aggregate conformations, referred to as α-synuclein polymorphs.

The aim of the study was to amplify α-synuclein aggregates from brain extracts of patients thoroughly diagnosed on the basis of the molecular pathology as well as the clinical symptoms as PD, DLB and MSA, using the established protocol of protein misfolding cyclic amplification (PMCA). A combination of hydrogen-deuterium (HD) exchange coupled to nuclear magnetic resonance (NMR) spectroscopy, electron paramagnetic resonance (EPR) and the specific binding of fluorescent probes to amyloid fibrils was chosen to obtain single-residue resolution of the conformational properties of brain-extract seeded α-synuclein fibrils. The same approach was also applied to two well-characterized *in vitro* α-synuclein polymorphs, their aggregation was performed in the absence of brain extract seeds following published aggregation procedures and they acted as internal references for benchmarking the methodological approach. On the other hand, the availability of a high-resolution cryo-electron

microscopy model of the fibrillar core for one of the *in vitro* α-synuclein polymorphs obtained under high salt conditions, allowed direct correlation of the residue-specific conformational restraints to a structural model, both for *in vitro* polymorphs of α-synuclein as well as brain-extract amplified α-synuclein fibrils of PD, MSA and DLB.

Distinct highly ordered conformational features of *in vitro* α-synuclein fibrils were successfully reproduced, detecting solvent-protected residues with high precision and in agreement with published data. In contrast, α-synuclein fibrils amplified from brain extracts were more flexible and differed structurally from *in vitro* fibrils. Hydrogen-deuterium exchange coupled to NMR spectroscopy identified a common solvent-protected core shared among all patient brain derived α-synuclein fibrils for the synucleinopathies PD, MSA and DLB. The solvent-protected fibrillar core was formed by the most hydrophobic residues of α-synuclein. Outside the common core structure, α-synuclein fibrils derived from brain extracts differed disease-specifically in the conformation. Residue-specific conformational differences in core-flanking residues of α-synuclein as well as in defined N-terminal regions were observed.

This study establishes a strong correlation between α-synuclein aggregate structure and the disease phenotype for the synucleinopathies Parkinson's disease, Dementia with Lewy bodies and multiple system atrophy and the data provide further insight in "prion-like" features of neurodegenerative diseases in general and synucleinopathies in particular. The work presented here is a step forward towards the understanding of α-synuclein pathology and hopefully contributes to improved disease diagnosis and treatment of synucleinopathies.

Publications

Following publications appeared in peer-reviewed journals as a doctoral student including personal contributions as stated in the respective publications.

Moree, B. *et al.*
Small Molecules Detected by Second-Harmonic Generation Modulate the Conformation of Monomeric alpha-Synuclein and Reduce Its Aggregation in Cells.
J Biol Chem **290**, 27582-27593, (2015)

Gentile, I. *et al.*
Interaction of Cu(i) with the Met-X3-Met motif of alpha-synuclein: binding ligands, affinity and structural features.
Metallomics **10**, 1383-1389, (2018).

Table of Contents

Index of Tables

Table of Figures

Abbreviations

aSyn	N-terminally acetylated α-synuclein
CJD	Creutzfeldt-Jakob disease
DLB	Dementia with Lewy bodies
EM	Electron microscopy
EPR	Electron paramagnetic resonance
FSB	(E,E)-1-fluoro-2,5-bis(3-hydroxycarbonyl-4-hydroxy) styrylbenzene
GCI	Glial cytoplasmatic inclusions
HD	Hydrogen-deuterium
hsAsyn	High salt aSyn polymorph (50 mM Tris-HCl, pH 7.5, 150 mM KCl, 0.02% NaN_3)
HSQC	Heteronuclear single quantum coherence/correlation
IDP	Intrinsically disordered protein
lsAsyn	Low salt aSyn polymorph (5 mM Tris-HCl, pH 7.5, 0.02% NaN_3)
MSA	Multiple system atrophy
MTSL	S-(1-oxyl-2,2,5,5-tetramethyl-2,5-dihydro-1H-pyrrol-3-yl) methyl methanesulfonothioate
NAC	Non-Aβ component
NMR	Nuclear magnetic resonance
NTFs	Neurofibrillary tangles of tau protein
NUS	Non-uniform sampling
PAGE	Polyacrylamide gel electrophoresis
PD	Parkinson's disease
PFF	Pre-formed fibrils
PHF	Paired-helical filaments of tau in AD
PiD	Pick's disease, also called frontotemporal dementia
PMCA	Protein misfolding cyclic amplification
PrP	Prion protein
QELS	Quasielastic light scattering
SDS	Sodium dodecyl sulfate
SEC	Size-exclusion chromatography
SF	Straight filaments of tau in AD
SN	Supernatant
UC	Ultracentrifugation

1   Introduction

1.1   Neurodegenerative disorders

Age-related[1] neurodegenerative disorders form a class of heterogeneous diseases, differing in pathology and clinical symptoms. The common hallmark and class-defining pathology is the intra- and extracellular aggregation of particular proteins in the human brain (Table 1). They are therefore also named *proteinopathies*. Figure 1-1 shows three examples of aggregated protein deposits. These protein deposits are also often referred to as *amyloids* in analogy to the polysaccharide amylose[2]. Amyloids as well as starch reacts positively with iodine, that allowed histological staining early on.

Neurodegenerative disease	Amyloidogenic proteins
Parkinson's disease[3]	α-synuclein[4]
Alzheimer's disease[5]	$A\beta$[6], tau[7]
Amyotrophic lateral sclerosis[8]	TDP-43[9], SOD1[10]
Huntington's disease[11]	Huntingtin protein[12]
Creutzfeldt-Jakob disease[13]	Prion protein[14]

Table 1. Overview of common neurodegenerative disorders and the disease defining amyloidogenic proteins.
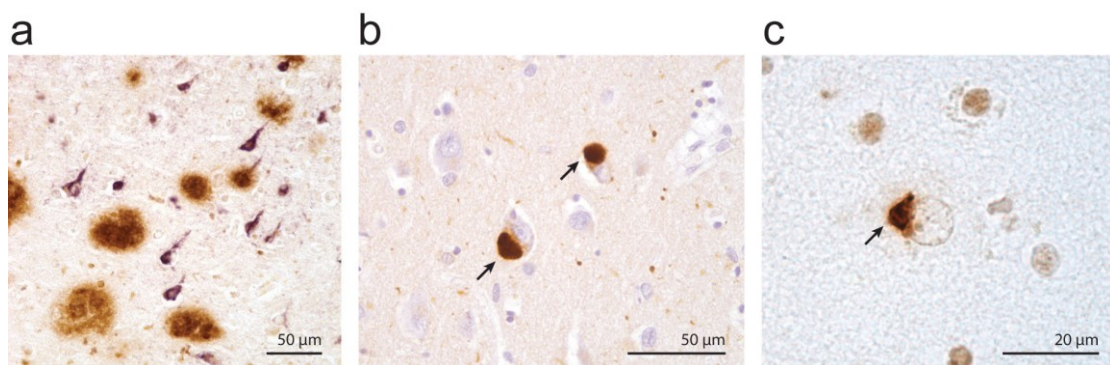
Figure 1-1. Antibody staining of hallmark protein deposits.
(a) In brown extracellular $A\beta$ plaques and in purple intracellular neurofibrillary tau tangles of AD. (b) Lewy bodies (arrow) common in PD and DLB. (c) TDP-43 (arrow) deposits of ALS, taken from Walker LC[15].

Neurodegeneration is a complex multifactorial interplay[16] that differs from one disease to the other, but it always manifests in the loss of neuronal and non-neuronal glia cells due to cell death in the brain over time. In an aging society with growing life expectancy, age-related neurodegenerative disorders have become a heavy burden for the health care systems and they are a major public health priority for policy makers worldwide[17].

1.2 α-Synuclein

The human protein α-synuclein (aSyn) is 140 amino acids long and has a molecular weight of 14.46 kDa. The human gene *SNCA* is located on the long arm of chromosome 4 at position 21[18]. The protein was first described by Maroteaux et al. in 1988[19] studying the electric organ of *Torpedo californica*. They already showed high similarities to a 140 amino acid sequence in a cDNA library of rat brain. The name *synuclein* was derived from its apparent localization in the presynaptic nerve ends and the nucleus. Very quickly a homologue was purified and characterized from bovine brain[20,21] only occurring in synapses around neuronal cells and not in glial cells.

Ueda et al.[22] then established the first link to neurodegeneration. They identified two short peptide fragments X and Y (X: N-$_{61}$EQVTNVGGAVVTGVTAVAQK$_{80}$-C, Y: N-$_{81}$TVEGAGSTAAATGFV$_{95}$-C) in purified amyloids from the frontal cortex of an AD patient. With the sequence information of the peptides Ueda et al. were able to amplify the full-length aSyn DNA sequence from a human fetal brain cDNA library. The region spanned by the two fragments is therefore called non-Aβ component (NAC). Jakes et al.[23] and Ji et al.[24] completed the synuclein family by identifying β- and γ-synuclein respectively. β- and γ-synuclein are lacking the NAC region and are not known to form amyloids *in vivo*. There are two relevant point mutations of β-synuclein that are associated with dementia with Lewy bodies and might be disease relevant[25,26].

1.2.1   Structure

Under native functional conditions aSyn is considered to be a monomeric intrinsically disordered protein (IDP)[27,28,29]. The protein however maintains long-range tertiary interactions[30,31] and higher compactness than a random coil ensemble. On the sequence level, the protein can be divided into three regions, an amphipathic N-terminus (residues 1-60), a hydrophobic central region (NAC region, residues 61-95) and an acidic C-terminal region (residues 96-140) that is rich in prolines (Figure 1-2). Although aSyn is highly dynamic in solution and can exchange between a large number of conformations, the protein acquires α-helical secondary structure upon interaction with phospholipid bilayers and micelles mainly driven by the amphipathic N-terminus. In the case of SDS micelles aSyn forms a bent-helix[32] (Figure 1-2b), whereas with phospholipid bilayers it forms an extended α-helix[33] orchestrating the curvature of biological membranes.

a

```
      1  MDVFMKGLSK AKEGVVAAAE KTKQGVAEAA GKTKEGVLYV GSKTKEGVVH GVATVAEKTK
```



```
     61  EQVTNVGGAV VTGVTAVAQK TVEGAGSIAA ATGFVKKDQL GKNEEGAPQE GILEDMPVDP
```

```
    121  DNEAYEMPSE EGYQDYEPEA
```

b

NAC region

acidic proline-rich region

amphipathic N-terminal region
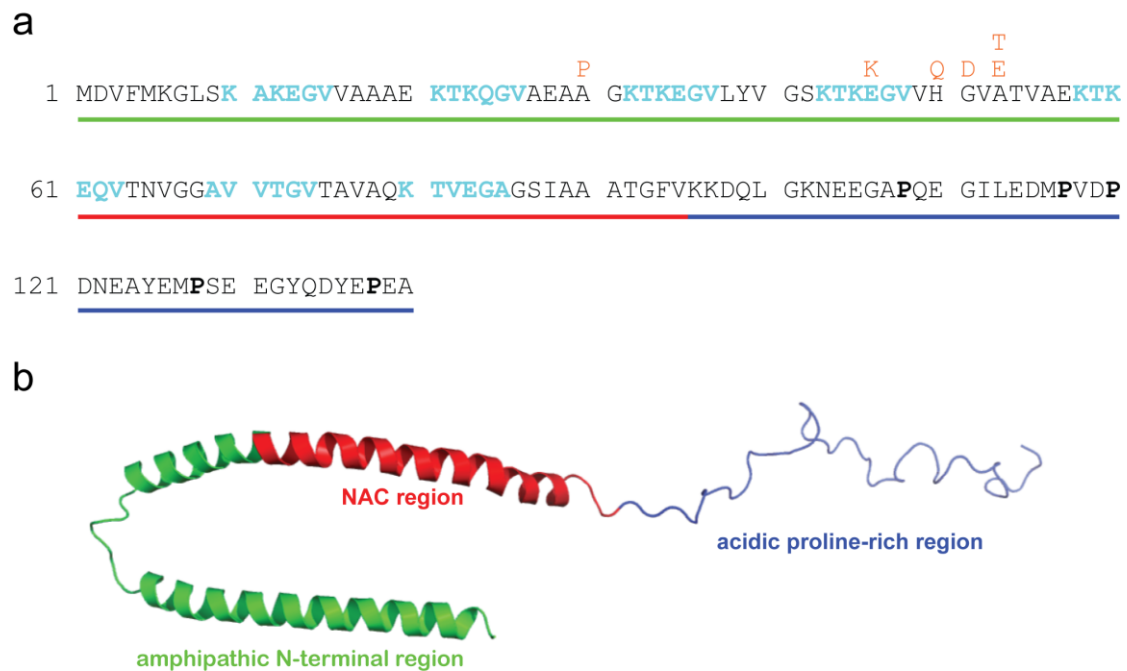
Figure 1-2. aSyn sequence and structural properties.

(a) aSyn sequence, amphipathic N-terminal region underlined in green, NAC region in red and acidic proline-rich region in blue. In orange mutations associated with familial forms of synucleinopathies are indicated: A30P, E46K, H50Q, G51D, A53E and A53T. The proline residues are indicated by bold letters, the KTKEGV-motif of the seven 11-residue imperfect repeat regions is shown in cyan. (b) Cartoon representation of aSyn bound to SDS micelles, curved α-helix V3-V37 and K45-T92, PDB: 1XQ8.

Of special importance in the context of synucleinopathies, aSyn can also form amyloid fibrils[4]. Amyloid fibrils are highly structured and thermodynamically stable[34] protein assemblies, that consist of intermolecular β-strands of polypeptide chains arranged perpendicular to the fibril axis and stacked by hydrogen bonding with a spacing of 4.7 Å[35], this arrangement is also named the cross-β structure[36,37]. In *in vitro* studies the interconversion of aSyn into amyloid fibrils has been extensively studied using a wide variety of aggregation conditions with varying pH[38], ionic strength, temperature[39], concentration, additives[40] and stimulation procedures. Figure 1-3a summarizes the different structural steps. Monomeric aSyn is converted into mature fibrils, also called preformed fibrils (PFF), involving the formation of transient on-pathway oligomers[41] with β-sheet content. *In vivo* it is much more challenging to follow aSyn aggregation over time (Figure 1-3b). Physiological monomeric aSyn can be detected in the terminal ends of synapses. Granular structures might represent oligomeric or early fibrillar states of synuclein based on cell culture experiments, whereas complex structures

such as pale bodies and Lewy bodies can only be observed in patients, however a simplified mouse model for pale bodies exists[42].
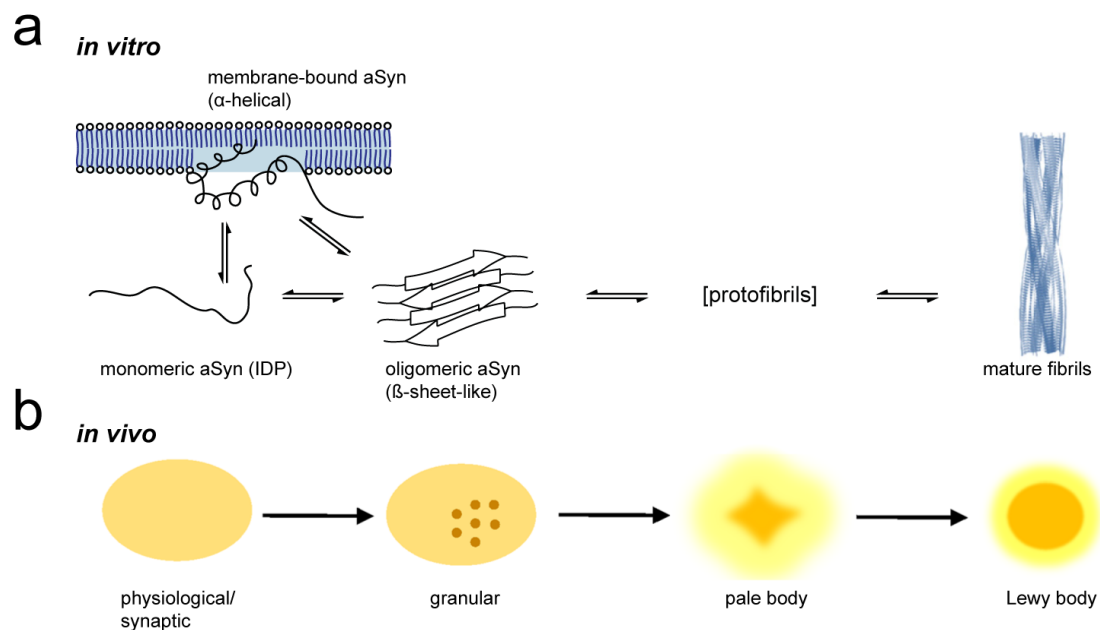
Figure 1-3. Aggregation of aSyn *in vitro* and *in vivo*.

(a) *In vitro* aggregation scheme of monomeric aSyn. (b) Detectable morphological species *in vivo* by histological antibody staining. Figure adapted from these publications[43,44,45].

1.2.2 Functional aspects

The α-helical state of aSyn has been associated with its potential biological function in the presynaptic terminals that is until today only poorly understood. There is evidence, that aSyn-membrane interactions are crucial in synaptic transmission[46] as well as the cycling of synaptic vesicles via endocytosis[47]. An important finding potentially related to the biological function of aSyn was obtained by George et al.[48] on the bird species zebra finch, where synuclein mRNA and protein expression levels are downregulated over a period during development when the birds develop their final adult song, while the levels stay low during adult life in comparison to brain regions not involved in song control. The authors correlated their findings with neuronal plasticity. Directly related to aSyn's function in the presynaptic terminals is its role as a member in the assembly of the SNARE-complex, where it acts as a noncanonical chaperone[49]. This interaction is believed to happen through protein-protein interactions of aSyn's acidic C-terminus with synaptobrevin-2/VAMP2 while interacting with phospholipid bilayers of biological membranes through its N-terminus[50]. Burré et al.[50] also showed that aSyn undergoes oligomerization bound to membranes and that this step is crucial for the supposed chaperone function in membrane fusion and exocytosis.

1.3 Synucleinopathies

The term *α-synucleinopathies* or also just *synucleinopathies* defines all members of a family of proteinopathies sharing as a common feature intracellular protein aggregates of aSyn[51,52] in neuronal and/or glial cells. There are two major pathologies: on one hand Lewy-related α-synuclein pathologies (LRP) comprising Lewy bodies and Lewy neurites and on the other hand glial cytoplasmatic inclusions (GCI)[53,54]. Lewy FH was the first to describe these inclusions in brain sections of PD patients in 1912 and Tretiakoff C later on in 1919 proved their presence in the *substantia nigra*[55] naming these structures in Lewy's honor. Another key finding is the presence of Lewy bodies in the cortex[56]. Pale bodies are considered precursors of Lewy bodies[57].
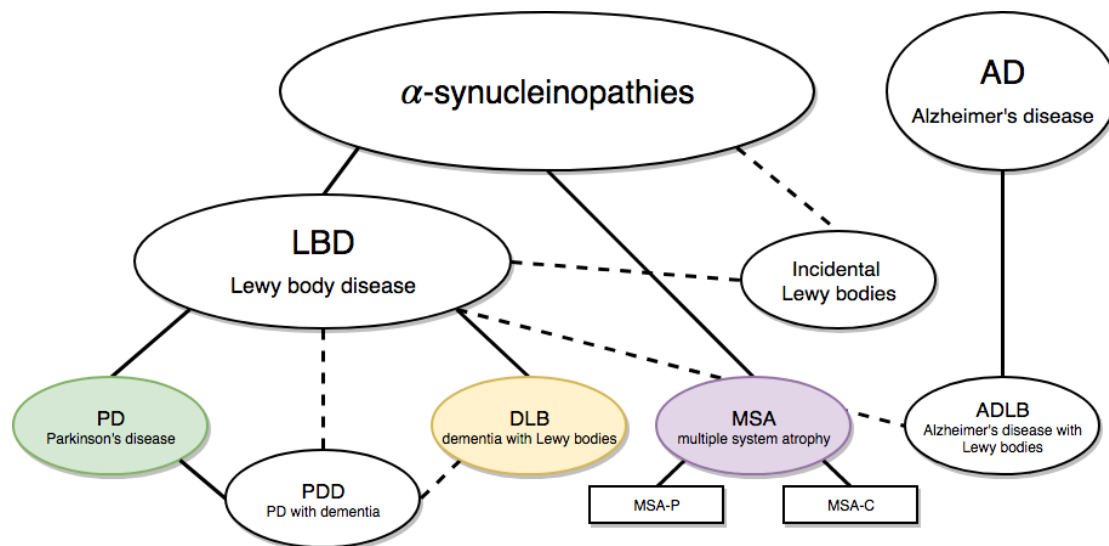
Figure 1-4. Preliminary classification of synucleinopathies.
Preliminary classification of synucleinopathies and associated diseases using information provided by Alafuzoff et al.[58] and McCann et al.[59].
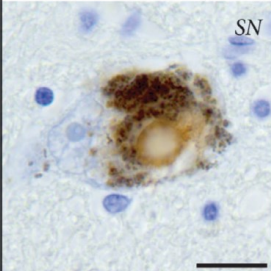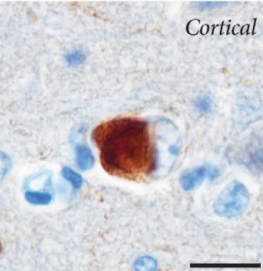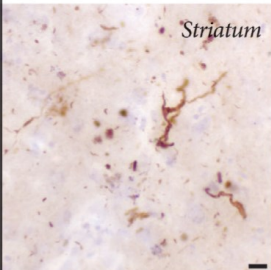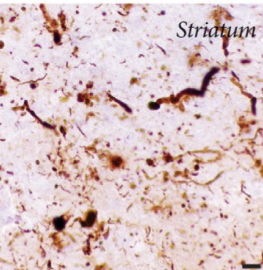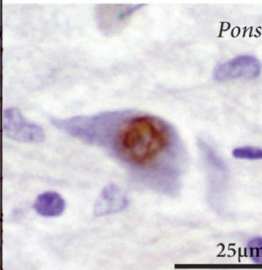
Lewy body composition has been in the focus of research over many years and fibrillar forms of aSyn have been identified as the key element often associated with post-translational modifications such as phosphorylation[60], mainly residue S129, as well as high levels of aSyn ubiquitination[61] and others. In fact anti-ubiquitin antibodies were used for Lewy body staining before knowing about aSyn's role in synucleinopathies[4]. Importantly Lewy bodies are very diverse in their composition and should not be seen as pure inclusions of fibrillar synuclein. Indeed, more than 90 molecular components[62] have been identified and some studies identified even more possible candidates (~400 proteins[63]), and similar findings have been reported for aSyn inclusions in animal

model systems[42]. To the present day, it is not clear how LRPs and GCIs are associated with toxicity and cell death.

The best medical diagnosis of synucleinopathies still relies on the postmortem examination of defined brain areas using immunohistochemical techniques. Figure 1-4 shows the different diseases in a hierarchic chart.

Clinical	Parkinson's disease (PD)	Dementia with Lewy bodies (DLB)	Multiple System Atrophy (MSA)
Age of Onset (years)	~60	~70	~60
Duration (years)	~12	~5	6-9
Motor signs	All	Some	All
L-dopa responsive	Yes	Variable	No
Non-motor signs			
Autonomic	Late	Late	Early
Hallucinations	Late	Early	No
Olfactory dysfunction	Early	Early	No
Dementia	Late	Early	No
Main synucleinopathies	NCIs	NCIs	GCIs
	SN	Cortical	Pons
	Neurites	Neurites	NNIs
	Striatum	Striatum	Pons 25μm

Figure 1-5. Hallmark pathologic features of PD, DLB and MSA.

Parkinson's disease (PD), Dementia with Lewy bodies (DLB) and Multiple System Atrophy (MSA). NCI: neuronal cytoplasmatic inclusions, GCI: glial cytoplasmatic inclusions, SN: *substantia nigra*. In green distinct pathologic features are indicated. Taken from McCann et al.[59]

1.3.1 Parkinson's disease

Parkinson's disease (PD) is the second most common age-related neurodegenerative disorder[64] after Alzheimer's disease (AD) affecting 950 individuals per 100,000 in the US[65] which translates approximately in a prevalence rate of 1% in the Western world. A European prevalence study suggests that by the year 2030 between 8.7 and 9.3 million people will be affected by PD[66].

The main clinical criteria for PD diagnosis is the presence of two out of three motor signs: bradykinesia, rigidity and resting tremor[67]. In addition, non-motor symptoms such as sensory impairments, REM sleep disorders, depression, constipation, pain as well as cognitive deterioration can occur, often becoming noticeable before the onset of motor symptoms.

The mutations A30P[68], E46K[69], H50Q[70], G51D[71], A53T[72] and A53E[73] of aSyn are associated with familial forms of PD, as well as SNCA gene duplication[74] and triplication[75]. Most of PD cases are sporadic. Key PD symptoms are directly linked to cell death of pigmented dopaminergic neurons in *substantia nigra* and are signs of dopamine deficiency. Post-mortem LPR in SN are detectable. Depigmentation of the *substantia nigra* can be readily observed in brain autopsy. Some PD patients also develop dementia and for some pathologists it is even classified as a distinct Lewy body disease, Parkinson's disease with dementia (PDD) (Figure 1-4). LPRs do not differ much between PD, PDD and LBD. For correct assessment of the disease type, it is absolutely crucial that in case of PD and PDD, signs of dementia start after the advent of motor symptoms and vice versa of DLB[59].

Besides symptomatic pharmacological therapy of PD[76] by L-DOPA and surgical deep brain stimulation[77], there is down to the present day no cure for the diseases . Thus, further fundamental research is required, in order to better understand and characterize the disease and eventually help the millions of people affected.

1.3.2 Dementia with Lewy bodies

Dementia with Lewy bodies overlaps closely in its pathology with PD. It follows Alzheimer's disease as the most common form of dementia[78]. The worsening of cognitive functions associated with dementia has to precede motor symptoms for at least one year. LBP seems to be more pronounced in the cerebral cortex in comparison to PD (Figure 1-5).

1.3.3 Multiple system atrophy

Multiple system atrophy (MSA) shows two disease subtypes. The first subtype named MSA-P is associated with classical symptoms also occurring in PD such as bradykinesia, tremor, rigidity and postural instability. The second subtype MSA-C affects mainly the cerebellum and the associated functions causing gait and speech problems as well as oculomotor dysfunctions[79]. MSA has a similar onset age as PD, but the survival time is much shorter with patients dying within 6-9 years.[59] The most striking difference appears in the pathology, in MSA unlike any other synucleinopathy, the affected cells are non-neuronal oligodendrocytes of the brain glia and the hallmark feature are aSyn-positive glial cytoplasmatic inclusions (GCI) (Figure 1-5). Currently it is still an open question if the misfolded aSyn is expressed by the oligodendrocytes themselves[80] or if there is a transmission pathway that allows transport of aSyn from neurons to glial cells[81] and equally important what is the conformation of the aSyn species that occur in this neuron-to-glia transmission.

1.3.4 ADLB and others

Lewy body pathology has also been observed in a subpopulation of patients diagnosed with Alzheimer's disease, specially within the amygdala[82]. These cases might represent a distinct pathologic entity or represent mixed-type pathologies of DLB and AD[83], making it difficult to categorize unanimously. In addition, it is known that Lewy bodies occur in asymptomatic patients, which is referred to as "incidental Lewy bodies" in the field. These cases could also represent preclinical stages of true synucleinopathies.

1.4 Prion hypothesis and prion-like behavior of aSyn

1.4.1 Prion disease

The native prion protein (PrP^c) has in humans a length of 253 amino acids[84] and is expressed in vertebrates[85]. The structure of PrP^c is known for mice[86] and sheep[87], it contains a globular C-terminal domain comprised of three α-helices and an intrinsically disordered N-terminus. Native PrP^c can misfold *in vitro* and *in vivo* in a β-sheet rich confirmation forming amyloid fibrils. The misfolded and infectious form of the protein is referred to as PrP^{Sc}, named after the neurodegenerative disease it causes in sheep, scrapie disease. The exact conformation of PrP^{Sc} fibrils is still unknown, but it lacks the α-helical moiety of its native monomeric form[88]. PrP^c can spontaneously change its conformation and convert *de novo* into PrP^{Sc}. PrP^{Sc} has autocatalytic activity and

converts monomeric PrP[c] into PrP[Sc], also referred to as *templated seeding*. In humans it causes Creutzfeldt-Jakob disease (CJD) in two variants with distinct pathology[89], sporadic (sCJD) and familial Creutzfeldt-Jakob disease (fCJD)[90] associated with mutations in the prion gene (*Prnp*).

All prion diseases are transmissible, they are truly communicable[91]. In case of CJD the only reported transmissions were based on the usage of prion-contaminated hormone preparations from human cadavers[92]. There is a third form of CJD, the so called variant CJD (vCJD) that happens to cross-species infection of the cattle prion disease, bovine spongiform encephalopathy (BSE), by consumption of contaminated beef[93]. Genetically distinct PrP[Sc] of cattle causes the aggregation of human PrP[c] into PrP[sc]. The prions of vCJD are biochemically distinct and show a different pathology with increased contagiousness. Transmission among humans via blood transfusions is possible and they conserve the characteristics of vCJD[94]. They are considered a prion strain and differences in pathology seem to be conformationally encoded[15,95] (Figure 1-6).
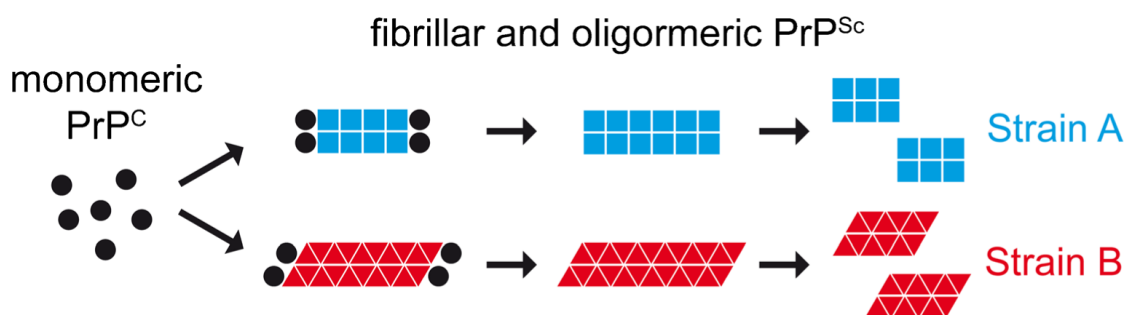
Figure 1-6. Prion disease strain behavior.

Structurally and pathologically distinct population of prion strains causing different prion transmissible diseases. Taken from Tamgüney et al.[96]

1.4.2 Protein misfolding and seeded aggregation

The conversion of monomeric aSyn in the absence of fibrils or oligomers is called *de novo* aggregation. Hashimoto et al.[97] reported for the first time that recombinant aSyn aggregates *in vitro* into amyloid fibrils (Figure 1-3). Wood et al.[98] shortly after showed that the aggregation could be speeded up by the addition of preformed fibrils obtained by *de novo* aggregation. This opened the field for in depth biophysical investigations of aSyn aggregation and the aggregation kinetics, as well as variants of aSyn associated with familial mutations[99]. It is important to point out that aSyn under quiescent conditions does not form fibrils at 37°C and pH 7.4 and stays in solution, shown in detail by Buell et al.[100]. The same group also showed, that the addition of seeds under quiescent conditions leads to fibril elongation, excluding secondary

nucleation processes. In the prion field two techniques were developed to amplify prion strains by converting recombinant PrP^C into PrP^{Sc} with seeds from cellular material[101] named real-time quaking induced conversion[102] (RT-QuIC) and protein misfolding cyclic amplification[103] (PMCA). Both techniques are now established in the synuclein field. RT-QuIC is thoroughly tested on cerebral spine fluid (CSF) of patients[104] for diagnosis purposes. Herva et al. recently improved the PMCA and showed that PMCA end products are bona fide synuclein amyloid fibrils maintaining the structural properties[105]. Jung et al. used brain homogenates of pathologic tissues[106] and also independently showed conservation of structural properties.

1.4.3   Spreading in synucleinopathies

Braak et al. introduced in a milestone research a staging system for AD pathology[107] and applied the methodology later on to PD[108], correcting recently some assumptions on the initial origin in the early phases of the disease[109]. There is also an alternative staging system by McKeith et al.[110] and in addition, Beach et al. proposed modifications to Braak's stages[111].
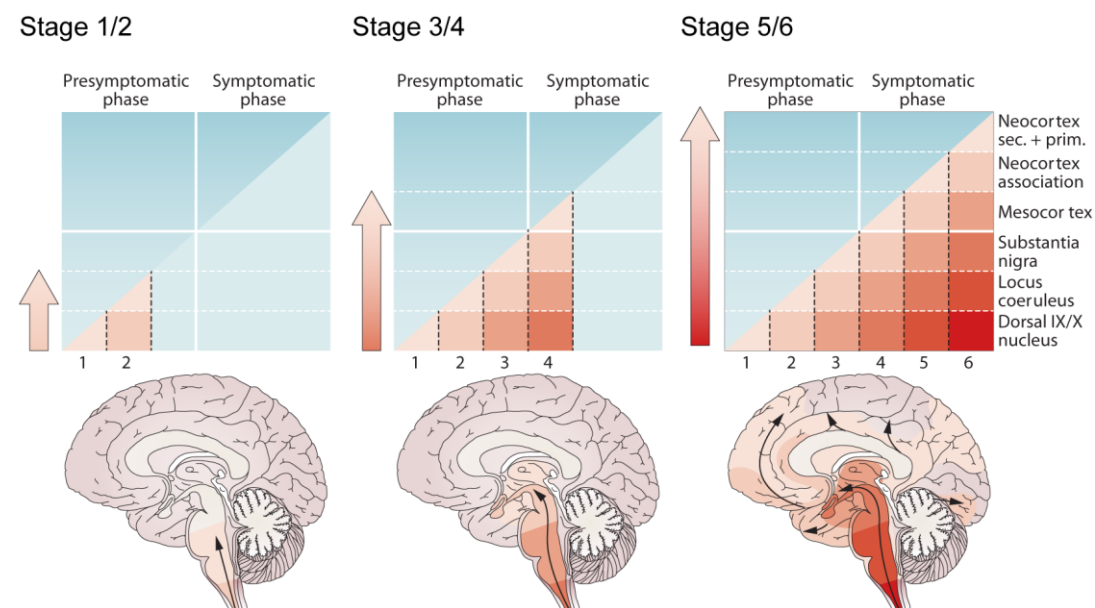
Figure 1-7. Braak's staging of PD pathology.

Arrows indicate temporal disease progression in the central nervous system over anatomically interconnected brain regions, red color indicates severity of PD pathology. Key brain areas are listed in the upper panel. Taken from Goedert et al.[112]

Braak's disease progression model is based on the detailed analysis of individual postmortem brains of PD diagnosed patients, grouping their lesions due to severity and brain regions affected. He could thereby show, that all patients investigated follow a pattern that can be correlated with a temporal progression of PD, starting in the brain stem. The open question remains if the pathology starts independently developing at different time points and/or different velocities or if the pathology travels along connected brain areas and ultimately spreads from cell-to-cell. Inevitably the question arises, what would be the nature of the "pathogen" and what are the routes along which the "pathogen" travels[113]. The best candidate for the pathogen is aSyn itself. For the spreading nature of pathology in neurodegenerative disorders caused by amyloidogenic proteins themselves, the term "prion-like" is established.

Pioneering work of two groups independently showed via postmortem analysis of PD brains, that Lewy body pathology can spread from neuronal tissue of the patients into the newly grafted tissue for patients that received fetal tissue transplants and survived for less than twenty years[114,115].

A plethora of animal model studies, see Table 1 of Steiner et. al[116], were performed where *in vitro* aggregated recombinant aSyn fibrils under different aggregation conditions were applied via intracranial injection into specific brain areas (e.g. *striatum* or *substantia nigra*) of the animal models of choice, mainly in rodent models. Afterwards the affected brain area and neighboring regions were thoroughly investigated and spreading of pathology into distal areas were consistently shown. Thanks to these experimental studies, we have strong evidence that aSyn fibrils get internalized by neuronal cells *in vivo* and stimulate LB-like pathology and neurotoxicity. Internalized aSyn fibrils also seem to stimulate the aggregation of endogenously expressed aSyn[117]. Some of these experiments however fall short on answering the burning question of cell-to-cell transmission unanimously. Due to the experimental design and the intrinsic limitations of the approach, it cannot be always ruled out that aSyn pathology is induced due to internalization of exogenous injected material in distal areas to the injection site. If not, pathology in distal areas could only stem from *de novo* pathology close to the site of injection and would imply true cell-to-cell transmission[116,118]. A recent study by Rey et al.[119] seems to rule out this issue by applying PFF to the olfactory bulb of a mouse model and observing widespread aSyn pathology in distant brain regions. In conclusion, there is strong evidence for prion-like cell-to-cell transmission in synucleinopathies and a similar picture evolves for other neurodegenerative disorders associated with Aβ, tau and huntingtin[120].

1.4.4 Prion strain-like behavior in synucleinopathies and structural polymorphism

In 2013, Guo et al.[121] showed that *in vitro* aSyn fibrils obtained through *de novo* aggregation (strain A) differ from *in vitro* fibrils that were obtained through repetitive seeding (strain B) and show distinct pathology in primary neuron cultures upon fibril transduction. Guo et al. worked on a C-terminally truncated aSyn construct only comprising residues 1-120 and bearing a C-terminal Myc tag and not *wt* aSyn. Strain A and B also differed in a proteinase K digestion assay, indicating the presence of conformational differences. In addition, Bousset et al.[122] characterized two *in vitro* aSyn fibril polymorphs that were obtained under high- (50 mM Tris-HCl, 150 mM KCl, pH 7.5) and low (5 mM Tris-HCl, pH 7.5) salt conditions using a *de novo* aggregation approach. Solid-state NMR spectroscopy showed that these two types of *in vitro* fibrils differ structurally with additional β-structure present in the N-terminal region of the low salt polymorph. Bousset et al. also showed, that the high and low salt polymorph of aSyn (hsAsyn and lsAsyn respectively) cause different toxicities in a neuronal cell line upon transduction. In a follow-up publication by Peelaerts et al.[117], the two polymorphs were shown to result in distinct pathology in a rat animal model (Wistar rats). In addition, the proteinase K digestion suggested that the confirmation of the polymorphs was conserved throughout *in vivo* passaging. Thus, increasing evidence suggests that aSyn not only leads to templated seeding *in vivo* and *in vitro*, but it also conserves structural features of the primary seed summed up under the term *imprinting*. The term *prion-like* seems to be therefore justified, because a true prion behavior with disease transmission among humans has not been observed[123] yet.

Because these findings were obtained using *in vitro* prepared fibrils, it remains to be shown if strain-like behavior also occurs in patient brains and if differences in pathology among the distinct synucleinopathies are associated with conformationally distinct aSyn strains? To address the question, Prusiner et al.[124]. used brain homogenates of 14 postmortem brains of patients diagnosed with multiple system atrophy (MSA) and Parkinson's disease (PD), six PD cases included in the study, in combination with a hemizygous mouse model (TgM83+/-) that overexpresses human full-length A53T aSyn protein. The mice were intracerebrally injected with brain homogenate and 120 days post-injection the animals were sacrificed and the brains analyzed for neuropathology. Only brain homogenate of MSA patients was able to induce neuropathology with atypical Lewy body pathology in neurons. MSA-infected mouse brain homogenate can also induce pathology upon reapplication to a new TgM83+/- cohort. PD brain homogenate in contrast did not cause neurodegeneration in the mouse model, neither in the first generation with human brain homogenate nor

in the following generation with homogenized mouse brain. This provides further support for the strain model of synucleinopathies (Figure 1-8).
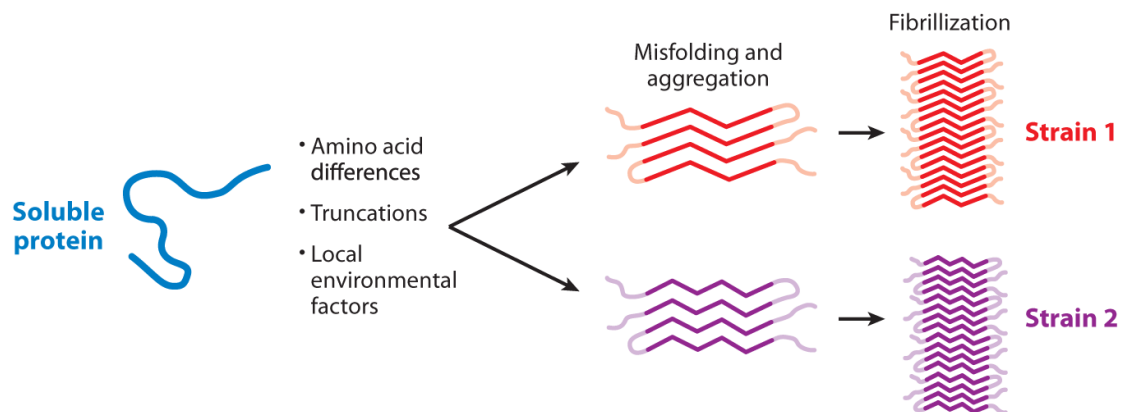
Figure 1-8. Strain behavior in neurodegenerative diseases.
General scheme of strain behavior in neurodegenerative diseases, taken from Walker LC[15].

Prusiner et al. also report that MSA as well as PD brain homogenate failed to induced pathology in mice expressing human or mouse *wt* aSyn. A similar study by Bernis et al.[125] showed neuropathology in mice expressing *wt* human aSyn for brain homogenate of MSA patients and patients with incidental Lewy body pathology, which questioning the unique role of aSyn strains in MSA.

1.4.5 Fluorescent dyes as molecular probes for disease-specific conformations

The binding of fluorescent dyes to amyloid structure is well established and used to stain protein deposits in tissue[126,127]. The Congo red derivative FSB binds amyloid plaques of Aβ as well as NTFs of tau protein[128,129]. FSB and Curcumin also allowed determination of intersubject variability of amyloid-β aggregates in Alzheimer's disease[130], while fluorescent polythiophene dyes were used to distinguish prion strains[131]. The polythiophene derivative HS-68 was developed to successfully probe differences between NTFs and amyloid plaques[132].

1.5 High resolution structures of *in vitro* aSyn fibrils

The first high resolution structure of human *wt* aSyn *in vitro* fibrils was solved by Tuttle et al.[133] using solid-state NMR (PDB accession code: 2N0A). Tuttle et al. showed that the monomeric aSyn entity of an aSyn fibril under their *in vitro* aggregation condition forms a Greek key fold (Figure 1-9c) stabilized by hydrogen bonds in register along the fibril axis. The fibrils were *de novo* aggregated in a sodium buffer (50 mM NaP, pH 7.4, 0.1 mM EDTA, 0.02% NaN$_3$).

Introduction

In July 2018 two groups almost simultaneously published cryo-electron microscopy structures of *in vitro* aSyn fibrils (Figure 1-9 a, b). Guerrero-Ferreira et al.[134] aggregated a C-terminally truncated construct of aSyn (residues 1-121) in Dulbecco's phosphate-buffered saline (DPBS: 2.66 mM KCl, 1.47 mM KH_2PO_4, 137.93 mM NaCl, 8.06 mM Na_2HPO_4, pH 7.0–7.3). They were able to confirm the Greek key topology, but in contrast to Tuttle et al. the aSyn fibrils consist of two entangled protofibrils that form a protofibril interface from residue 50 to 57. The group was able to model aSyn residues 38 to 95 into the electron density map (PDB accession code: 6H6B) at a resolution of 3.4 Å (Figure 1-9a). For the missing residues no electron density was observed, indicating that those residues are not part of the fibril core and show high conformational flexibility in the absence of intermolecular hydrogen bonds.

Li et al.[135] determined the structure of another aSyn *in vitro* fibril by cryo-EM. Full-length *wt* aSyn was fibrillated under identical high salt conditions as in Bousset et al.[122] and Peelaerts et al.[117]. The structure of Li et al. thus provides a high-resolution view of the "high salt polymorph" (hsAsyn) investigated by Bousset et al. and Peelaerts et al.. Li et al. deposited a structure (PDB accession code: 6A6B) comprising residues 37 to 99 at a resolution of 3.07 Å (Figure 1-9b). The structure of a single aSyn molecule is highly similar for residues 38-95 in the cryo-EM structures of Guerrero-Ferreira et al. and Li et al. and also closely overlaps with the Greek key topology determined by solid-state NMR[133]. In addition, the structure of Li et al. displays the dimer of two protofibrils with an almost identical protofilament interface ranging from residue 50 to 57. The two deposited cryo-EM structures, however, differ on the quaternary level. Li et al.'s structure is left-handed while Guerrero et al.'s structure right-handed. These differences could be due to the two groups using different aSyn constructs and/or differences in aggregation buffers.
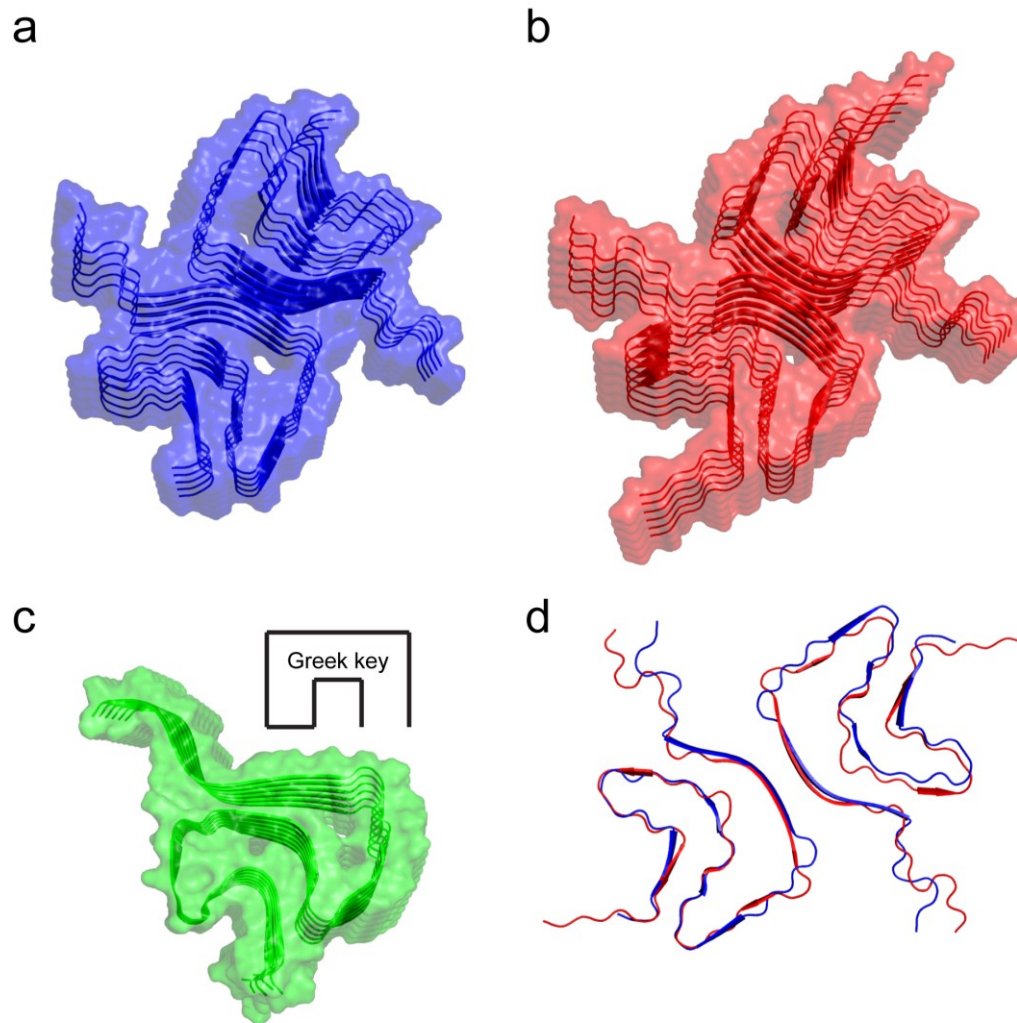
Figure 1-9. High resolution structures of *in vitro* aSyn fibrils.

(a) In blue cryo-EM structure of Guerrero-Ferreira et al. (July 3, 2018), PDB-code: 6H6B, residue 38-95. (b) In red cryo-EM structure of Li et al. (July 31, 2018), PDB: 6A6B, residue 37-99. (c) Solid-state NMR structure of Tuttle et al. (2016), PDB: 2N0A, residue 37-99. (d) Planar overlay of cryo-EM structures blue (6H6B) and in red (6A6B).

1.6   Aims and outline

In the field of neurodegenerative diseases, and in particular for synucleinopathies, the paradigm has evolved that these diseases are caused by prion-like misfolded protein aggregation and spreading of pathology through the nervous system. On the other hand, there is striking evidence that α-synuclein fibrils generated *in vitro* under different aggregation conditions show conformational diversity, so called "polymorphs", associated with distinct toxicities in cells and animal models.

Since synucleinopathies comprise a broad spectrum of pathologies and symptoms that cluster in distinguishable disease types with striking differences in the

manifestation of the disease on the molecular level, the temptation of merging the two observations into one single scientific concept, the strain-like behavior of α-synuclein in synucleinopathies, is high and lively debated in the field. However, the final cornerstone is missing and as convincing as the concept appears, further experimental evidence is needed to proof the hypothesis.

The work of this thesis directly aims to address α-synuclein's potential strain-like behavior in synucleinopathies. To this end, the project followed a clear strategy:

1. The amplification of disease-relevant α-synuclein fibrils from patient brains of distinct synucleinopathies (PD, MDA and DLB) through PMCA by collaborators.
2. The setup of a hydrogen-deuterium (HD) exchange coupled to NMR spectroscopy pipeline based on an established protocol using two well characterized *in vitro* α-synuclein polymorphs achieving single-residue resolution.
3. Biophysical characterization of α-synuclein fibrils for both *in vitro* α-synuclein fibrils as well as for α-synuclein fibrils amplified from patients' brains by negative-stain EM, CD and fluorescent dye binding.
4. Correlation of single-residue HD exchange results by NMR for the high and low salt polymorphs with available data in literature. In addition, for the high salt polymorph mapping of HD exchange data to the available high-resolution cryo-EM structure.
5. Inter-disease correlation of HD exchange data and mapping to high-resolution cryo-EM structure.
6. Characterization of α-synuclein fibrils by ortholog high-resolution EPR spectroscopy through collaboration.

2 Materials and methods

2.1 Chemical reagents

(E,E)-1-fluoro-2,5-bis(3-hydroxycarbonyl-4-hydroxy)styrylbenzene (FSB) from Santa Cruz Biotechnology (Lot # D1012, sc-359845), Curcumin from Sigma-Aldrich (Lot # WXBC5818V, 08511-10MG), HS-68 synthesized by the Synthetic Chemistry Facility of the MPIBPC Göttingen, (1-oxy-2,2,5,5-tetramethyl-d-pyrroline-3-methyl)-methanethiosulfonate (MTSL) from Toronto Research Chemicals, Ammonium chloride (^{15}N, 99%) from Cambridge Isotope Laboratories, D-Glucose (U-13C6, 99%) from Cambridge Isotope Laboratories, Deuterium oxide from Sigma-Aldrich (756822-1.107KG), Guanidine thiocyanate (BioUltra, >99.0%) from Sigma-Aldrich (50980).

2.2 Bacterial strains and plasmids

Cell lines: Competent BL21(DE3) cells purchased from Invitrogen (44-0048)

Plasmids: pT7-7 aSyn WT provided by the Lansbury Laboratory, Harvard Medical School, Cambridge

pNatB (pACYCduet-naa20-naa25) purchased from Addgene (53613)

2.3 Equipment

Bruker NMR spectrometers (400 – 950 MHz), Eppendorf Thermomixer comfort, Eppendorf Entris precision balance, IKA KS 4000i incubator, INFORS HT Multitron incubator, GFL water bath, AVESTIN EmulsiFlex C3 French press, Beckman Coulter centrifuge Avanti JXN-26, Beckman Coulter JLA-8.1 rotor, Beckman Coulter JA-25 rotor, Eppendorf Centrifuge 5810R, Eppendorf Centrifuge 5424R, GE Äkta prime plus, GE Äkta pure, Eppendorf BioSpectrometer, Beckman Coulter Optima MAX-XP Ultracentrifuge, Bandelin Sonorex Digitec ultrasonic bath, Agilent Technologies Cary Eclipse fluorescence spectrophotometer, Applied Photophysics qCD Chirascan spectrophotometer, Agilent Technologies 1260 Infinity HPLC pump and UV detection unit, Wyatt miniDAWM TREOS, Wyatt Optilab T-rEX, Wyatt DynaPro NanoStar, ThemoFisher Herasafe KS clean bench, Heidolph Duomax 1030 shaker, Sartorius CPA 2245 analytical balance, BioRad GelDoc XR+, TECAN Spark 20 M plate reader, ThermoScientific Heratherm incubator, Mono Q 5/50 GL, GE Superdex 75 and Superdex 200 16/600 GL, GE Superdex 75 and S200 26/600, GE Superdex 10/300 GL, Sharp microwave.

2.4 Software

Topspin (Bruker), Sparkcontrol v2.2 (TECAN), Pro-Data Chirascan v4.5 (Applied Photophysics), NMRPipe[136] v8.9, Prism v7 (GraphPad), Excel v16 (Microsoft), MATLAB R2016b (MathWorks), DeerAnalysis2018[137,138], CcpNmr Analysis[139] v2.4, PyMOL v2.2.0, Illustrator CS v5.1 (Adobe), Word v16 (Microsoft), EndNote X8, Affinity Photo v1.6.

2.5 Buffers

Low salt buffer: 5 mM Tris-HCl, pH 7.5, 0.02% NaN_3
High salt buffer: 50 mM Tris-HCl, 150 mM KCl, pH 7.5, 0.02% NaN_3
HEPES buffer: 50 mM HEPES, 100 mM NaCl, pH 7.4, 0.02% NaN_3

2.6 Protein preparation

Purification was performed as previously described by Hoyer et al.[38]. If not explicitly stated otherwise, aSyn refers to N-terminally acetylated *wt* α-synuclein. Stefan Becker and Karin Giller (NMR2, Max-Planck-Institute for Biophysical Chemistry, Göttingen, Germany) kindly provided non-acetylated *wt* α-synuclein for reference experiments, stock solution 0.3 mM in HEPES buffer. Sol Cima (Translational Structural Biology in Dementia, DZNE, Göttingen, Germany) helped with the preparation of aSyn.

2.6.1 Transformation and glycerol stock

Human N-terminally acetylated *wt* α-synuclein (aSyn) was obtained by co-transfection of *E. coli* BL21 (DE3) cells with pT7-7 plasmid encoding for *wt* human α-synuclein and NatB acetylase complex of *Schizosaccharomyces pombe*[140] using pNatB plasmid. The pT7-7 plasmid was kindly provided by the Lansbury Laboratory, Harvard Medical School, Cambridge MA. The pNatB plasmid (pACYCduet-naa20-naa25) was a gift from Dan Mulvihill (Addgene plasmid # 53613). BL21(DE3) Competent *E. coli* cells were thawed on ice, 300 ng of each plasmid DNA was added and incubated for 5 minutes on ice. Heat shock was performed for 45 sec at 42 °C on an Eppendorf Thermomixer comfort. 200 µL of autoclaved LB medium was added and the temperature was set to 37°C. The BL21 (DE3) cells were incubated for another 30 minutes under shaking, 650 rpm. 50 µL of cells were plated out on LB-agar plates with 100 µg/ml ampicillin (Amp) and 25 µg/ml chloramphenicol (Chl), plates were incubated at 37°C o/n. A single *E. coli* colony was picked the following day and o/n culture grown

in 7 ml LB medium (100 µg/ml Amp, 25 µg/ml Chl) at 37 °C. Eventually 500 µL of o/n culture was mixed with 500 µL of sterile 50% glycerol in water in a 2 ml screw top tube, gently mixed and shock frozen in liquid nitrogen, storage at -80°C.

2.6.2 Protein expression

25 ml LB medium preculture (100 µg/ml Amp, 25 µg/ml Chl) was inoculated with BL21(DE3) pT7-7 pNatB glycerol stock and grown o/n at 37 °C. A sterile disposable inoculation loop was used to scratch the glycerol stock surface and then inserted into the LB medium of the preculture. For unlabeled aSyn expression, 2 ml of o/n preculture was added to 1 l of LB medium (Amp/Chl) and grown to OD_{600} of ~ 0.8, induced with 0.5 mM IPTG final concentration and incubated at 25 °C o/n. For ^{15}N-labeled and double-labeled (^{13}C-,^{15}N-labeled) aSyn, the protocol was slightly adapted. 4 ml of the 20 ml o/n LB medium preculture was shortly centrifuged in a 15 ml Falcon tube and the pellet resuspended in 4 ml 1x M9 minimal medium (Amp, Chl) before adding it to 1 l of 1x M9 medium (Amp/Chl) supplemented with $^{15}NH_4Cl$ (0.5 g/l) and in case of double-labeled supplemented additionally with D-^{13}C-Glucose (4 g/l) and further grown to OD_{600} of ~0.8. 0.5 mM IPTG was added for induction and protein expression happened at 25°C o/n.

Compound	Amount
M9 salts (5x)	200 ml
Trace elements	10 ml
$CaCl_2$ (1 M)	300 µl
$MgSO_4$ (1 M)	1 ml
Thiamine (10 mg/ml)	0.1 ml
D-Glucose / D-^{13}C-Glucose	4 g / 4 g
$^{15}NH_4Cl$	0.5 g
H_2O (deionized)	up to V_t = 1 l

Table 2. Recipe for 1 l M9 minimal medium.

M9 salts (5x):   30 g Na_2HPO_4, 20 g KH_2PO_4 x 3 H_2O, 2.5 g NaCl dissolved in 1 l H_2O (deionized)

Trace elements: 0.6 $FeSO_4$ x 7 H_2O, 0.115 g $MnCl_2$ x 4 H_2O, 0.08 g $CoCl_2$ x 6H_2O, 0.07 $ZnSO_4$ x 7 H_2O, 0.03 $CuCl_2$ x 2 H_2O, 0.002 gH_3BO_3, 0.025 g $(NH_4)_6Mo_7O_{24}$ x 4 H_2O, 0.5 g EDTA dissolved in 100 ml H_2O (deionized)

2.6.3 Cell harvest and purification

Cells were harvested at 4 °C for 15 minutes at 7000 rpm using a Beckmann Coulter centrifuge with a JLA-8.1 rotor. The supernatant (SN) was discarded and the bacteria pellet stored for further use at -20 °C. The cell pellets were resuspended in 20 ml per 1 l culture volume lysis buffer (10 mM Tris-HCl, pH 8, 1 mM EDTA, 1mM PMSF). Cell lysis was achieved using a French press. The cell lysate was boiled in a water bath at ~100 °C for 30 minutes and centrifuged in a JA-25 rotor at 13,500 rpm at 4 °C for 30 minutes, the SN was saved. DNA of SN was precipitated by adding at a ratio of 1:10 streptomycin sulfate from a stock solution in water (100 mg/ml). The DNA precipitation was enhanced by constant shaking for 15 minutes at 4 °C. The precipitated DNA was separated as a pellet from the solution by a 30-minute centrifugation step, using a JA-25 rotor (13,500 rpm, 4 °C). Thereafter aSyn and residual protein impurities were precipitated by adding ammonium sulfate, weighing in the salt to a final concentration of 360 mg/ml and incubating the solution for 15 minutes at 4 °C under constant shaking. The protein pellet was harvested by centrifugation as described earlier and the SN discarded. The pellet was either stored at -20 °C or directly used for further purification steps.

The pellet was then resuspended in 25 mM Tris-HCl buffer, pH 7.7 and dialysed o/n against 4 L of the same buffer, Roche protease inhibitor added. The dialysate was sterile filtered and applied to a Mono Q 5/50 GL anion exchange column. To the column a salt gradient (25 mM Tris-HCl, pH 7.7, 0 – 1 M NaCl) was applied, aSyn elutes around 300 mM NaCl. The aSyn fraction was collected and loaded onto a Superdex gel filtration column (S75 and/or S200) in order to remove high and low weight impurities. Gel filtration was always performed in fresh, sterile filtered and degassed HEPES buffer. The final pure protein yield was concentrated via centrifugal concentrators (MWCO 5 kDa) and sterile filtered (0.22 µm). Aliquots at concentrations between 500 µM and 1 mM were shock-frozen in liquid nitrogen and stored at -80°C.

All steps of the purification were monitored by SDS-PAGE with 15% gels and the protein concentrations were determined by an Eppendorf BioSpectrometer using 100 µL quartz cuvettes and an extinction coefficient of 5960 M^{-1} cm^{-1}. An example purification is shown in Figure 2-1.

a

b
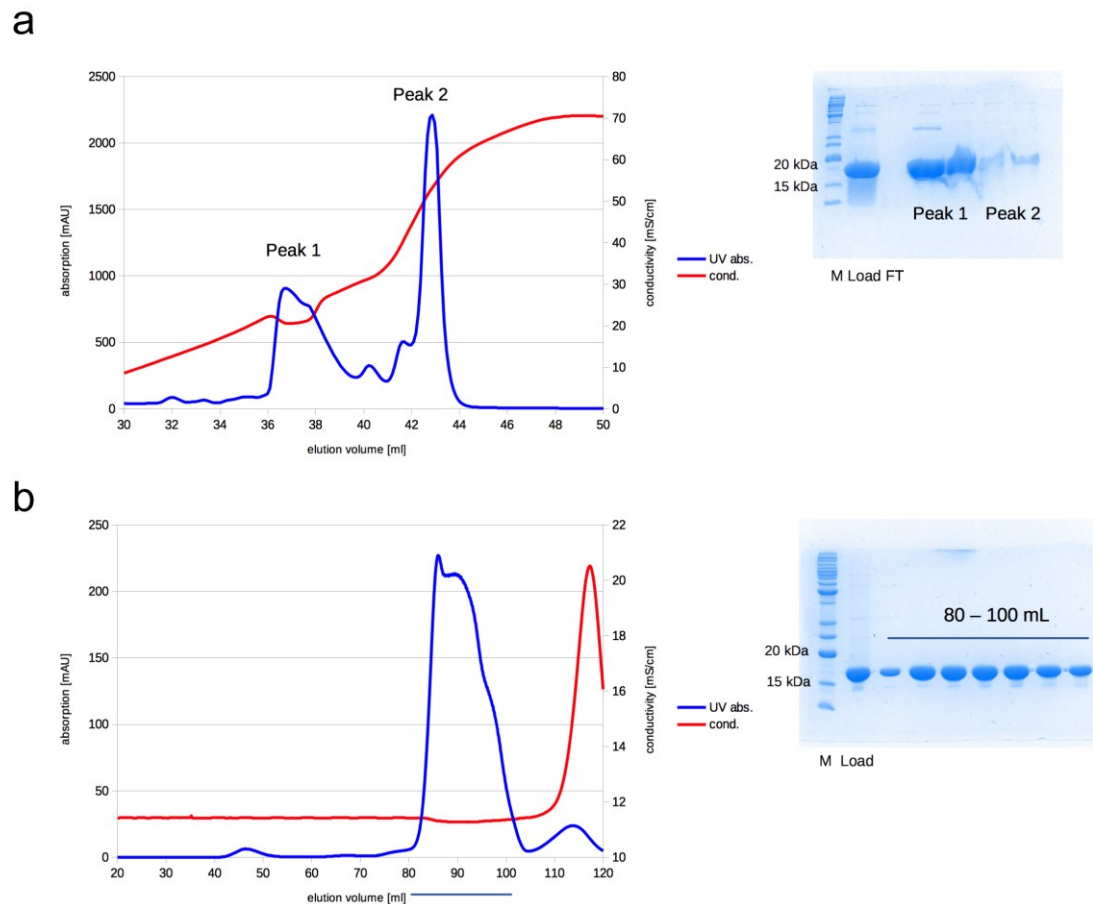
Figure 2-1. Purification of N-terminally acetylated α-synuclein.

(a) Mono Q 5/50 anion exchange column run. (b) Gel filtration on Superdex 200 10/300 GL. Using GE Äkta pure, 15% SDS-PAGE, M: Marker (BenchMark, Invitrogen), FT: flow through.

2.7 SEC-MALS

The standard technique multi-angle light scattering[141] coupled with size exclusion chromatography (SEC-MALS[142]) was used for the biophysical characterization of monomeric *in vitro* aSyn as described before by Burré et al.[143]. The combination of MALS with analytical size exclusion allows absolute mass determination at any position of the elution chromatogram characterizing the different conformational species of soluble protein as well as the analysis of mixed samples.

200 µL of aSyn and non-acetylated α-synuclein at a concentration of 50 µM were injected onto a Superdex 200 10/300 GL analytical column (GE) using the HPLC system 1260 Infinity with UV detection unit (Agilent Technologies) in combination with the Wyatt system: MALS detector miniDAWM TREOS, RI detector Optilab T-rEX and online QELS detector DynaPro NanoStar. The data analysis was performed with the

Wyatt Astra software package (Astra 7) using a standard BSA (Sigma) protein solution run at a concentration of 1 mg/ml for peak alignment and band broadening.

2.8   Mass spectrometry of aSyn

Kerstin Overkamp (NMR2, Max-Planck-Chemistry of Biophysical Chemistry, Göttingen, Germany) performed all mass spectrometry experiments. She was provided with a 1 mg/ml aSyn solution in HEPES buffer. N-terminal acetylation of aSyn was validated using a single quadrupole mass detection system (SQ Detector 2) from Waters in combination with a HPLC system from ACQUITY with diode-array detectors (DAD). The DAD spectrum combines all absorption properties of the sample between 210 and 400 nm. Mass-to-charge ratios (m/z) from 400 to 2500 Da were recorded. For HPLC, a XSelect Peptide CSH C18 column from Waters was chosen with buffers A: 0.1 % TFA in H_2O (deionized) and B: 0.1 % TFA in acetonitrile. The theoretical molecular weight (M_w) of N-terminally acetylated aSyn is: 14.502 kDa (Appendix: 7.1.2).

2.9   Patient material

The patient material used in this study was kindly provided by Glenda M. Halliday (Brain and Mind Centre, Sidney Medical School, Sidney, Australia). Table 3 summarizes the anonymized patient data.

Disease #	Age	Gender	Postmortem delay (hrs)	Cause of death	Disease duration (yrs)
PD1	79	Male	17	Acute myocardial infarction	7
PD2	82	Male	22	Cardiorespiratory failure	7
PD3	81	Female	29	Cardiorespiratory failure	22
MSA1	82	Male	8	Cardiorespiratory failure	7
MSA2	71	Female	19	Hypostatic pneumonia	6
DLB1	69	Male	28	Cardiorespiratory failure	3
DLB2	78	Male	3	Anorexia/cachexia	7

Table 3. Demographics of donor brains from synucleinopathy patients.
PD: Parkinson's disease, MSA: multiple system atrophy, DLB: Dementia with Lewy bodies.

2.10 PMCA and aSyn aggregation

2.10.1 Homogenization of patient's material and PMCA

The human amygdala samples of the synucleinopathy patients (Table 3) were homogenized and amplified by PMCA as described earlier by Jung et al.[106] (Figure 2-2). Homogenization and PMCA was done by Byung Chul Jung (Department of Biomedical Sciences, Neuroscience Research Institute, Seoul, Korea).

The amygdala samples were diluted 10% (w/v) in PBS homogenization buffer (1% Triton X-100 in PBS, Roche protease inhibitor added) and sonicated with a Vibra-cell sonicator from Sonics. Protein misfolding cyclic amplification (PMCA) was performed with a Qsonica system comprising a microplate horn, a sound enclosure and a thermoelectric chiller. aSyn was diluted in PBS conversion buffer (1% Triton X-100 in PBS, Roche protease inhibitor added) to a final concentration of 2.5 µM. 50 µl of aSyn were transferred into PCR tubes that contained 2.5 µg of brain homogenates of the different patient material. Prior to PMCA, three PTFE beads were added to each PCR tube. The samples were subjected to cycles of 20 sec sonication (amplitude 1%) and 29 min 40 sec of incubation at 37°C. Total duration of the PMCA was 2 days.
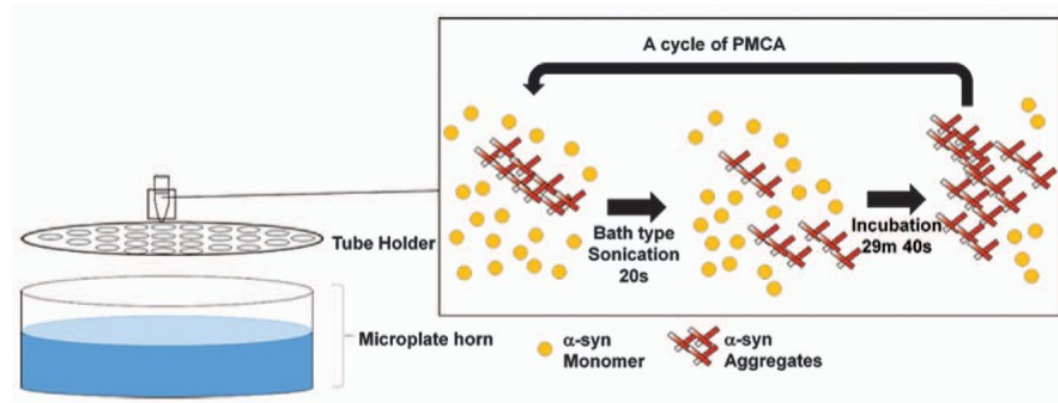
Figure 2-2. Basic principle of cyclic amplification of aSyn fibrils using PMCA.
Taken from Jung et al.[106].

2.10.2 Preparation of aSyn fibrils

aSyn aggregation was performed at 37 °C using 250 µM monomeric aSyn taken from the supernatant (SN) of freshly thawed aSyn on ice after ultracentrifugation (UC) for 1 hour and contained 0.02% NaN_3. All UC steps were performed on an Optima MAX-XP (Beckman Coulter) using a TLA 100.3 rotor with a rotor speed of 55,000 rpm. aSyn concentrations were determined by UV absorption (5960 M^{-1} cm^{-1}) at 280 nm using an Eppendorf BioSpectrometer. Fibrillization was monitored by ThT fluorescence (see section 2.12).

Material and methods

De novo aggregation

In case of *de novo* fibrillization of high (hsAsyn; 50 mM Tris-HCl, 150 mM KCl, pH 7.5, 0.02% NaN_3) and low salt (lsAsyn; 5 mM Tris-HCl, pH 7.5, 0.02% NaN_3) *in vitro* polymorphs, monomeric aSyn (unlabeled and ^{15}N-labeled) was dialyzed against the respective aggregation buffer at 4 °C o/n, followed by fibrillization as described in Bousset et al.[122]. After harvesting (see fibril harvest) the *in vitro* fibrils, the fibril pellets were either directly used in hydrogen-deuterium (HD) exchange experiments or for subsequent seeded aggregation experiments the *de novo* aggregated fibril pellets were resuspended in fresh aggregation buffer to a final concentration of 250 µM, water bath (Bandelin Sonorex) sonicated for 1 min, aliquoted and shock-frozen in liquid nitrogen for storage at -80 °C.

In vitro seeded aggregation, high and low salt

Seeded aggregation of the *in vitro* polymorphs was performed in the same manner as *de novo* aggregation, but adding 0.5% (w/w) of room temperature thawed seeds to the aggregation reaction followed by fibril harvest through UC. If not stated otherwise, all data reported for *in vitro* polymorphs were obtained through seeding.

Seeded aggregation of synucleinopathic fibrils obtained through PMCA

For the patient-derived aSyn fibrils, 0.5% (w/w) PMCA end product was added to 250 µM aSyn stock solution (50 mM HEPES, 100 mM NaCl, pH 7.4, 0.02% NaN_3) and initially water bath sonicated for 10 minutes. This mixture was aggregated under quiescent conditions in 1.5 ml Eppendorf cups in a Heratherm (ThermoScientific) incubator (Figure 2-3) at 37 °C. After complete fibril formation the fibrils were harvested.

Fibril harvest

Fibrils were harvested by UC (55 krpm) for 2 hours at 25 °C and the SN was separated from the pellet. aSyn concentrations in the SN were determined spectrophotometrically to estimate fibril yield.
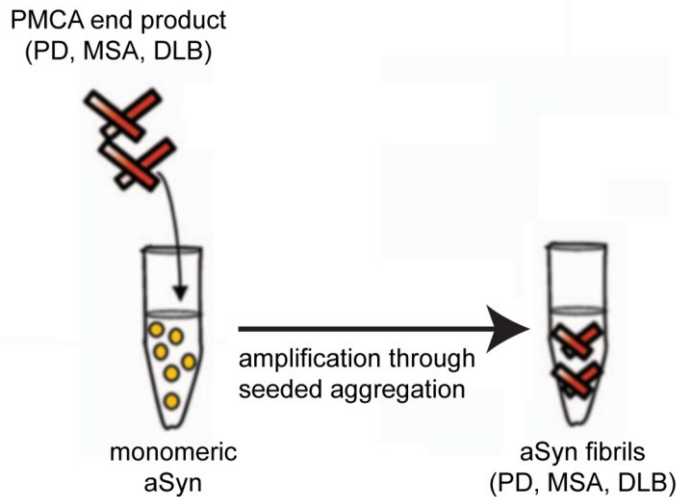
Figure 2-3. Aggregation scheme for PMCA end products.

2.11 Negative stain transmission electron microscopy

Electron microscopy experiments were performed by Gudrun Heim (EM-Facility, Max-Planck-Institute for Biophysical Chemistry, Göttingen, Germany). Samples were adsorbed onto 400 mesh carbon-coated copper grids and the buffer was removed using a filter paper. Subsequently, samples were stained by the addition of 1% uranyl acetate solution, which was subsequently dried with a filter paper. The grids were imaged using a FEI CM 120 electron microscope with a Tietz F416 CMOS camera.

2.12 Thioflavin T fluorescence

The assembly of aSyn fibrils was monitored over time by Thioflavin T (ThT) fluorescence. ThT dye's application in *in vitro* binding of amyloid fibrils was described by Naiki et al.[144]. A ThT stock solution of 5 mM ThT in deionized water was produced, sterile filtered, aliquoted and stored at -20 °C. For each aggregation assay a fresh 10 µM ThT glycine buffer solution (50 mM glycine in deionized water, pH adjusted to 8.8 and sterile filtered) was produced. The ThT solution was always kept in the dark and stored at RT. 2 µl aliquots of aSyn aggregation sample (*de novo* and/or seeded) were taken at different time points from the total sample volume and added to 200 µl of 10 µM ThT in glycine buffer to monitor the fibril assembly progress via a Cary Eclipse fluorescence spectrophotometer (Agilent Technologies). The samples were thoroughly mixed at RT and 180 µl were transferred to a black 96-well plate (Greiner) and the maximum emission value was determined at 482 nm exciting the sample well at 440 nm (ex. bandwith: 10 nm, em. bandwith: 10 nm, gain: 600V PMT detector).

2.13 CD spectroscopy

Circular dichroism (CD) spectroscopy is a powerful tool to estimate the secondary structure elements of proteins in the far-ultraviolet (UV) spectrum[145].
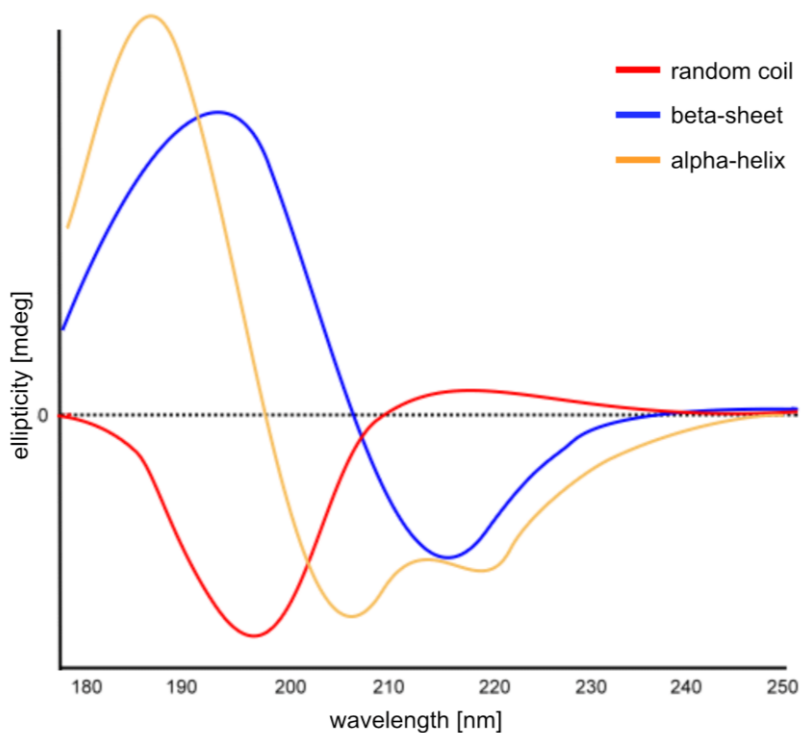
Figure 2-4. Overview of CD spectra of pure secondary structures.
Adapted from Farid, R. S.[146]

For characterization of aSyn fibrils, 5 µL of aggregation sample were centrifuged for 10 minutes at 20,000 g in an Eppendorf centrifuge 5424. The pellets were resuspended in 60 µl deionized water after discarding the supernatants and transferred to a 0.02 cm pathlength cuvette. CD data were collected from 185 nm to 260 nm by using a Chirascan qCD spectrometer (Applied Photophysics) at 20 °C, 1.5 time-per-point (s) in 1 nm steps. The datasets were averaged from two repeats. All spectra were baseline corrected against deionized water and smoothed (window size: 8, 4th order polynom).

2.14 Fluorescent dye binding

The dyes (E,E)-1-fluoro-2,5-bis(3-hydroxycarbonyl-4-hydroxy)styrylbenzene (FSB) and curcumin were purchased from Santa Cruz Biotechnology and Sigma-Aldrich. The polythiophene acetic acid derivative HS-68 was synthesized by the Synthetic Chemistry Facility (Max-Planck-Institute for Biophysical Chemistry) according to published procedures[147] as a sodium salt, see (Appendix: Figure 7-1).
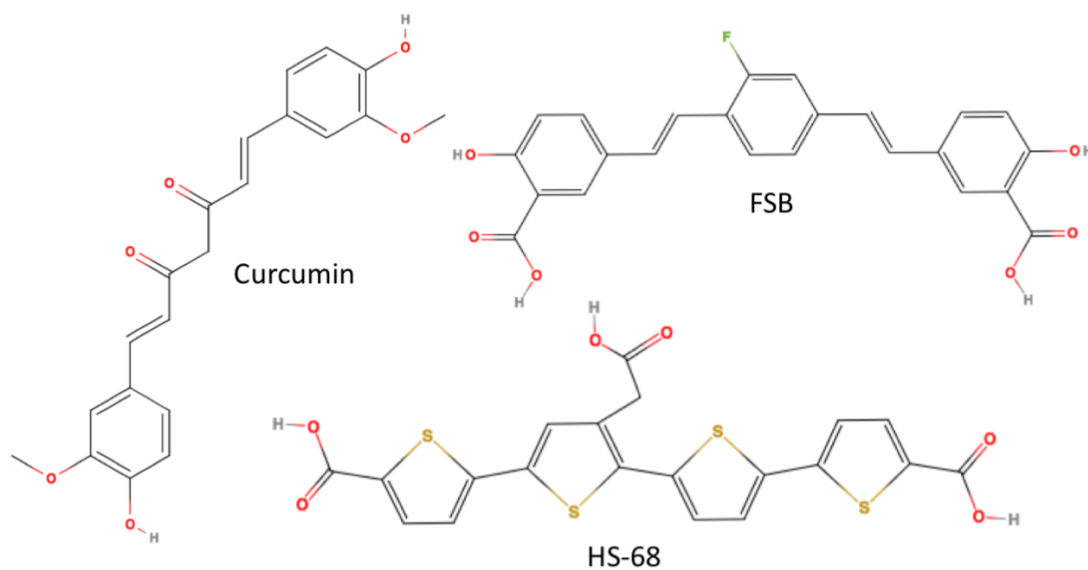
Figure 2-5. Chemical structural formula of fluorescent dyes.

The fluorescent dyes curcumin and FSB were dissolved in DMSO, HS-68 in deionized water at a stock solution of 5 mM. The stock solution was then aliquoted and stored at -20 °C in the dark. Working solutions were freshly prepared from the dye stocks to a final concentration of 50 µM of the respective dye in 50 mM HEPES, 100 mM NaCl, pH 7.4, the final DMSO concentration for curcumin and FSB was 1 %.

100 µL of working dye solution was mixed thoroughly with 10 µL of aSyn fibrils to a final protein-to-dye ratio of ~1:6. The samples were transferred to a 96-well microplate (PS, µCLEAR, black, chimney well from Greiner). The fluorescence measurements were performed on a Spark 20M reader (TECAN) and read from the top at 25 °C with z-Position: 17191 µm, intensity 505 averaged over 30 flashes, 2 nm steps.

Curcumin: ex.: 440 nm, gain: 80, ex. bandwidth: 20 nm, em. bandwidth: 20 nm, 485 – 800 nm.
FSB: ex.: 380 nm, gain: 60, ex. bandwidth: 10 nm, em. bandwidth: 10 nm, 450 – 800 nm.
HS-68: ex.: 450 nm, gain: 60, ex. bandwidth: 10 nm, em. bandwidth: 10 nm, 510 – 800 nm.

All spectra were baseline subtracted by dye buffer blank measurements and smoothed (windows size: 8, 4th order polynom).

2.15 NMR spectroscopy

2.15.1 Heteronuclear single quantum coherence (HSQC)

Due to the small gyromagnetic ratio of hetero nuclei (such as ^{15}N and ^{13}C) in comparison to protons (^{1}H), a vast amount of complex inverse magnetization transfer based pulse sequences were developed for liquid-state NMR spectroscopy achieving magnetization transfer from proton to the hetero nuclei of choice, followed by variable evolution periods under defined conditions and eventually ending with back-transfer of magnetization to ^{1}H for detection.

a

b
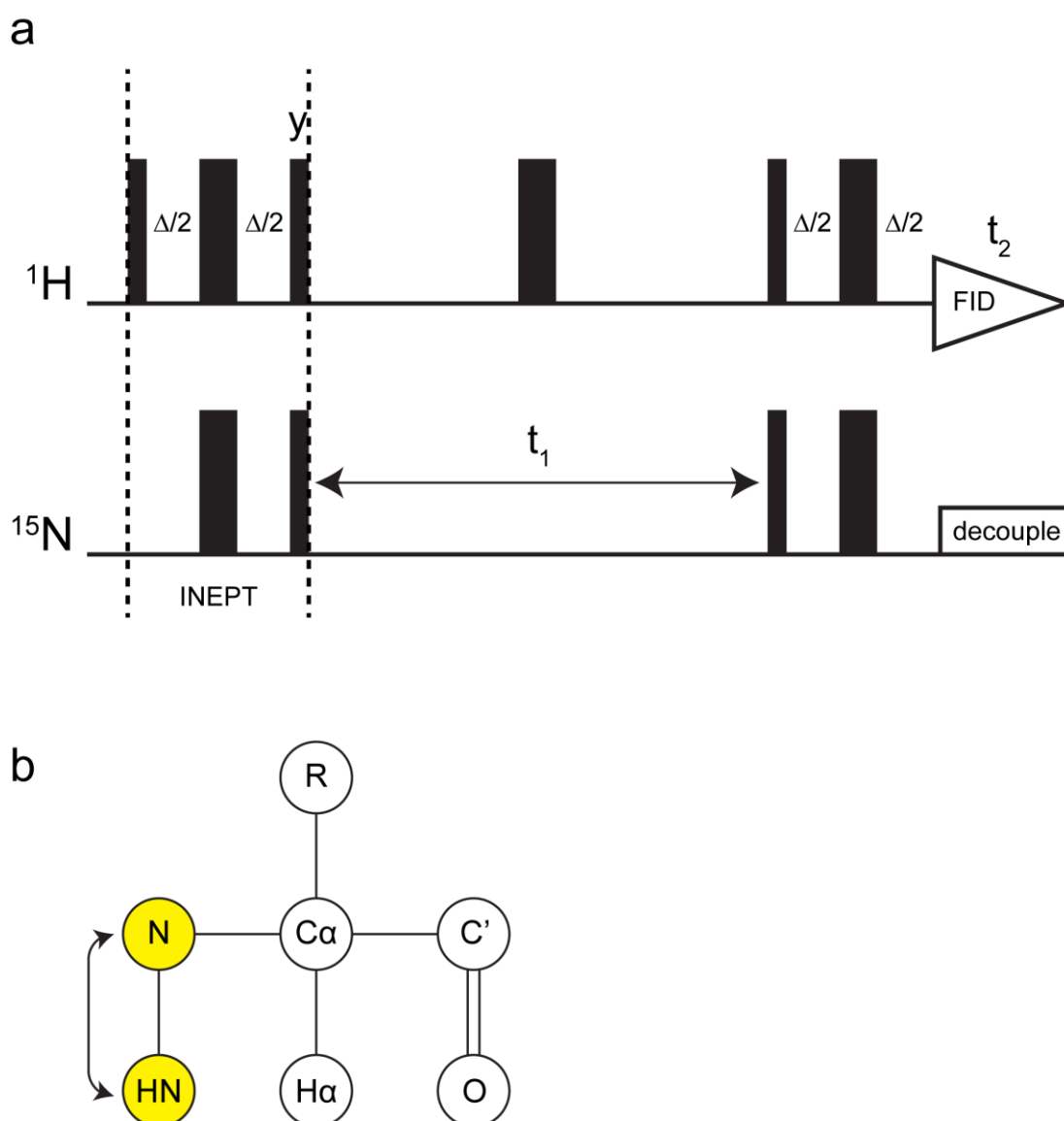
Figure 2-6. Simplified scheme of 2D HSQC NMR spectroscopy.

(a) Schematic visualization of a HSQC pulse sequence. Narrow bars represent 90°, wide bars 180° pulses. All pulses have phase x if not stated otherwise. The INEPT element is indicated by dashed lines. Δ is set to $1/(2J_{NH})$ for complete transformation of in-phase into anti-phase

magnetization. The block "decouple" stands for the ^{15}N broad band decoupling pulse during acquisition. (b) The HSQC pulse sequence achieves magnetization transfer from the amide attached proton (^{1}H) to the nitrogen (^{15}N) of the amide bond shown for the amino acid backbone of a polypeptide sequence. INEPT: insensitive nuclei enhancement through polarization transfer.

In case of the ^{1}H-^{15}N HSQC pulse sequence[148] (Figure 2-6 a) magnetization transfer from the proton to the ^{15}N hetero nucleus is achieved via the INEPT element, evolution of chemical shift of ^{15}N occurs then during t_1 but not for ^{1}H, a $180°_x$ pulse centered in t_1 applied only on ^{1}H refocuses the offset of ^{1}H. The evolution period t_1 is followed by a reverse-INEPT block restoring in-phase magnetization on ^{1}H preceding acquisition under t_2 with broad band decoupling on ^{15}N (Figure 2-6 a).

Recording a set of one-dimensional proton FIDs during t_2 incrementing the evolution period t_1 results in a two-dimensional dataset in the time domains t_2 and t_1. Operations can be directly performed on the time domains such as baseline correction, linear prediction and window multiplication. Eventually using the fast Fourier transform algorithm, the dataset is converted into a 2D ^{1}H-^{15}N HSQC spectrum in the frequency domain plotted in parts per million (ppm). The final HSQC spectrum is obtained using empirically optimized phase correction. Since the HSQC pulse program correlates the protons directly bonded to nitrogen (^{15}N), it is a powerful tool for protein science. The amide backbone of proteins and polypeptides own for each amino acid residue one proton single-bonded to nitrogen (Figure 2-6 b), except for proline residues (Pro, P) that cannot be studied by HSQC spectra.

The HSQC pulse sequence[149-151] used in this study is shown in Appendix 7.5 in detail and is more complex than the scheme shown in Figure 2-6 a, however the same basic principles hold true.

2.15.2 Resonance assignment

Backbone resonance assignments of aSyn in the dissolving buffer (4M GdSCN, 0.4% formic acid, pH 2.5) at a protein concentration of 600 μM were obtained with the help of 3D HNCO[152,153,154], HN(CA)CO[155,154], HNCA[152,153,154], HN(CO)CA[153,154] and HNCACB[156,157] experiments[158], in which indirect frequency dimensions were sampled in a non-uniform manner (NUS)[159] for the experiments stated in Table 4 using standard Bruker pulse sequences. The spectra were processed using nmrPipe[136] with SMILE[160] for NUS data and analyzed with CcpNmr Analysis software package[139].

Experiment	Parameters	Spectrometer	Pulse sequence
HNCO	110x60x2048, ns: 16	600 MHz	hncogpwg3d
HNCO	128x80x2048, ns: 16, NUS (25%)	800 MHz, cryoprobe	hncogpwg3d_sct
HN(CA)CO	105x60x2048, ns: 32	600 MHz	hncacogpwg3d
HNCA	115x60x2048, ns: 32, NUS (25%)	800 MHz, cryoprobe	hncagpwg3d_sct
HN(CO)CA	104x60x2048, ns: 24	600 MHz	hncocagpwg3d
HNCACB	124x100x2048, ns: 40, NUS (30%)	800 MHz, cryoprobe	hncacbgpwg3d_sct

Table 4. 3D experiments recorded for resonance assignment of aSyn in dissociation buffer.

2.15.3 Weighted chemical shift perturbations

The weighted chemical shifts (CSP) were calculated using the relative chemical shifts in ^{1}H (δ_H) and ^{15}N (δ_N) according to:

$$d = \sqrt{\frac{1}{2} \cdot \left[\delta_H^2 + \left(\frac{1}{5} \cdot \delta_N^2 \right) \right]}$$

2.15.4 Secondary chemical shifts

Secondary chemical shifts were calculated using CcpNmr Analysis software package[139] based on the assignment (Appendix: Table 5) according to Schwarzinger et al.[161].

2.16 Hydrogen-deuterium exchange

The combination of hydrogen-deuterium (HD) exchange studies with methods of rapid fibril dissociation and liquid-state NMR spectroscopy allows the determination of deuterium incorporation levels with single-residue resolution[162,163,164]. To further enhance the distinction for residues with different amide proton exchange rates, a mixture of H_2O and D_2O in the dissociation buffer was used. Hydrogen-deuterium (HD)

exchange coupled to nuclear magnetic resonance (NMR) spectroscopy (Figure 2-7) was performed according to a previously established protocol by Cho et. al.[162].

2.16.1 Forward exchange

Previous HD exchange studies conducted on *in vitro* aggregated aSyn fibrils established that a forward (fw) exchange time of 1.5 days allows robust determination of residue-specific protonation level[162,164]. To slow down HD exchange and thus allow a better definition of regions with small differences in solvent protection, forward HD exchange was done in 0.1% formic acid (pD 4.0) in 99.9 % D_2O at 37 °C. The forward HD exchange of amide protons in aSyn fibrils was stopped after 1.5 days, fibrils were collected by ultracentrifugation (2 hours, 200,000 g), frozen in liquid nitrogen and stored in a refrigerator at -80 °C.

2.16.2 Back-exchange and NMR real-time acquisition

Subsequently, back-exchange in the dissociation buffer (4 M guanidine thiocyanate (GdSCN), 0.4% formic acid, pH 2.5, in 60 % D_2O) was followed by 120-140 2D ^1H-^{15}N heteronuclear single quantum coherence (HSQC) experiments (experimental time for each HSQC: 8 min 16 sec; number of increments in ^{15}N-dimension: 128) recorded over a time period of ~19 hours at a temperature of 3 °C. NMR experiments were measured on a Bruker 800 MHz spectrometer equipped with a 5 mm triple-resonance, pulsed-field z-gradient cryoprobe. Preparative steps such as shimming and temperature equilibration resulted in a dead time of about 7 minutes (measured for each data set) before the start of the first HSQC.

2.16.3 Data analysis

Acquired spectra were processed with linear prediction for the ^{15}N dimension and analyzed by NMRPipe[136]. The relative intensity (height) data for 103 HSQC-separated aSyn residues were extracted from 120-140 2D ^1H-^{15}N HSQC spectra using the centered peak position of the final fully exchanged HSQC spectrum of the series normalized to a value of 1.0 using NMRPipe[136]. For each aSyn residue the back-exchange curves were fitted to a single exponential decay using Prism (Graphpad). Knowing the exact dead time and HSQC experiment duration the relative t_0 intensity level was back-calculated and the scale was transformed into absolute protonation levels by using the average maximum intensity value of the five residues with highest signal intensity.
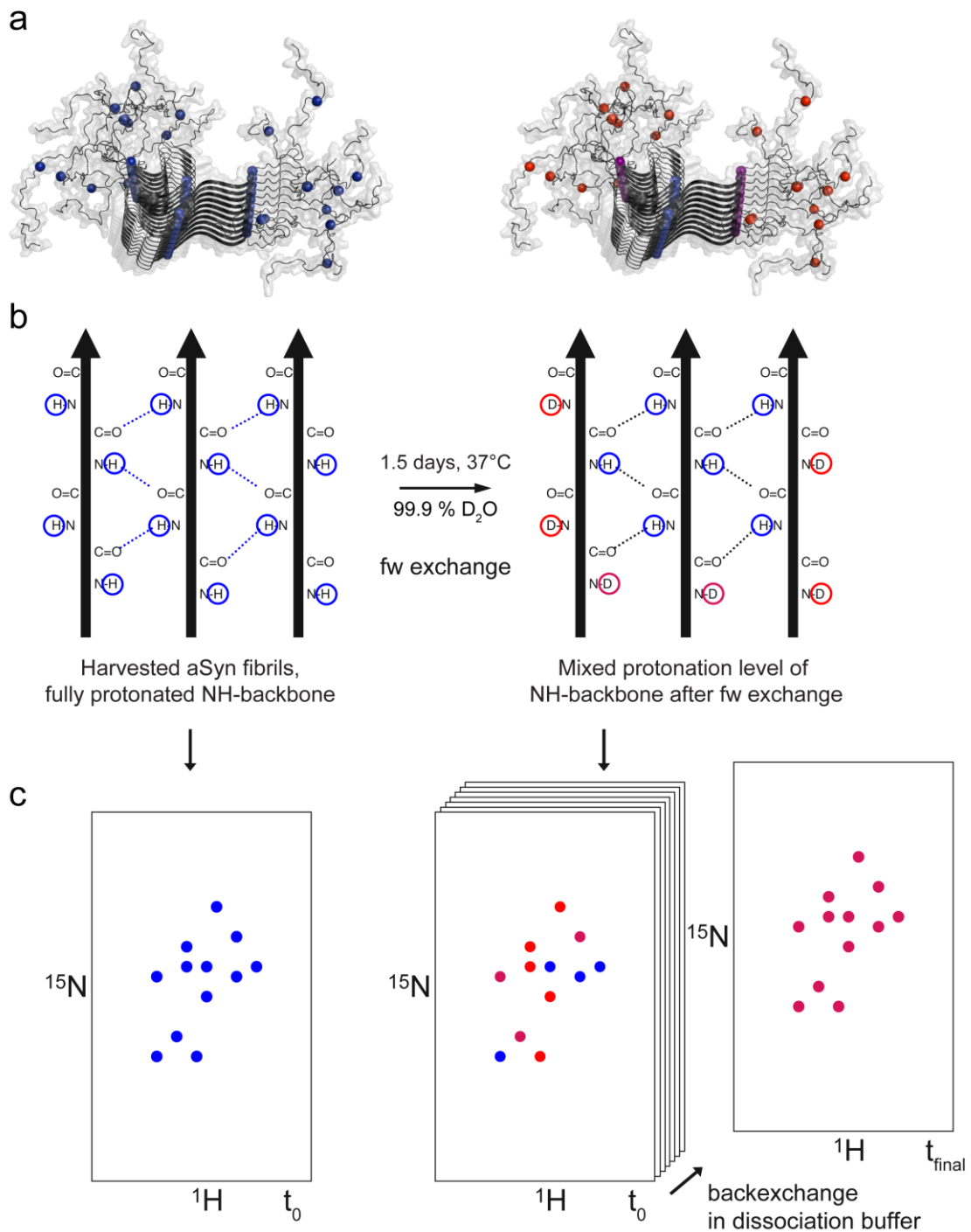
Figure 2-7. Schematic description of HD exchange coupled to NMR spectroscopy.
(a) aSyn fibril model before (left) and after fw exchange showing selected protons of the NH-backbone, blue: fully protonated, red: fully deuterated, purple: intermediate protonation level.
(b) Simplified HD fw exchange scheme. (c) HSQC intensities coding for protonation level.

2.17 EPR spectroscopy

Monomeric aSyn was aggregated under quiescent conditions after initial 10 minutes water bath sonication as described in Chapter 2.10.2 using 0.5% (w/w) of aSyn fibrils (hsAsyn, lsAsyn, PD, MSA and DLB) as seeds in the presence of 1:30 MTSL-labeled aSyn-T54C/A90C following an established protocol of Pornsuwan S. et al.[165]. The total aSyn concentration was 200 µM, 193.3 µM of aSyn and 6.7 µM of MTSL-labeled aSyn-T54C/90C. MTSL-labeled aSyn, see Figure 2-8, was provided by Stefan Becker and Karin Giller (NMR2, Max-Planck-Institute for Biophysical Chemistry, Göttingen, Germany). The mutant protein aSyn-T54C/A90C was constructed using the QuikChange site-directed mutagenesis kit (Stratagene), and the introduced modifications were verified by DNA sequencing. Protein expression and purification was performed as described[38]. The reaction of the aSyn-T54C/A90C mutant protein with the nitroxide spin label MTSL was carried out as described[30].

In brief, using size exclusion chromatography (PD-10 columns, Amersham Pharmacia Biosciences) the reducing agent DTT was removed from the buffer before labeling procedure. The α-synuclein mutant (aSyn-T54C/A90C) was then equilibrated in Tris-HCl buffer (20 mM Tris-HCl, 100 mM NaCl, pH 7.5) in presence of 5-fold molar excess of MTSL. The reaction was performed at 4 °C and stopped after 16 hours by removal of unreacted MTSL spin label using again PD-10 columns. The spin-labeled aSyn-T54C/A90C was concentrated using Microcon YM-3 (MWCO: 3 kDa) centrifugal filters (Amicon).

After fibril formation the fibrils were pelleted by UC (Optima MAX-XP, TLA 100.3 rotor, 55,000 rpm, 25 °C, 2 hours) and additionally washed with a fully-deuterated 50 mM HEPES, 100 mM NaCl, pD 7.81 buffer following a final harvest step of 1 hour. The pellet was shock-frozen in liquid nitrogen and stored at -80 °C. For EPR measurements the respective fibril pellets were thawed at RT and resuspended in 30 µl final volume D_2O supplemented with 10% deuterated glycerol-d_8 and 15 µL were loaded into quartz tubes with an outer diameter of 1.6 mm and an inner diameter of 1.1 mm.
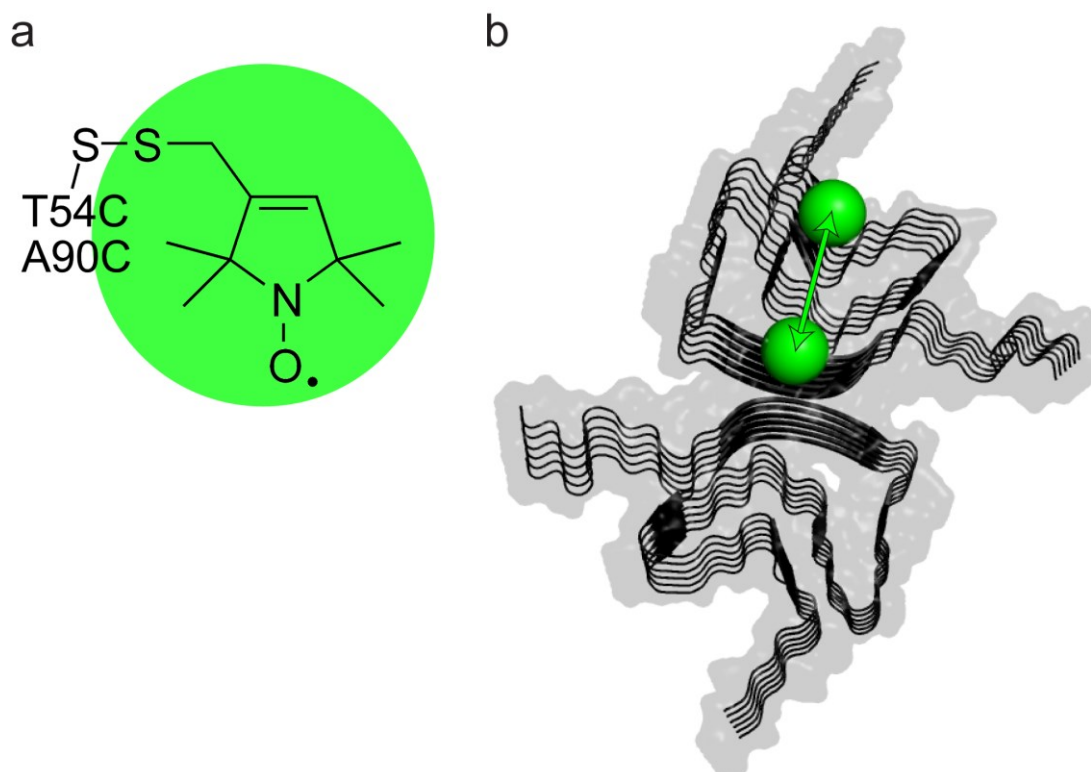
Figure 2-8. MTSL-labeled aSyn A90C/T54C incorporated into fibril structure at 1:30.
(a) MTSL-label attached to cysteine side chain of T54C and A90C mutations of aSyn. (b) Distance determination by EPR indicated with arrow between the two label positions in the structure of aSyn fibrils (PDB: 6A6B).

EPR measurements were done by Shu-Hao Liou (EPR spectroscopy, Max-Planck-Institute for Biophysical Chemistry, Göttingen, Germany). Room-temperature continuous wave EPR spectra were recorded on an EleXsys E500 spectrometer at X-band (9.8 GHz), equipped with a Super-High Q resonator (ER4122SHQE). Experimental conditions: microwave (MW) power 2 mW, modulation amplitude 5 G, conversion time 10 ms and 150 scans. Continuous wave EPR spectra were simulated using the program 'Chili' in Easyspin software (version 5.1.12)[166].Two nitroxide species with different weights were used in the simulation. After initial estimation of weights, multiple least-square optimizations were performed, in order to obtain the correlation times and weights for different nitroxide dynamics. For the fitting procedure, hyperfine and g values as well as peak-to-peak line widths were kept within a range consistent with previous reports[167].

Q-band (34 GHz) PELDOR measurements were performed on a Bruker EleXsys E580 spectrometer, equipped with a pulsed 170 W Q-band TWT-amplifier (Model 187Ka, Applied Systems Engineering Inc.) and an EN5107D2 EPR/ENDOR probe-head. PELDOR traces were measured using a four-pulse sequence ($\frac{\pi 1}{2} - \tau_1 -$

$\pi^1 - (\tau_1 + T) - \pi^2 - (\tau_2 - T) - \pi^1 - \tau_2 - [\text{echo}])$ with probe pulse (^{1}) and pump pulse (^{2})[168] . *T* was incremented in 8 ns steps. The pump pulse frequency was located at the maximum nitroxide absorption, determined by field-swept echo experiments. The probe pulse frequency was set to 80 MHz lower than the pump frequency (Δv = 80 MHz). The probe and pump pulse lengths were determined by a nutation experiment. The length of the probe π pulse was 26-32 ns, depending on the Q-value of the cavity. The $\frac{\pi}{2}$ pulse length was set to be identical to the length of π pulse by varying the pulse strength or amplitude (w_1). This procedure minimizes the overlap between the pump and probe pulse and thus attenuates the so-called '2+1' artifact. The π pulse at pump frequency was around 22-26 ns, and τ_1 was set to 200 ns, in order to suppress deuterium modulations. DeerAnalysis2018[137,138] was used to analyze PELDOR spectra. Background subtraction was performed using 2nd polynomial functions, followed by least-square fitting and Tikhonov regularization with L-curve selection.

3   Results

3.1   Biophysical characterization of monomeric aSyn

N-terminal acetylation is a post-translational modification commonly occurring in mammalian proteins[169]. α-synuclein isolated from humans is considered to be ubiquitously acetylated in its first methionine residue[60,170]. On top of that N-terminally acetylated α-synuclein (aSyn) has distinct biophysical properties shown for membrane binding[171] and protein-metal ion interactions[172]. In addition, aSyn is well known to show high variability in its aggregation behavior and the critical parameter besides working with protein of high purity is the absence of oligomeric higher molecular weight species that promote aggregation and eventually lead to inconsistent aggregation behavior of aSyn *in vitro*. Therefore, purified recombinant aSyn protein was studied with different biophysical techniques (SEC-MALS, mass spectrometry and NMR spectroscopy) to investigate protein purity, its conformational state as well as the completeness of the N-terminal acetylation introduced as described in section 2.6 (Protein preparation).

By protein purification, purities higher 95% were consistently obtained. The elution volume of aSyn from a size-exclusion column indicated an intrinsically disordered behavior.

3.1.1   SEC-MALS

Analytical size-exclusion coupled to multi-angle light scattering (SEC-MALS) showed that the recombinantly expressed aSyn elutes as a monomer from the analytical size exclusion column (Superdex 200 10/300 GL) under native-like aqueous conditions in solution. The detected Z-average molar mass (M_z) for aSyn was 14.1 ± 1.38 kDa using the RI detector for concentration determination and three light scattering detectors (45°, 90° and 135° angle), see Figure 3-1. The theoretical expected molecular weight for aSyn is 14.50 kDa. α-synuclein without N-terminal acetylation from a different protein preparation was analyzed for comparison; the detected molecular weight was 13.8 ± 1.37 kDa. The apparent molar mass of aSyn from SEC-MALS was 300 Da higher than for non-acetylated α-synuclein and aSyn also eluted slightly earlier from the column indicating a higher molecular weight. For cross-validation the UV signal was used as method for concentration determination showing also higher molecular mass for aSyn at a slightly lower absolute level (data not shown).

a

b

Mz: 14.1 ± 1.38 kDa
13.8 ± 1.37 kDa
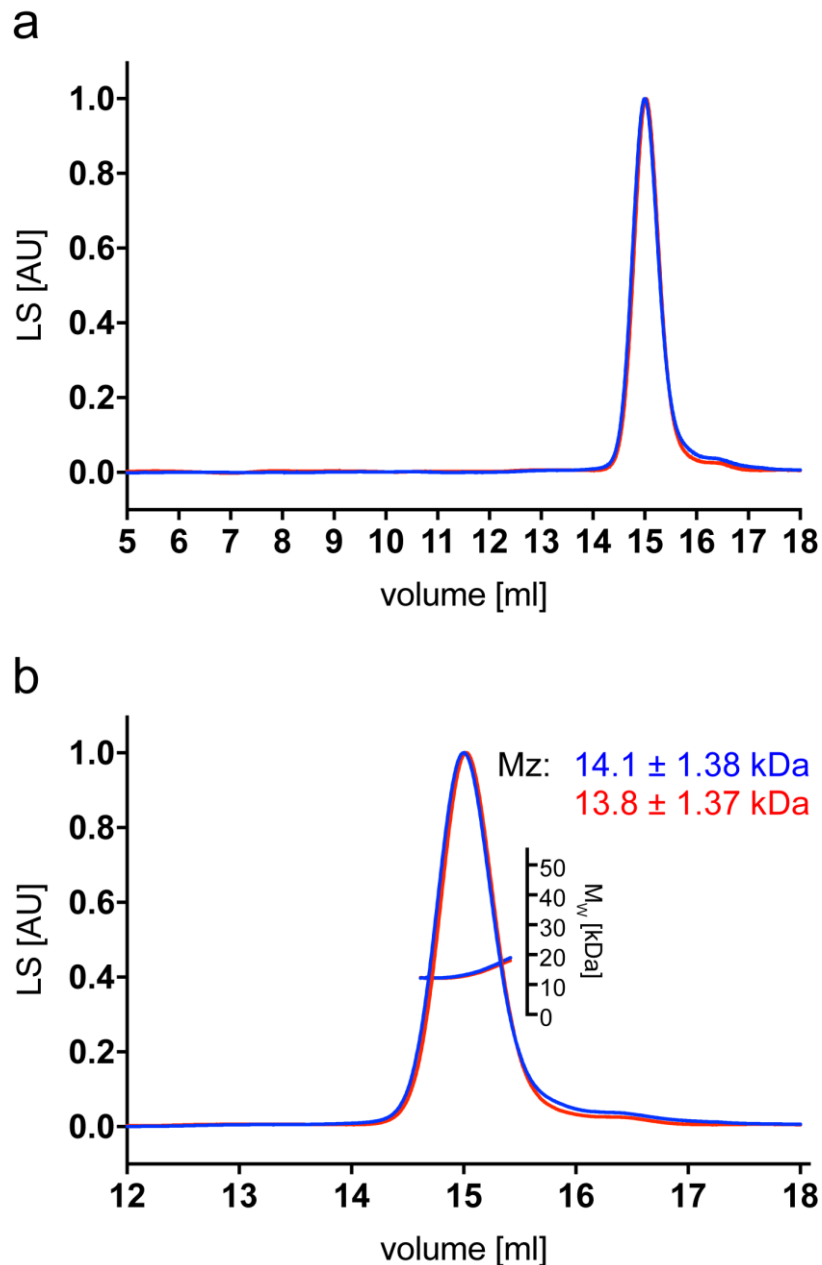
Figure 3-1. SEC-MALS of aSyn in comparison to non-acetylated α-synuclein.

(a) SEC-MALS run showing normalized light scattering signal of the 90° detector. (b) Zoom into the α-synuclein elution peak, M_z molecular weight determined by RI signal. Blue: aSyn, red: non-acetylated α-synuclein.

3.1.2   Mass spectrometry

To further validate the purity of the protein preparation as well as the completeness of the introduced N-terminal acetylation, HPLC in combination with mass spectrometry (MS-ESI) was chosen. A single peak eluted from the column with a retention time of 8.74 min, the detected molecular mass was 14.505 kDa.
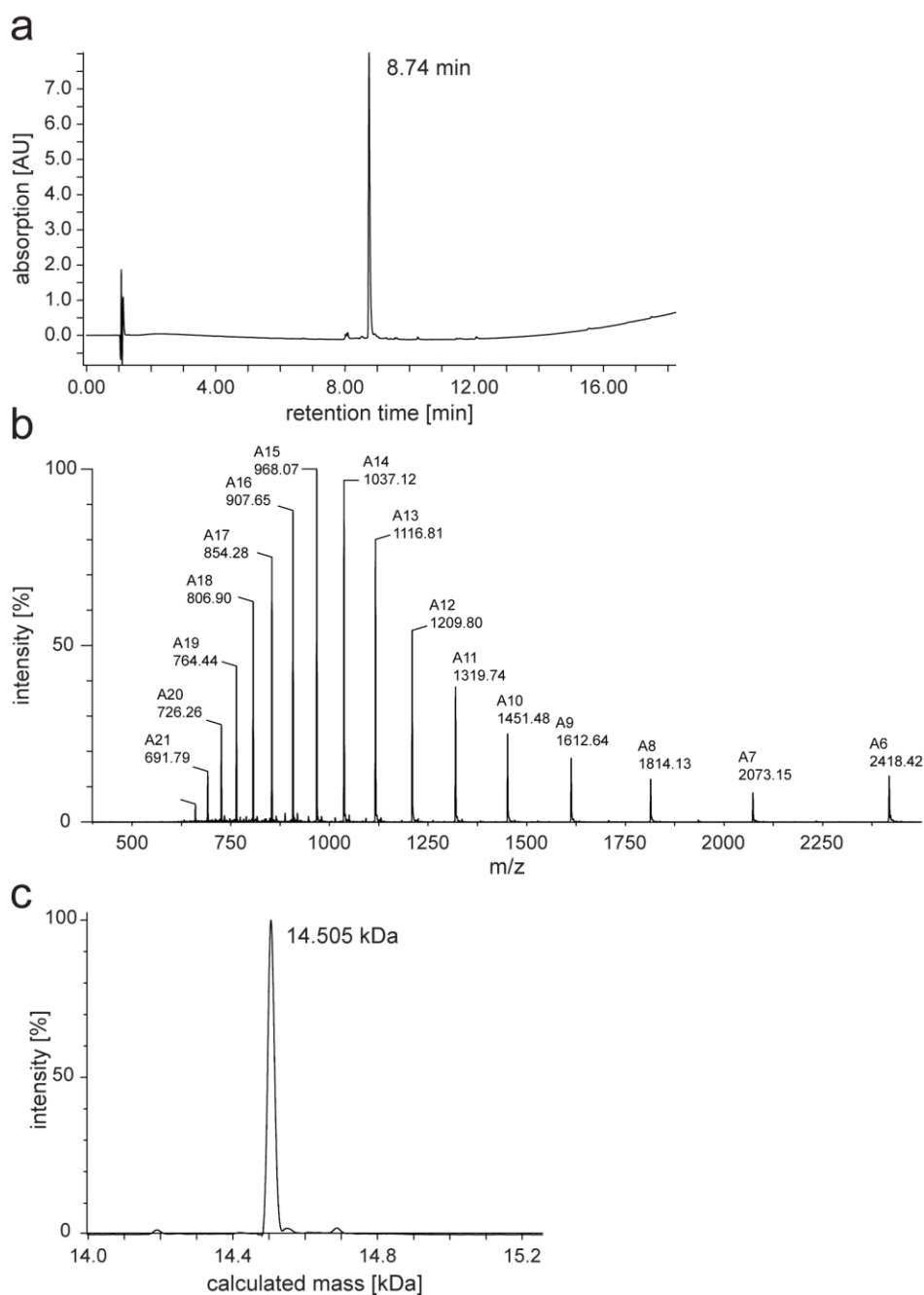
Figure 3-2 Validation of N-terminal acetylation of aSyn by mass spectrometry.

(a) HPLC run of aSyn. (b) m/z spectrum of aSyn. (c) Calculated average mass for HPLC elution.

3.1.3 N-terminal acetylation by NMR

Since the post-translational modification (PTM) of N-terminal acetylation changes the chemical environment of the initial aSyn residues and introduces structural perturbations in the ensemble due to higher rigidity of the N-terminus, two-dimensional heteronuclear correlation NMR experiments (^{1}H-^{15}N HSQC) are sensitive to it and allow validation of N-terminal acetylation (Figure 3-3).
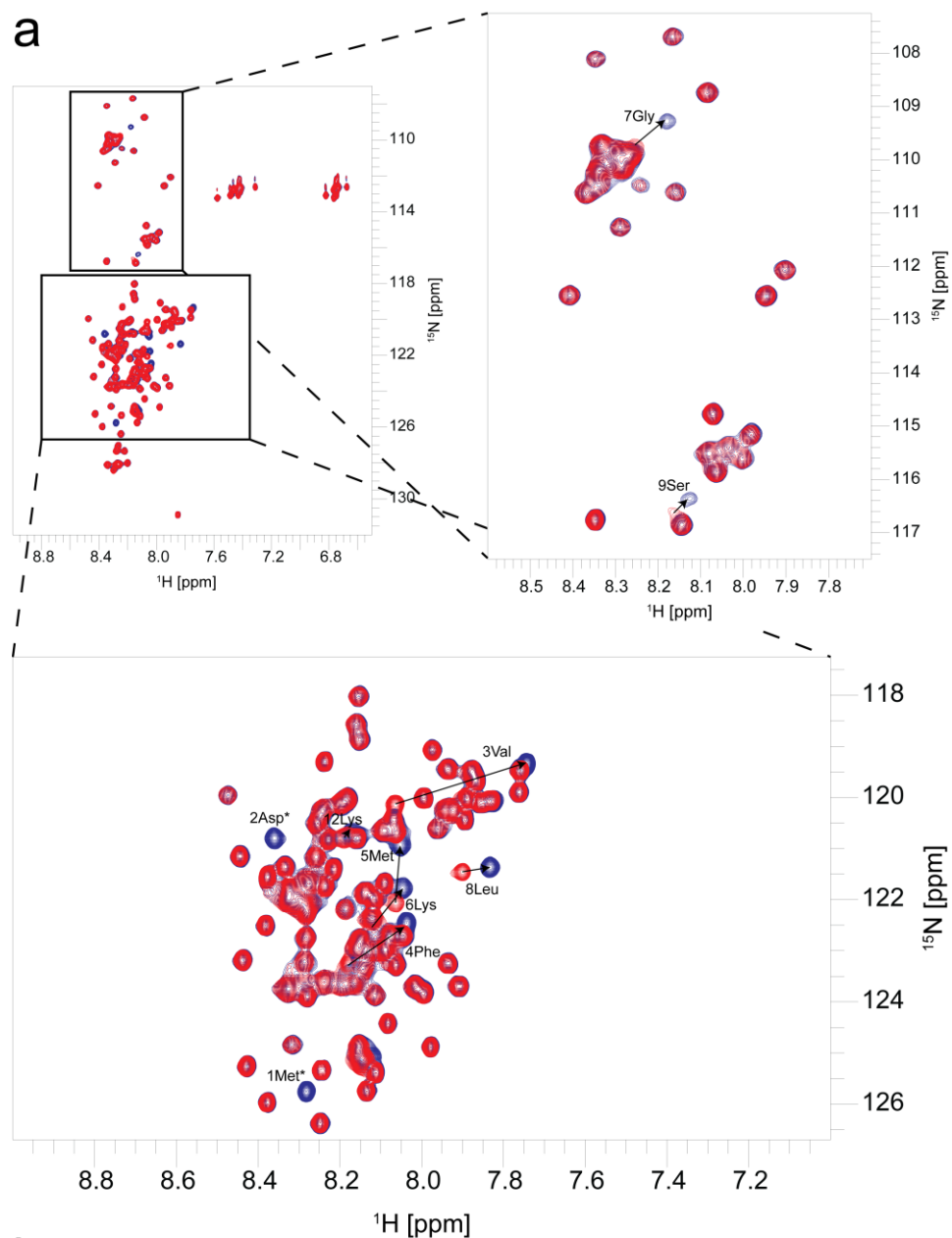
Figure 3-3. N-terminal acetylation validated by NMR.

(a) ^{1}H,^{15}N-HSQC spectra at 288 K in HEPES buffer (50 mM HEPES, 100 mM NaCl, pH 7.4, 0.01% NaN$_3$). Perturbed residues are indicated in two regions. aSyn in blue, non-acetylated α-synuclein in red. (b) Intensity ratio in orange, chemical shift perturbation in green.

3.2 Amplification of aSyn aggregates

3.2.1 Amplification of aSyn aggregates from brain extracts

aSyn aggregates from brain extracts of seven patients diagnosed with either PD, MSA or DLB (Patient material: Table 3) were amplified using protein misfolding cyclic amplification (PMCA) at low concentration of 2.5 µM to prevent *de novo* aggregation. The PMCA end products were then used to seed aggregation under quiescent condition in the presence of unlabeled and ^{15}N-labeled aSyn at 250 µM. The seeded amplification step was introduced to obtain sufficient quantities of PMCA-amplified amyloid fibrils for further structural analysis.
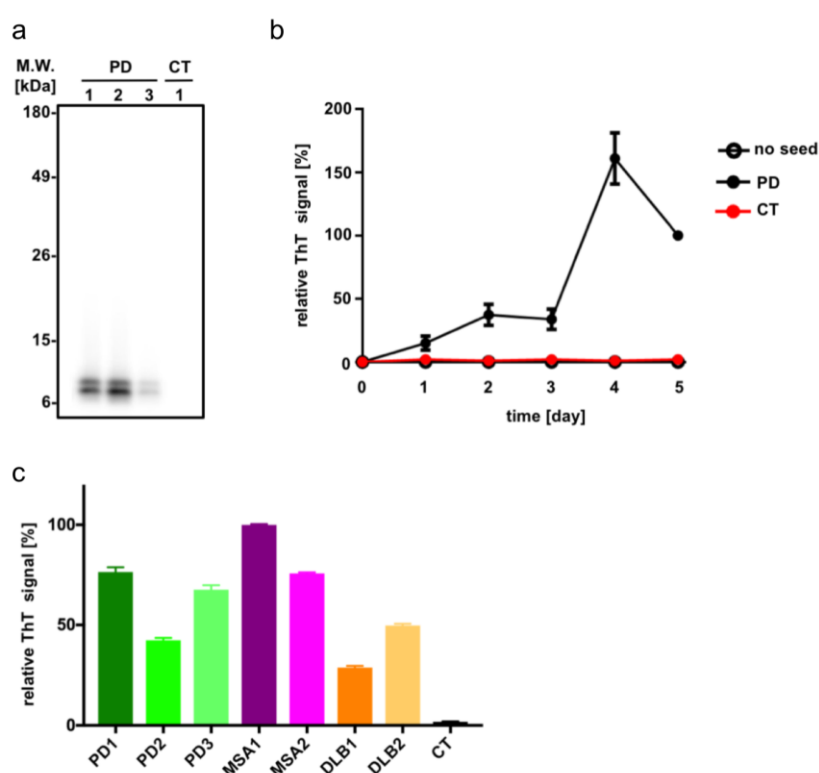
Figure 3-4. Amplification of aSyn from brain extracts.

(a) Immunoblotting of PMCA-amplified aggregates with PK digestion. Similar PK-resistant signals were detected in all three PD samples (PD1-PD3), whereas nothing remained in the control sample (CT; brain extract from an individual, in which a synucleinopathy was excluded). **(b)** ThT-binding kinetics of recombinant aSyn with or without nominated PMCA products as seeds. ThT-intensities for the three PD samples (PD1-PD3) were averaged and used to derive error bars. **(c)** Relative ThT fluorescence after seeding with different PMCA products. Error bars indicate standard deviation over three fluorescence measurements for each sample.

The Korean collaborators characterized the PMCA end product seeded aSyn aggregates by Western blot analysis after proteinase K (PK) digestion with a monoclonal aSyn-specific antibody (BD Biosciences, #610787) and monitored the seeded aggregation kinetics by thioflavin T binding assay as described by Jung et al.[106].

Figure 3-4 a shows the amplification of PK-resistant aSyn aggregates in the case of PD patients (PD1, PD2 and PD3) using 0.5 % (w/w) PMCA end products as seeds for seeded aggregation. The control brain extract (CT) PMCA end product in contrast did not result in the formation of PK-resistant aSyn aggregates, indicating the absence of competent aSyn seeds in the brain tissue. In addition, in panel b of Figure 3-4 the formation of ThT positive aSyn aggregates was monitored over time during the seeded aggregation amplification step. Again, the PMCA end product of control brain did not induce aSyn fibril formation, the ThT signal stayed low. The PMCA end products of the three PD patients however induce the formation of ThT-positive aSyn aggregates. Because recombinant aSyn in the absence of seeds did not form ThT-positive aSyn aggregates, *de novo* aggregation could be ruled out.

3.2.2 Aggregation of high and low salt *in vitro* polymorphs

Besides the amplification of aSyn form brain extracts, recombinant aSyn was additionally aggregated under two different, previously described buffer conditions through agitation[117,122] but in the absence of PMCA-seeds. These two types of aSyn fibrils – obtained through *de novo* aggregation at ionic strengths of either 5 mM (low salt; lsAsyn) or 200 mM (high salt; hsAsyn) – differ in their conformations and neurotoxic phenotypes[117,122]. The *de novo* aggregated fibrils were subsequently used to seed aggregation of monomeric aSyn (unlabeled and ^{15}N-labeled).

3.3 Characterization of aSyn aggregates by EM

Negative stain transmission electron microscopy (EM) with uranyl acetate was used to characterize the nature of aSyn aggregates seeded by PMCA end products for the different patients. For the high and low salt polymorphs (hsAsyn and lsAsyn), electron micrographs were already published by Bousset et al.[122]. In addition, EM was a valuable tool for quality control of the seeded aggregations as a yes/no readout for the fibrillization of aSyn.

3.3.1 EM of aSyn aggregates amplified from patient brain material by PMCA

The PMCA-seeded aSyn aggregates are genuine amyloid fibrils confirmed by negative-stain transmission EM. Figure 3-5 show representative micrographs for one patient of each type of synucleinopathy (PD1, MSA1 and DLB1). The aSyn fibrils have a diameter of ~10 to 12 nm.
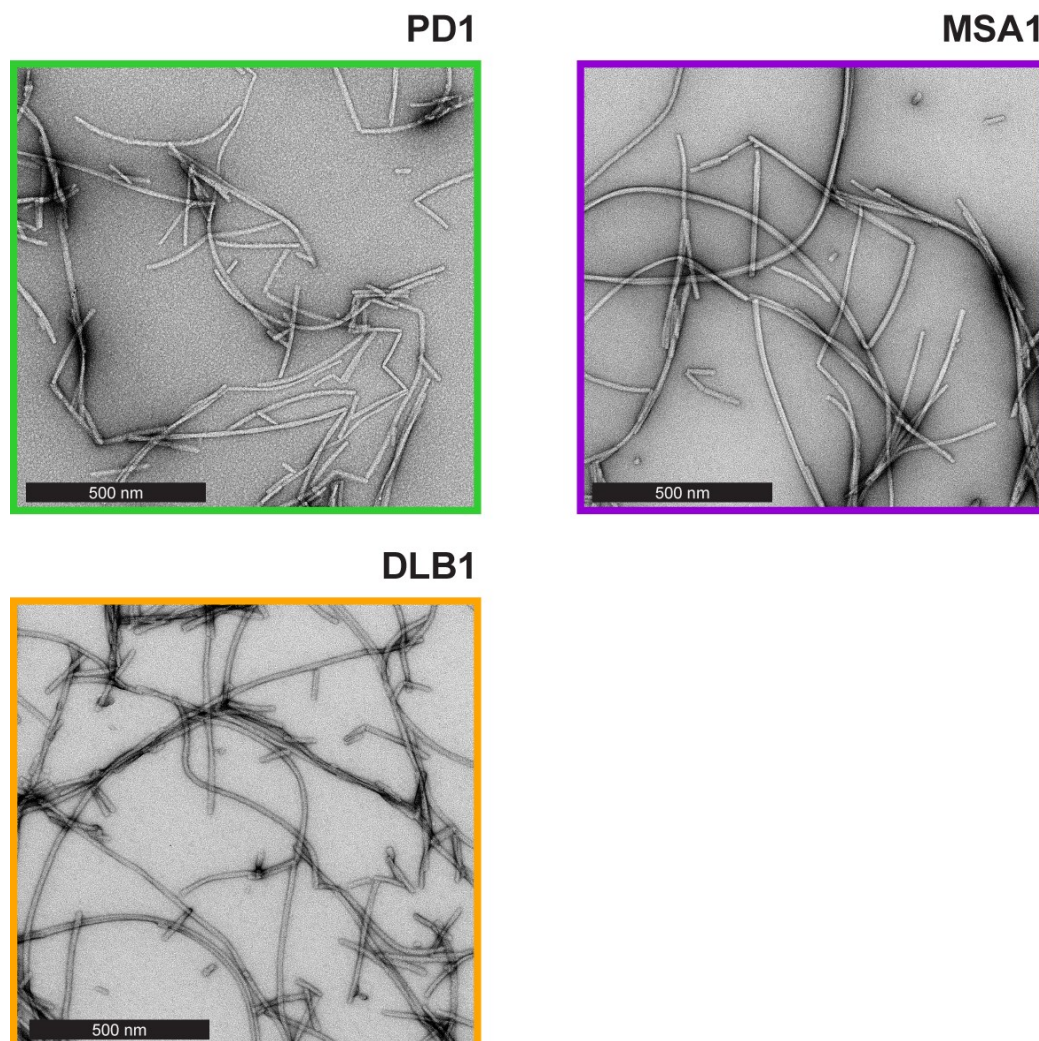
Figure 3-5. Electron micrographs of aSyn fibrils amplified from brain extracts.
Electron micrographs belong to fibrils amplified from brains extracts of PD, MSA and DLB.

aSyn fibrils extracted from patients' brains are polymorphic with fibril diameters of ~5 and ~10 nm[4].

3.3.2 EM pictures of high and low salt *in vitro* polymorphs

The high salt polymorph, hsAsyn, shows fibrils with a diameter of ~10 to 12 nm as well as small single filaments of ~5 to 6 nm.
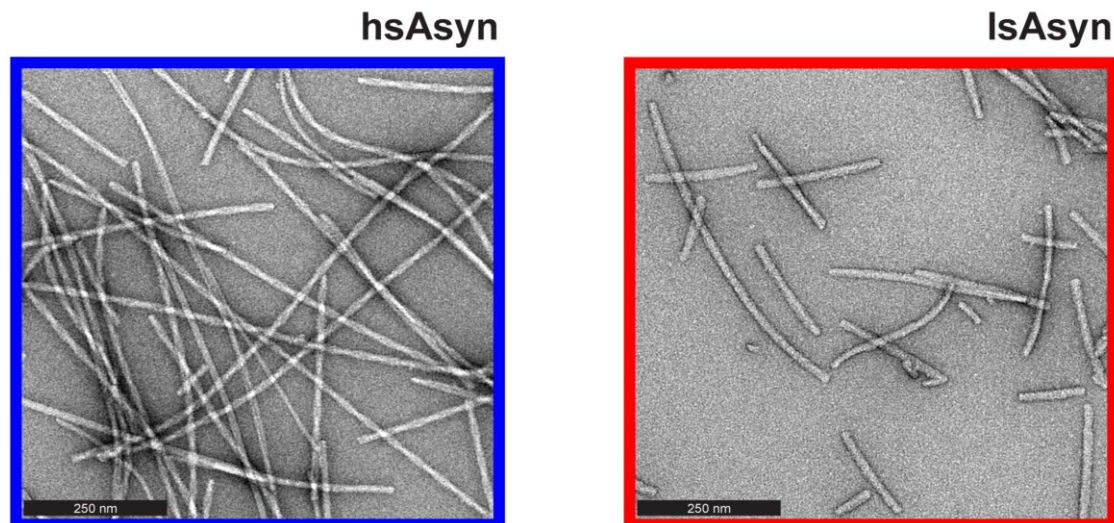
Figure 3-6. Electron micrographs of aSyn *in vitro* polymorphs.
Electron micrographs of the two *in vitro* aSyn polymorphs hsAsyn (50 mM Tris-HCl, 150 mM KCl, pH 7.5, 0.02 % NaN3) and lsAsyn (5 mM Tris-HCl, pH 7.5, 0.02 % NaN$_3$).

3.4 Secondary structure analysis of aSyn fibrils by CD spectroscopy

Having obtained genuine aSyn fibrils in appearance by TEM characterization, circular dichroism (CD) was used to characterize their secondary structure. Figure 3-7 summarizes the results. The CD spectra show an amyloid β-sheet structure with a characteristic minimum at ~220 nm and a maximum at ~195 nm. Random coil conformation of non-aggregated intrinsically disordered monomeric aSyn in solution was ruled out in the absence of the characteristic minimum at ~200 nm.
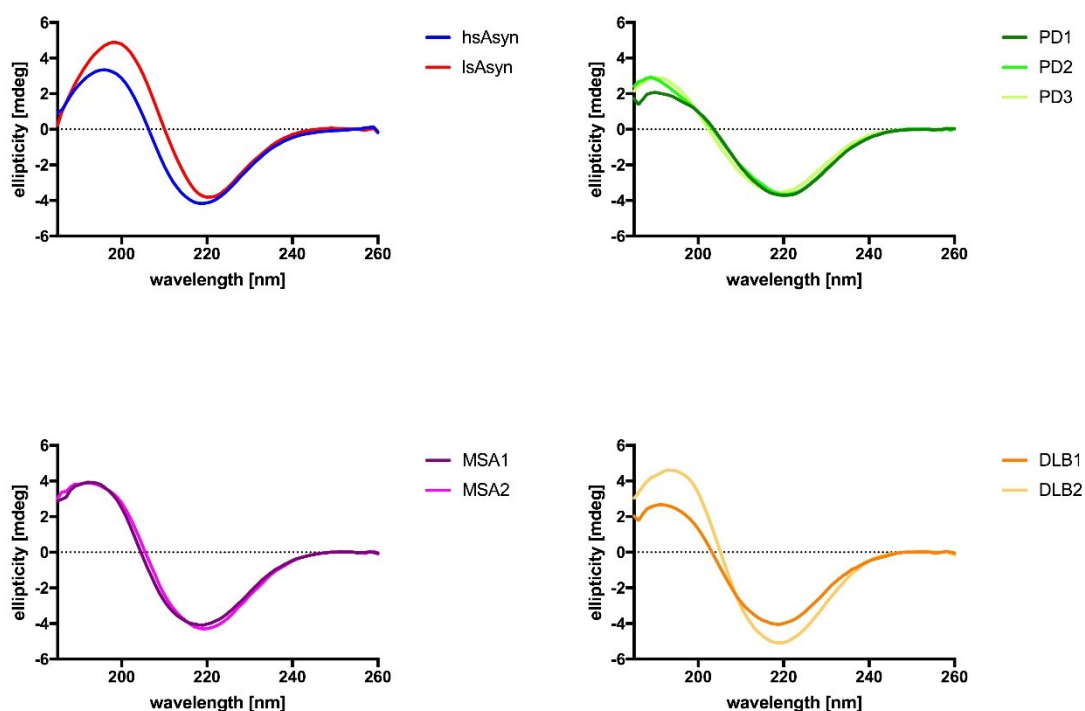
Figure 3-7. CD spectra of aSyn fibrils.

CD spectra of the two *in vitro* aSyn polymorphs (hsAsyn/blue, lsAsyn/red) and amyloid fibrils amplified from brain extracts of different patients (PD/green, MSA/purple, DLB/orange).

3.5 Detection of conformational differences by fluorescent dye binding

Fluorescent dyes that bind to specific amyloid conformations are able to differentiate prion strains and determine intersubject variability of amyloid-β aggregates in Alzheimer's disease[130,131]. To investigate the presence of conformational differences between aSyn fibrils, fluorescence measurements in the presence of the amyloid-binding dyes curcumin, FSB and HS-68[130,132] were performed.

3.5.1 Curcumin binding to aSyn fibrils

Figure 3-8 a and b show the fluorescence spectrum of curcumin upon binding to aSyn fibrils for two independent measurements of the same sample fibril harvest. Both spectra show two local maxima, one at ~519 nm and the other at ~593 nm. When normalized to the maximum observed for the hsAsyn polymorph at ~519 nm, a clear difference in the intensity of the maximum at ~593 nm was evident between hsAsyn and lsAsyn.
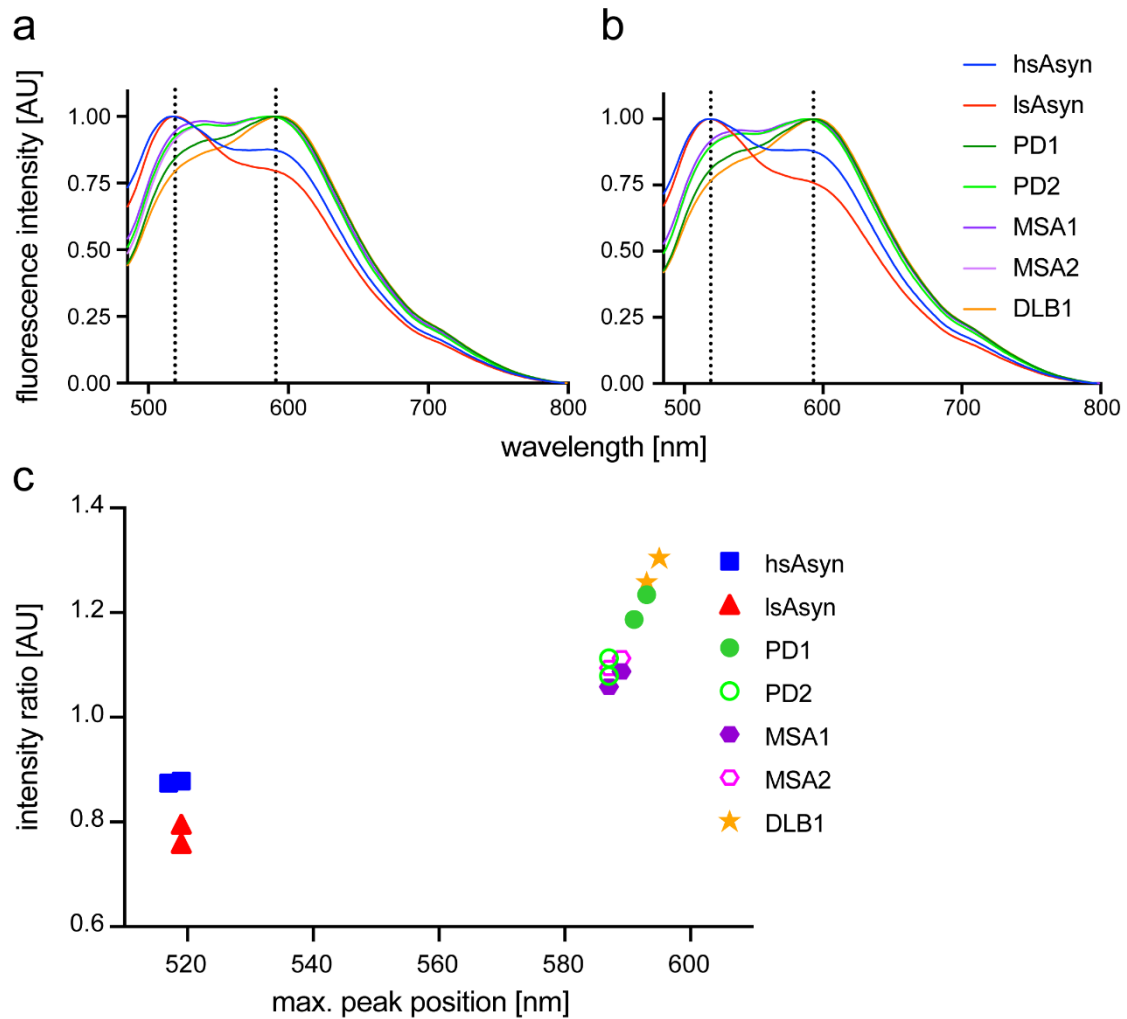
Figure 3-8. Curcumin binding to aSyn fibrils.

(a) and (b): Normalized fluorescence spectra of curcumin in the presence of two *in vitro* aSyn polymorphs (hsAsyn/blue, lsAsyn/red) and amyloid fibrils amplified from brain extracts of different patients (PD/green, MSA/purple, DLB/orange). (c) Two-dimensional analysis of fluorescence properties of curcumin in the presence of different aSyn fibrils. The position of the global maximum is correlated to the ratio of fluorescence intensities at ~519 nm and ~593 nm (see panel a and b). For each sample, fluorescence measurements were performed independently two times (two symbols each; representing intrinsic variability in the fluorescence measurements).

While the *in vitro* polymorphs displayed the maximal curcumin fluorescence at ~519 nm, this maximum was shifted to ~593 nm for the brain extract-amplified fibrils (Figure 3-8 a,b). Correlation of the position of the global maximum with the intensity ratios of the curcumin fluorescence at ~519 nm and ~593 nm further distinguished brain extract-amplified fibrils from the *in vitro* polymorphs (Figure 3-8 c). Differences in the fluorescence spectra of samples amplified from PD, MSA and DLB brain extracts were also evident, including differences in the normalized curcumin fluorescence at ~519

nm (Figure 3-8 c). The raw absolute fluorescence is shown exemplarily for the graph of Figure 3-8 b in Figure 3-9.
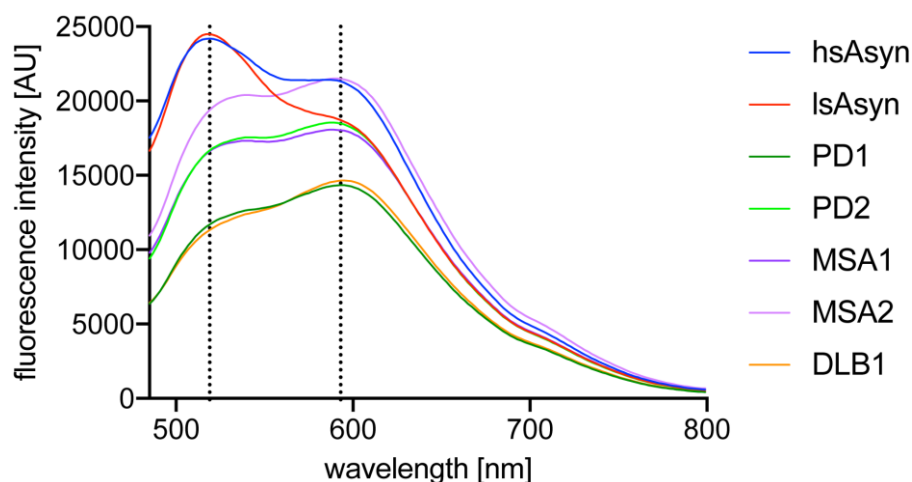
Figure 3-9. Absolute fluorescence of curcumin binding to aSyn fibrils.

Data shown here refers to the normalized graph of Figure 3-8b.

3.5.2   FSB and HS-68 binding to aSyn fibrils

In agreement with curcumin/aSyn fibril interactions, FSB also shifts the fluorescence emission maximum to longer wavelength in case of the brain extract-amplified fibrils. Differences in the fluorescence spectra of samples amplified from PD, MSA and DLB brain extracts were also evident in the absolute fluorescence intensities of FSB, see Figure 3-10 a. HS-68, Figure 3-10 b, shows stronger interaction with the high salt polymorph, hsAsyn. The fluorescent dyes indicated the presence of differences in the fibril conformations, mainly pointing out at differences between the *in vitro* polymorphs and the brain extract-amplified fibrils. In addition, the binding studies hinted towards conformational differences within the brain extract-amplified fibrils.

a

b
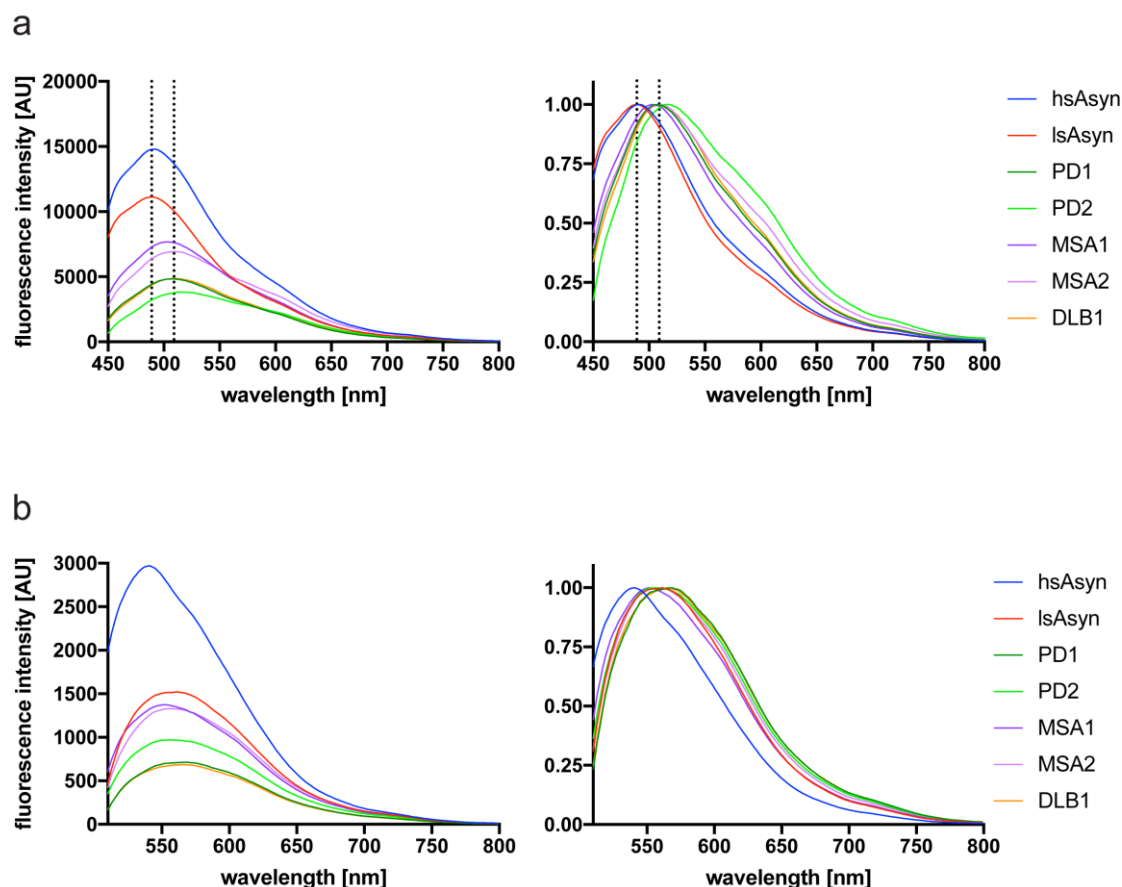
Figure 3-10. FSB and HS-68 binding to aSyn fibrils.

Fluorescence spectra of FSB (a) and HS-68 (b) in the presence of different amyloid fibers. Absolute and normalized fluorescence intensities are shown in the left and right column, respectively. The fluorescence maximum of FSB is shifted to longer wavelength in the presence of amyloid fibrils amplified from patient material (PD/green, MSA/purple, DLB/orange) when compared to the two *in vitro* polymorphs hsAsyn (blue) and lsAsyn (red). The average wavelengths of the fluorescence maxima of the two *in vitro* polymorphs (~ 489 nm) and the aSyn fibrils amplified from patient brain extracts (~ 509 nm) are marked by two dashed, vertical lines.

3.6   Hydrogen-deuterium exchange coupled to NMR

In order to gain insight into the conformational differences between different aSyn fibrils, hydrogen-deuterium (HD) exchange studies were conducted. When HD exchange studies are combined with methods of rapid fibril dissociation and liquid-state NMR spectroscopy, deuterium incorporation levels can be determined with single-residue resolution[162-164]. In the following sections the method is explained in detail, showing an in-depth analysis for a high salt polymorph.

3.6.1 Assignment of aSyn resonances in dissociation buffer

An important prerequisite was the assignment of 131 (including prolines) out of 140 residues of aSyn in guanidinium thiocyanate dissociation buffer (4 M GdSCN, 0.4% formic acid, pH 2.5) with the help of 3D HNCO, HN(CA)CO, HNCA, HN(CO)CA and HNCACB experiments as described in *section 2.15.1 – Resonance assignment* and summarized in *Appendix: 7.2*. On one hand those assignments are essential for the analysis of HD exchange experiments and the calculation of initial protonation levels, on the other hand they allow analysis of the secondary structure of aSyn in the respective dissociation buffer. The presence of secondary structure elements would indicate intra- and potentially also intermolecular hydrogen bonds affecting the back-exchange processes. In order to rule out this possibility, the secondary chemical shift differences to random coil NMR chemical shifts corrected for sequence-dependence[161] are reported here for α-carbon- (Cα), carbonyl- (C') and β-carbon (Cβ) resonances of aSyn.
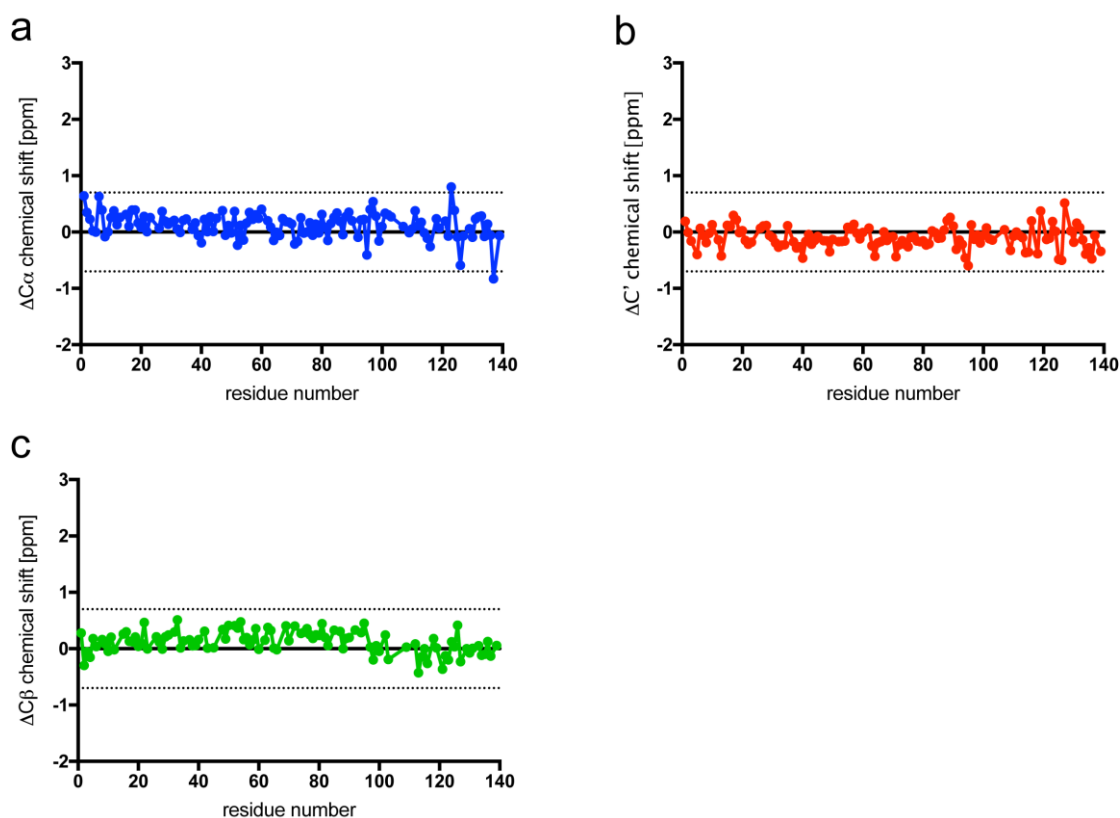
Figure 3-11. Secondary chemical shift differences.

(a) Cα-, (b) C'- and (c) Cβ-chemical shift differences.
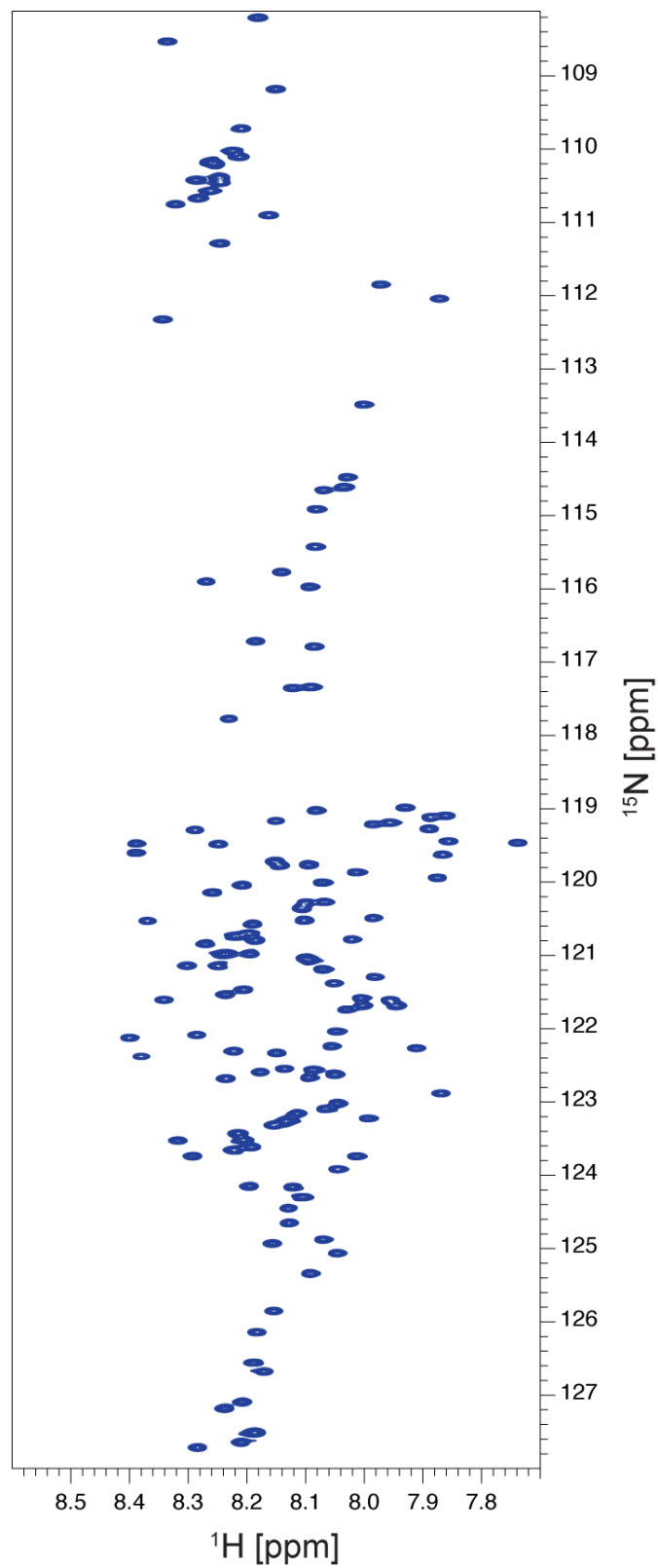
Figure 3-12. HSQC spectrum of aSyn in dissociation buffer.

Temp.: 276 K, 800 MHz, 600 μM aSyn in dissociation buffer (4 M GdSCN, 0.4% formic acid, pH 2.5).

The shift differences are small (Figure 3-11 a,b and c), therefore the presence of secondary structure elements could be ruled out. aSyn in the guanidinium thiocyanate dissociation buffer (Figure 3-12) behaves as a random coil and the buffer is suited for HD exchange measurements by NMR.

3.6.2   Hydrogen-deuterium back-exchange in dissociation buffer

Previous HD exchange studies conducted on *in vitro* aggregated aSyn fibrils established that a forward exchange time of 1.5 days allows robust determination of residue-specific protonation levels[162,164]. The data analysis from the acquisition of real-time HSQC spectra to the calculation of residue-specific protonation levels is shown here for *in vitro* seeded aSyn fibrils under high salt buffer conditions (50 mM Tris-HCl, 150 mM KCl, pH 7.4, 0.02% NaN_3), hsAsyn.

The forward-exchanged hsAsyn pellet was taken from the -80 °C storage, thawed and resuspended in dissociation buffer, followed by sample transfer to the NMR tube. All steps were performed on ice to quench the back-exchange kinetics. The NMR sample was quickly inserted into a pre-shimmed and temperature-equilibrated (276 K) 800 MHz cryoprobe-equipped NMR spectrometer and a series of HSQC spectra were recorded monitoring in real-time the back-exchange in dissociation buffer (H: 40%, D: 60%) as described in detail in the *Material and methods* section.

Figure 3-13 shows on the left side in blue the initial HSQC spectrum of the real-time series, the absolute intensities by height are a close approximation of the intensity values at t_0 that report the initial protonation levels for each residue after forward exchange. The light blue spectrum on the right side of Figure 3-13 shows the final HSQC spectrum of the HSQC series, representing the fully back-exchanged hsAsyn spectrum where the intensities report the protonation level of the dissociation buffer.

The series of HSQC spectra was converted into an intensity table using the resonance assignment for aSyn in dissociation buffer. Peaks were picked in the final HSQC spectrum and centered to the maximum peak height. Using nmrPipe's *seriesTab* script, the intensity values for each residue of every HSQC plane were extracted. The intensity values of the final HSQC of each aSyn residue were set arbitrarily to 1 and the series normalized accordingly. Knowing the initial time delay from pellet resuspension to the start of the first HSQC as well as the duration of each HSQC pulse program, the table can be plotted against the absolute time axis shown in Figure 3-14. To back-calculate the initial intensity level of each aSyn residue, the time curves were fitted to a single exponential decay and the relative intensity values for t_0 (t = 0 hours) were reported. The fit is shown as a continuous line in Figure 3-14.
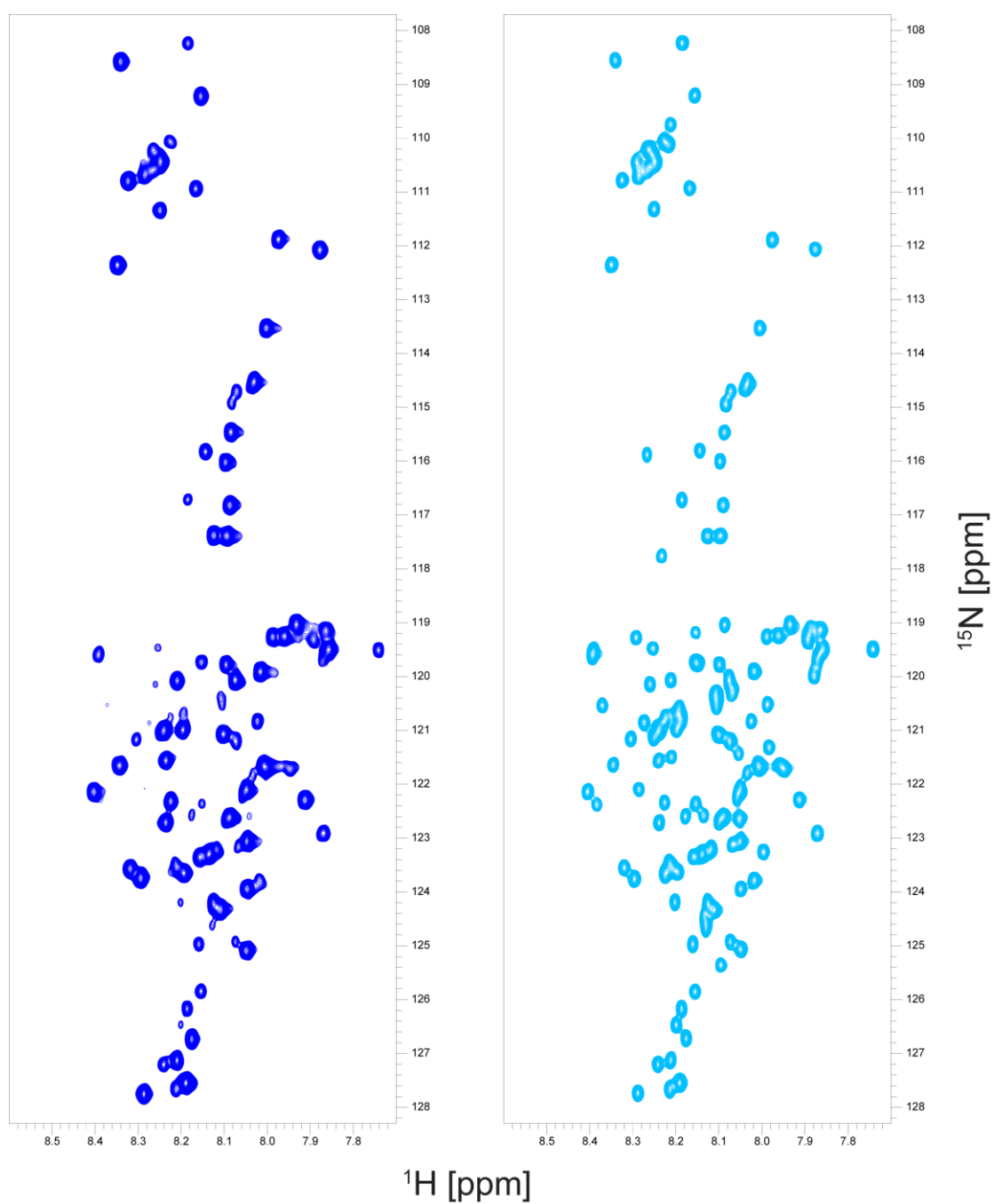
Figure 3-13. HD back-exchange monitored by HSQCs in real-time.

Full ^{1}H-^{15}N HSQC spectra recorded after fibril dissociation at the beginning (left) and end (right) of the back-exchange period for the hsAsyn polymorph.
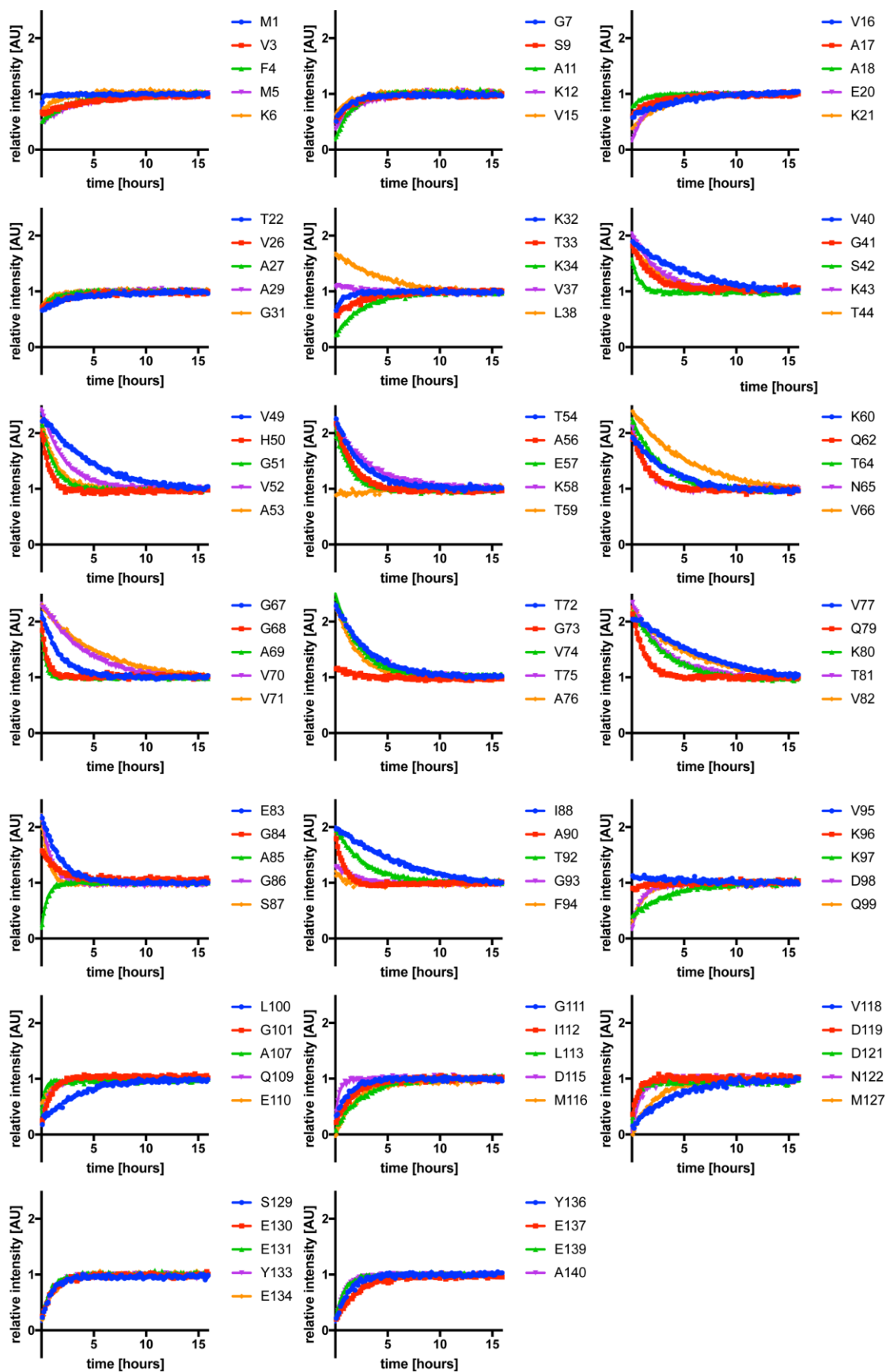
Figure 3-14. Back-exchange curves of hsAsyn polymorph.

99 non-overlapping HSQC cross peaks were included in analysis.

All hsAsyn residues converged within the duration of the real-time measurement to the final normalized intensity value 1. Differences in the rate constant are sequence- and residue type-dependent. The upper part of Figure 3-15 shows the back-fitted intensity values at t_0. The lower part the absolute protonation levels in % ^{1}H.
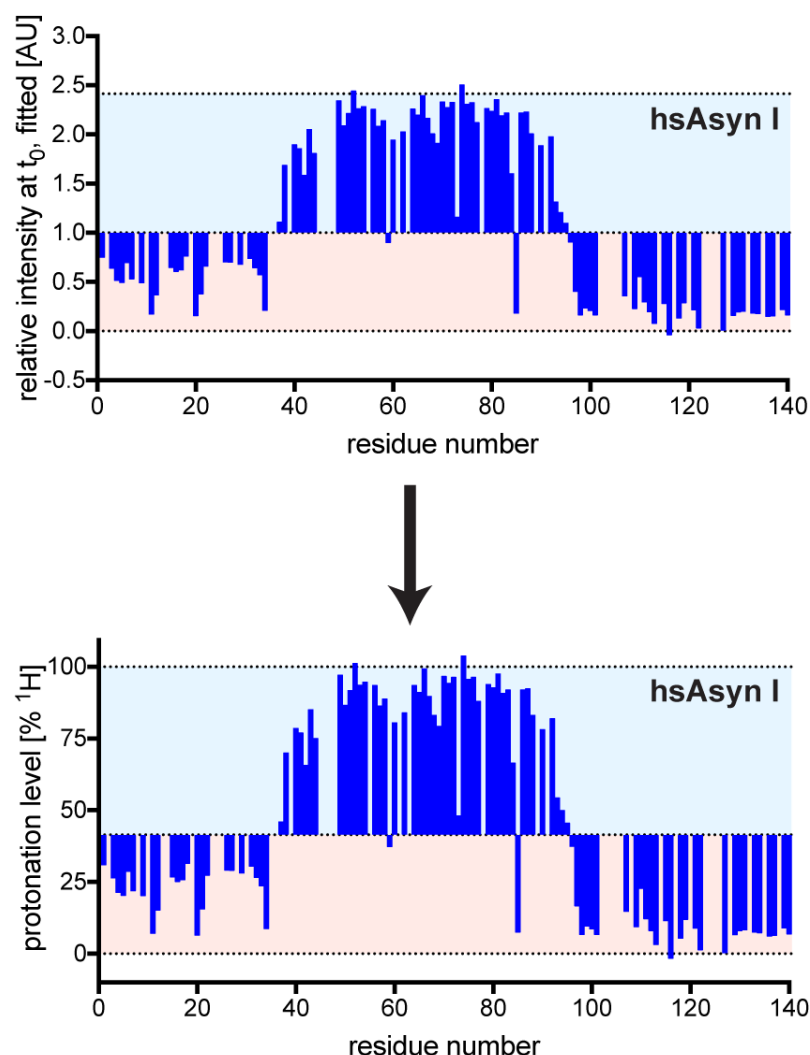
Figure 3-15. Data transformation from intensities to absolute protonation levels.
Arrow indicates transformation operation. The average of the sequence-independent residues of highest intensity is calculated and set as a protonation level of 100 % ^{1}H. The relative intensity 1 reports the absolute protonation level of the dissociation buffer, in case of hsAsyn 59% D_2O.

The structural implications of the detected protonation levels after HD exchange are discussed in the next section.

3.7 HD exchange profile of the *in vitro* high and low salt polymorphs

3.7.1 HD exchange profile of the high salt *in vitro* polymorph

a
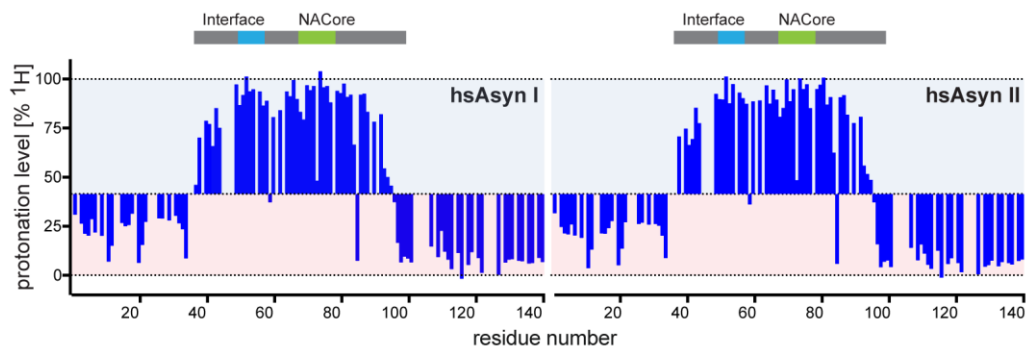
b
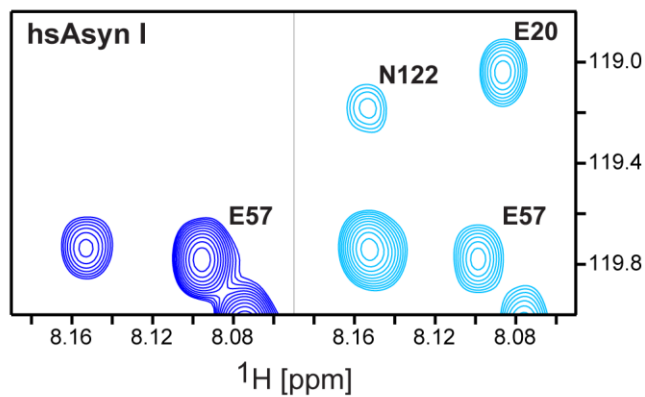
c
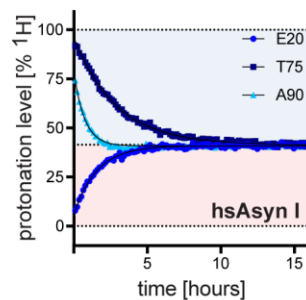
d
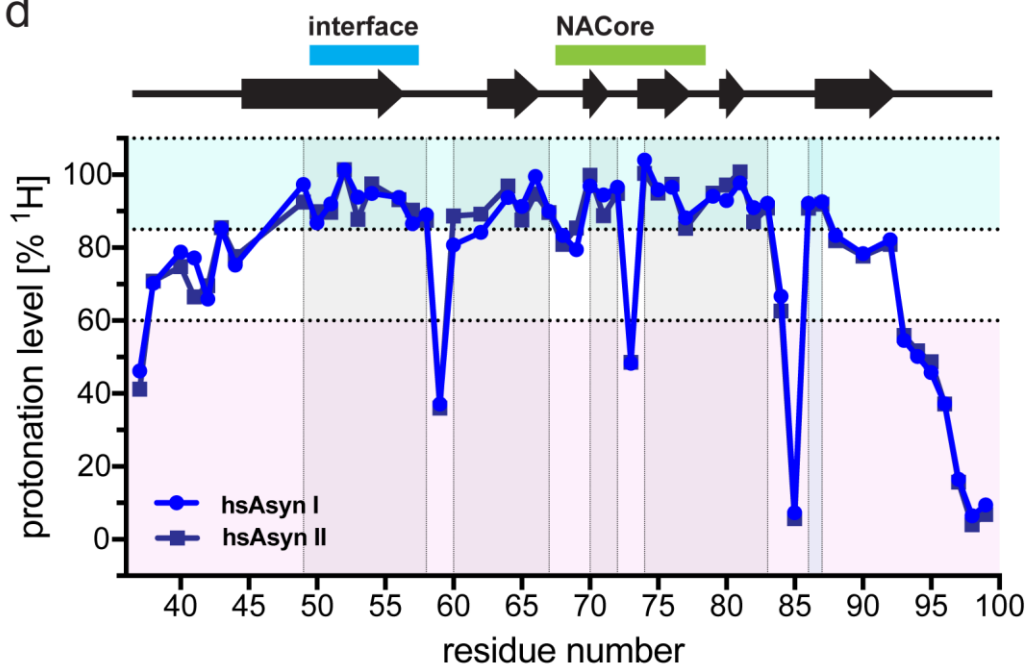
Figure 3-16. Residue-specific protonation levels in high salt polymorph (hsAsyn) fibrils by HD exchange.

(a) HD-exchange profiles of two independently seeded hsAsyn fibrils using the same *de novo* aggregates as seeds, labeled as hsAsyn I and II. (b) Selected region from ^{1}H-^{15}N correlation spectra recorded after fibril dissociation at the beginning (left) and end (right) of the back-exchange period for hsAsyn I fibrils, in detail see Figure 3-13. (c) Time-dependent back-exchange of selected residues (E20, T75 and A90) for hsAsyn I fibrils, in detail see Figure 3-14. (d) Detailed HD exchange profile of the *in vitro* polymorph (hsAsyn I in blue and hsAsyn II in dark blue) within the region that forms cross-β-sheets in the cryo-electron microscopy structure of hsAsyn (PDB code: 6A6B). NACore is the most hydrophobic part of the aSyn sequence and the interface between two aSyn filaments as seen in the PDB of 6A6B is marked, both in panel a and d above.

In agreement with previous data[162,164], it was found for the high salt polymorph that the fastest solvent exchange occurs in residues located in the ~40 C-terminal residues for which less than 25% of amide protons remained after 1.5 days of forward exchange in D_2O (Figure 3-16 a). Extensive incorporation of deuterium was also observed for the first 36 residues at the N-terminus of aSyn (Figure 3-16 a). In contrast, residues L38-V92 retained a large fraction of their amide protons after exchange in D_2O (Figure 3-16 d), indicating that these amide protons participate in hydrogen bonds. The hydrogen-bonded core of hsAsyn fibrils as determined by HD was consistent with those defined by solid-state NMR and cryo-electron microscopy for wild-type aSyn and aSyn(1-121)[133-135]. Figure 3-16 a-d show that protonation levels within the aSyn amyloid core were not uniform. Several residues within the region K43-S87 displayed little solvent exchange, with other residues retaining only ~60-85% of their amide protons (i.e. L38-T44, K60, Q62, G68-A69, G84, I88-T92) or even exchanging more than 60% (i.e. V37, T59, G73, A85, G93-Q99).

The structure of the hsAsyn *in vitro* polymorph (identical buffer conditions as used in the current study) has been recently determined by cryo-electron microscopy[135]. Figure 3-17 a shows the protonation levels determined by HD exchange in context of the cross-β-sheet structure of hsAsyn. Fast solvent exchange was undertaken by V37-T44 and G93-Q99, which are located in the N- and C-terminal parts, respectively, and are not surrounded by additional cross-β-sheet structure (Figure 3-17 a,b). A connection between solvent accessibility and differences in protonation levels was further supported by the finding that residues next to the hydrophilic channel[133-135,173] displayed decreased protonation levels (Figure 3-17 a). In addition, faster solvent exchange for some turn residues (e.g. T59, A85; Figure 3-17 a) was observed, potentially due to lower hydrogen bond strength[174]. In contrast, high

protonation levels for the residues A53-A56, which form the interface with a second filament in hsAsyn fibrils (Figure 3-17 a, Figure 3-16 d)[134,135] were detected. Although most residues within the amyloid core form hydrogen bonds to neighboring residues along the fibril axis (Figure 3-17 a,b), the analysis showed that HD exchange coupled to NMR spectroscopy provides a sensitive tool to characterize aSyn amyloid structure[163].
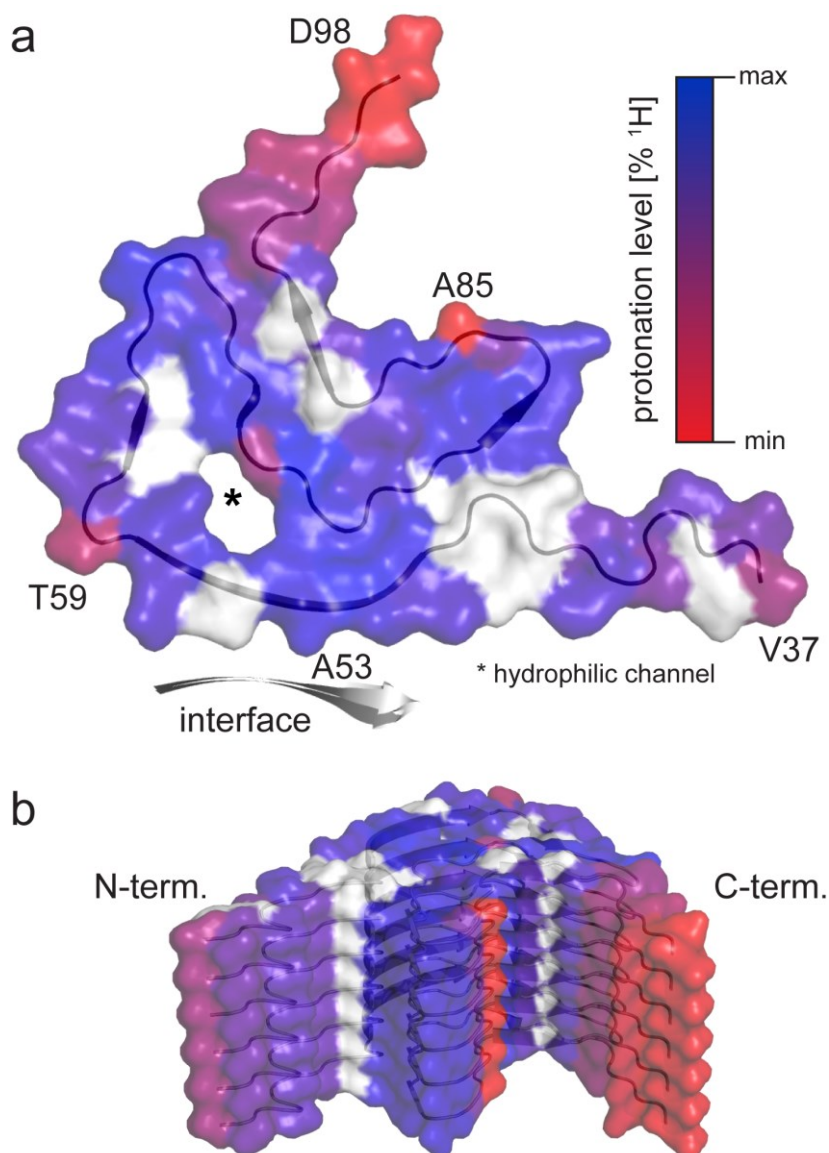
Figure 3-17. HD exchange profile mapped on high-resolution cryoEM structure.

(a) Mapping of residue-specific protonation levels of hsAsyn I (as shown in blue in panel a of Figure 3-16) on the structure of the hsAsyn filament (PDB code: 6A6B). The interface to the second filament, which involves A53, is marked. The scale bar indicates protonation levels relative to the minimum protonation level observed for V37-Q99. Residues with signal overlap were excluded from the analysis (shown in white). (b) Side view of (a).

3.7.2 Robustness of the high salt *in vitro* polymorph HD exchange profile

Here it is shown that HD exchange profiles of *de novo* aggregated and seed-derived hsAsyn fibrils were highly similar (Figure 3-18 a). The amyloid structure was thus propagated during seeding. In addition, *in vitro* aggregation and seeding in another high salt buffer used for the aggregation of brain-extract seeded aSyn fibrils resulted in a very similar HD exchange pattern (Figure 3-18 b).
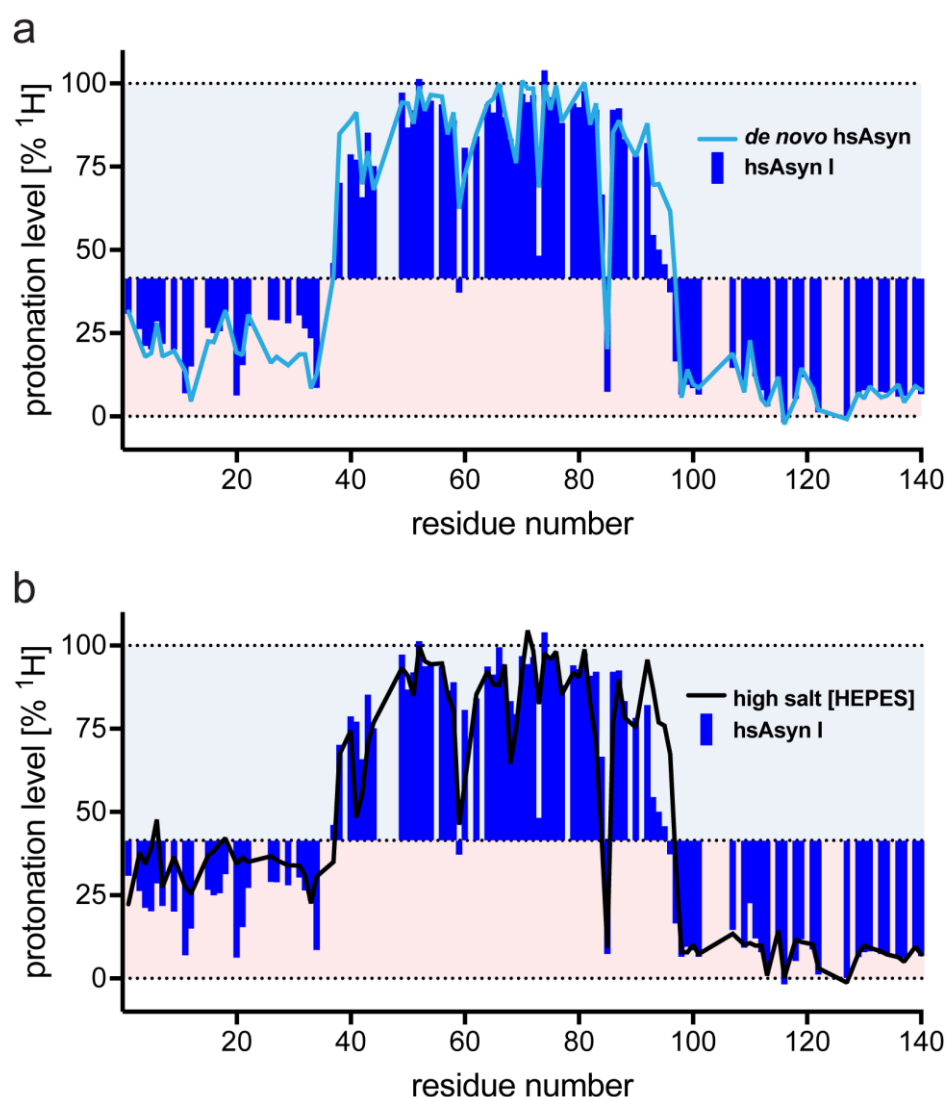
Figure 3-18. HD exchange profiles for *in vitro* high salt polymorph control experiments. (a) Comparison of HD exchange profiles of *de novo* aggregated hsAsyn I fibrils (line) and hsAsyn fibrils obtained after seeding (blue bars). (b) Comparison of the HD exchange profile of hsAsyn I fibrils (blue bars; buffer: 50 mM Tris-HCl, 150 mM KCl, pH 7.5, 0.02% NaN$_3$) with the HD exchange profile of aSyn fibrils obtained by aggregation in the aggregation buffer of brain-extract seeded aSyn fibrils (black line; buffer: 50 mM HEPES, 100 mM NaCl, pH 7.4, 0.02% NaN$_3$).

3.7.3   HD exchange profile of the *in vitro* low salt polymorph

Next, the HD exchange profile of the low salt *in vitro* polymorph (lsAsyn) was determined (Figure 3-19 a,b).
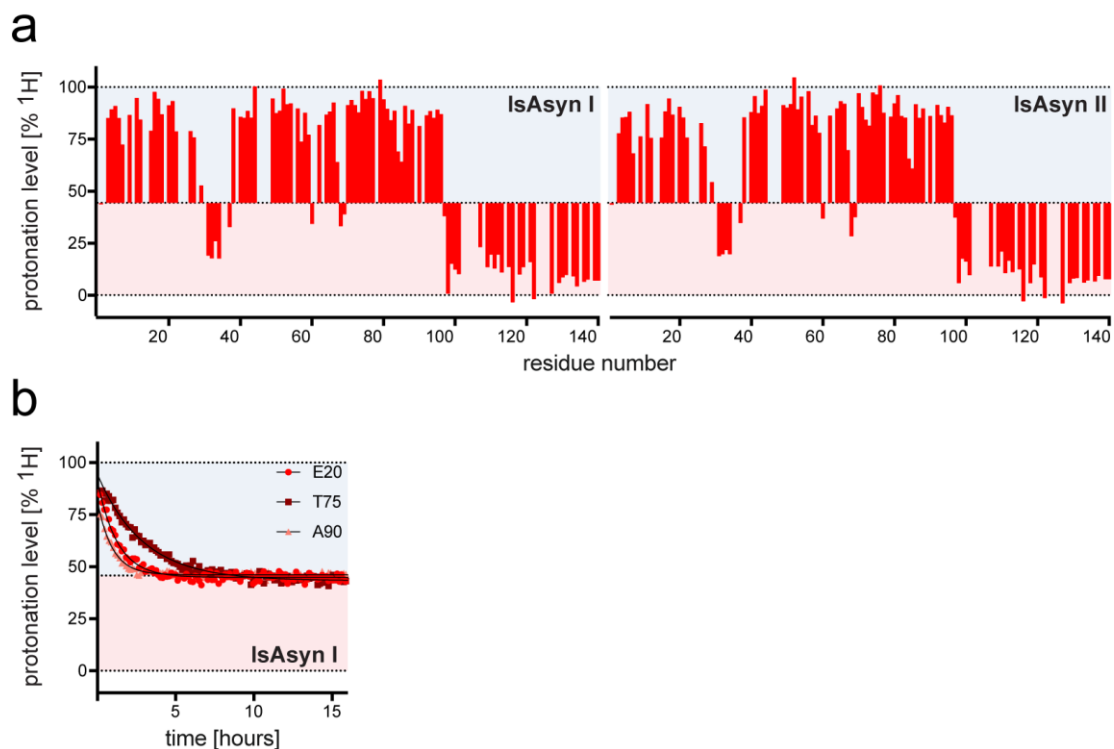
Figure 3-19. Residue-specific protonation levels in low salt polymorph (lsAsyn) fibrils by HD exchange.

(a) HD-exchange profiles of two independently seeded lsAsyn fibrils using the same *de novo* aggregates as seeds, labeled as lsAsyn I and II. (b) Time-dependent back-exchange of selected residues (E20, T75 and A90) for lsAsyn I fibrils.

In agreement with solid-state NMR spectroscopy[122], the lsAsyn polymorph contains hydrogen-bonded structure in the ~30 N-terminal residues (Figure 3-19 a, red).

3.7.4   Comparison of high- and low salt *in vitro* polymorphs

Comparing the two HD exchange profiles to each other, differences in protonation levels in the central part were evident in the two *in vitro* polymorphs, Figure 3-20. In the lsAsyn polymorph, solvent exchange for residues V37-T44 and G93-K97 was decreased when compared to hsAsyn. The turn residues T59, K60, G68, A69, G73 and A85 also differed in the protonation levels.

a

b
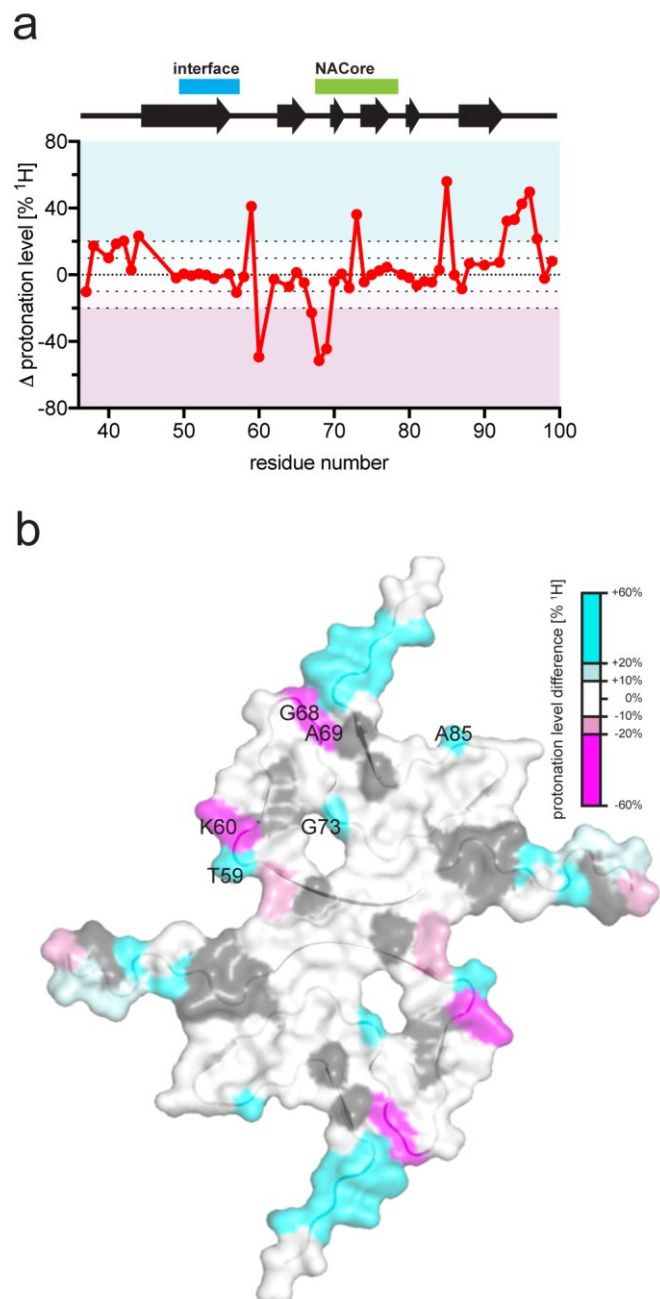
Figure 3-20. Comparison of HD exchange profile of high and low salt *in vitro* polymorphs. (a) Residue-specific differences in the protonation levels of hsAsyn and lsAsyn in the region from V37 to Q99, mapped in (b) onto the core structure of hsAsyn fibrils (PDB code: 6A6B). Difference values were calculated on the basis of the average protonation levels observed for two independently seeded samples (hsAsyn I/II and lsAsyn I/II respectively, see Figure 3-16 a and Figure 3-19 a). NaCore and the interface of the aSyn filaments are marked.

Thus, changes in amyloid structure occur when aSyn is aggregated at a low ionic strength matching Bousset et al.'s observations[122].

3.8   HD exchange profile of brain-extract seeded aSyn

HD exchange profiles of fibrils amplified from three different PD patients were very similar (Figure 3-21 b, Figure 3-23 b). For residues A53-K80, PD-protonation levels were also similar to those in hsAsyn fibrils (Figure 3-16 a,c). In contrast, protonation levels of residues L38-T44 were lower in the amyloid fibrils amplified from PD patient brain extracts when compared to the protonation levels in the *in vitro* polymorphs (Figure 3-22 a). In addition, the protonation levels decreased significantly from E83, suggesting a loss of hydrogen bonds (or decrease in hydrogen bond strength) for E83-K96 in PD-derived fibrils (Figure 3-22 a,b). Thus, amyloid fibrils that were amplified from PD patient brain extracts have a smaller hydrogen-bonded core than the two *in vitro* polymorphs hsAsyn and lsAsyn (Figure 3-22 a,b). This smaller core contains the most hydrophobic part of the aSyn sequence, the NACore region (G68-A78) which can form amyloid fibrils in isolation[175]. HD exchange profiles of aSyn fibrils amplified from brain extracts of three different PD patients were highly consistent (Figure 3-23 b). Two HD exchange profiles of aSyn fibrils amplified from brain extracts of individuals pathologically confirmed with MSA were also very similar to each other (purple bars in Figure 3-21 b), differences between MSA1 and hsAsyn I are shown for a selected region in the HSQC spectra (Figure 3-23 a). Disease-specific reproducibility was furthermore observed for the protonation levels of aSyn fibrils amplified from brain extracts of two DLB patients (orange bars in Figure 3-21 b). In addition, HD exchange profiles, which were obtained independently through seeding with PMCA-amplified fibrils from the same DLB patient, overlapped closely (Figure 3-23 c).

Because of the high reproducibility of the HD exchange studies, HD exchange patterns between different synucleinopathies (PD, MSA, DLB) were compared. Residues A18 to G93 displayed protonation levels above 50% in MSA-amplified fibrils (Figure 3-21 b), with V37-T44 and A85-G93 exchanging less rapidly when compared to PD-amplified fibrils (Figure 3-22 c,d). For DLB-amplified aSyn fibrils, protonation levels for residues A18-V48 and E83-G93 were in between those of PD and MSA (Figure 3-21 b). DLB- and MSA-amplified fibrils, however, had comparable protonation levels for A53-A56 (Figure 3-21 b, Figure 3-22 a), which were by 5-15% lower than in PD-amplified fibrils (Figure 3-22 c,d). Because A53-A56 are located in the interface with a second filament in the hsAsyn structure (Figure 3-17 a, Figure 3-22 d)[134,135], the more rapid solvent exchange of A53-A56 in MSA- and DLB-amplified fibrils could be caused by differences in the quaternary structure of aSyn fibrils in MSA and DLB when compared to PD.
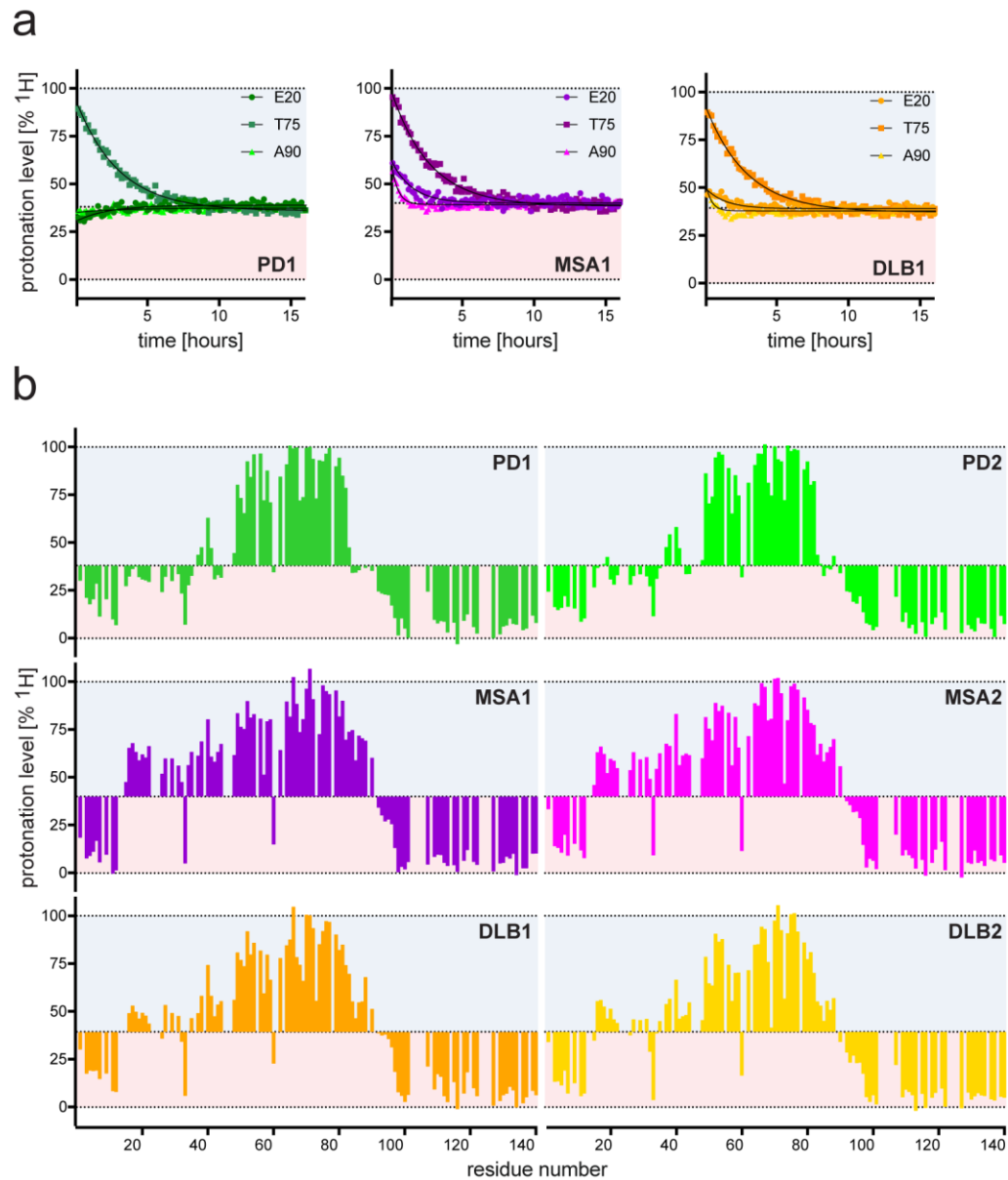
Figure 3-21. Residue-specific protonation levels of brain-extract seeded aSyn fibrils.

(a) Time-dependent back-exchange of patient-seeded aSyn fibrils of PD, MSA and DLB1 (E20, T75 and A90). (b) HD-exchange profiles of aSyn fibrils independently amplified from two individuals, which were pathologically confirmed with the same disease, are shown next to each other.
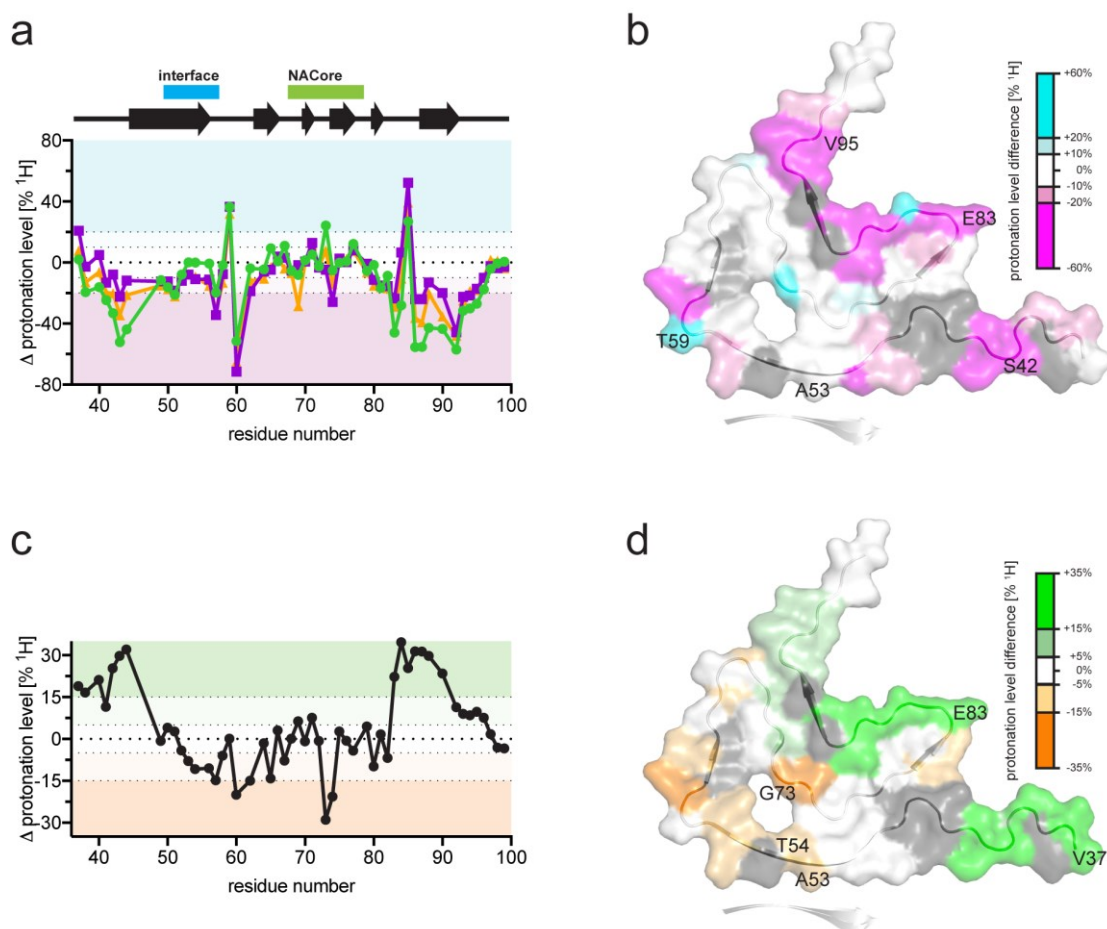
Figure 3-22. Conformational properties of aSyn fibrils amplified from PD, MSA and DLB brain extracts.

(a) Differences in the protonation levels in aSyn fibrils amplified from brain extracts (PD/green, MSA/purple, DLB/orange) when compared to those observed for the hsAsyn *in vitro* polymorph. Difference values were calculated on the basis of the average protonation levels observed for two patient samples each. The location of extended cross-β-structure within the hydrogen-bonded core of the hsAsyn fibril is shown on top. NACore is the most hydrophobic part of the aSyn sequence. (b) Mapping of protonation level differences between PD and hsAsyn (green curve in (a)) on the core structure of hsAsyn fibrils (PDB code: 6A6B). Differences are color coded according to the scale bar and as illustrated in (a). Residues that experience faster solvent exchange in PD fibrils are shown in magenta/pink, those with slower solvent exchange in cyan. Residues with signal overlap were excluded from the analysis (shown in grey). (c,d) Protonation level differences between aSyn fibrils amplified from PD- and MSA-brain extracts, mapped in (d) on the core structure of hsAsyn fibrils. Residues that experience faster solvent exchange in MSA fibrils (when compared to PD fibrils) are shown in orange, those with slower solvent exchange in green. Residues with signal overlap were excluded from the analysis (shown in grey in (d)).
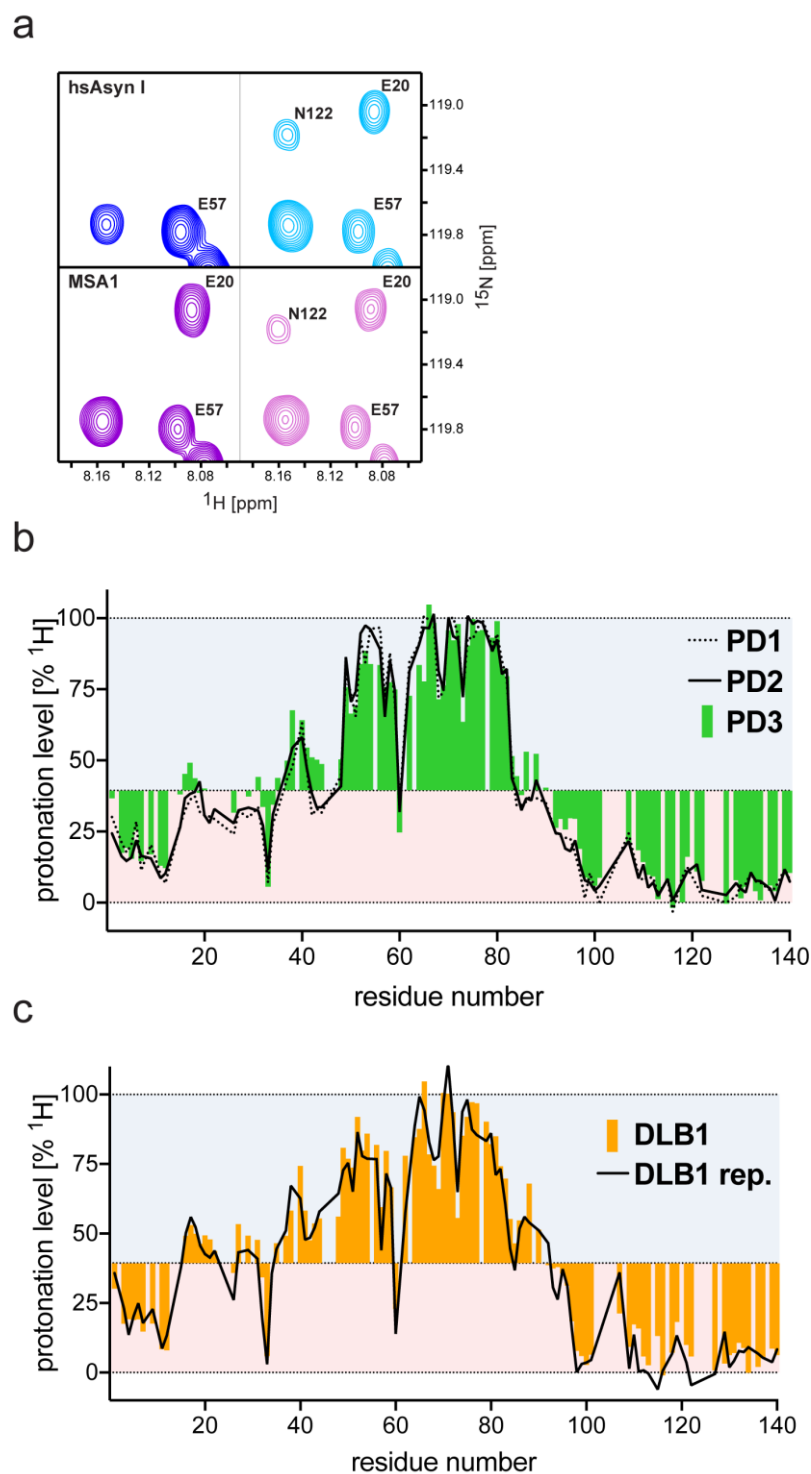
Figure 3-23. Extended data for brain-extract seeded fibrils.
(a) Selected region from ^{1}H-^{15}N correlation spectra recorded after fibril dissociation at the beginning (left) and end (right) of the back-exchange period for hsAsyn I fibrils in blue in comparison to MSA1 fibrils in purple. (b) Comparison of HD exchange profiles of aSyn fibrils amplified from the brain extracts of three different PD patients. HD exchange profiles of PD1 and PD2 are the same shown in Figure 3-21. (c) Comparison of HD exchange profiles of aSyn fibrils, which were obtained through seeding with PMCA-amplified fibrils from the same DLB patient.

3.9   EPR spectroscopy of aSyn fibrils

To further support structural differences between aSyn fibrils amplified from patient brain extracts and *in vitro* polymorphs, electron paramagnetic resonance (EPR) was used. In particular, to focus on the E83-G93 region (Figure 3-22 b). The recombinant aSyn-T54C/A90C mutant protein was labeled at the two cysteines with the nitroxide tag MTSL, and mixed with wild-type aSyn at a molar ratio of 1:30 (aSyn-T54C/A90C:aSyn)[165]. This mixture was subsequently aggregated into amyloid fibrils through seeding with either *in vitro* aSyn polymorphs or brain extract-amplified fibrils.

Continuous wave EPR spectra of all samples (hsAsyn, lsAsyn, PD, MSA, DLB) showed broad EPR lines (Figure 3-24 a,b), demonstrating that the MTSL-labeled aSyn-T54C/A90C protein was incorporated into fibrils[176].

sample	ratio fast/slow
hsAsyn	0.01
lsAsyn	0.01
PD1	0.06
PD2	0.06
MSA1	0.07
MSA2	0.06
DLB1	0.11
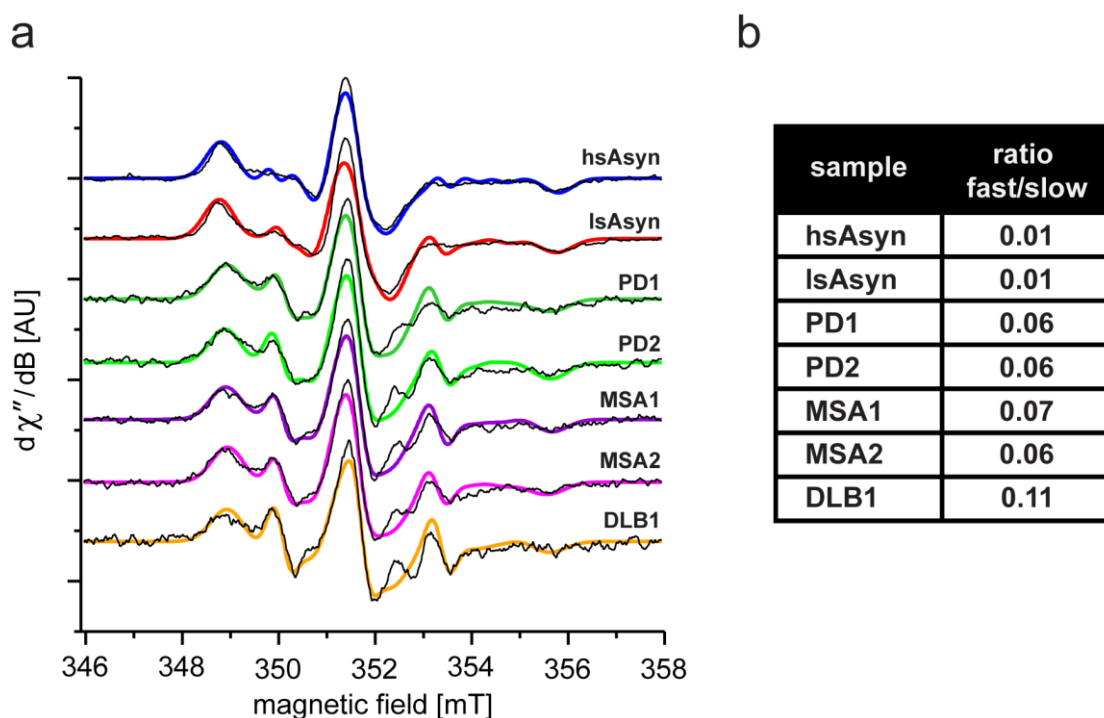
Figure 3-24. Continuous wave EPR spectra of aSyn fibrils.

(a) Continuous wave EPR spectra of aSyn fibrils. Fits derived from a two-spin simulation are shown as colored lines. (b) Dynamic parameters (weight: fast/slow) of MTSL spins derived from fitting continuous wave EPR spectra shown in (a). For both spin species g ≈ [2.008, 2.006, 2.002] and A/h ≈ [17.8-19, 18.5-19, 93-110] MHz. The peak-to-peak isotropic linewidths (lwpp) for the two species were $lwpp_{(slow)}$=0.52-0.67 mT and $lwpp_{(fast)}$=0.3-0.4 mT, respectively.
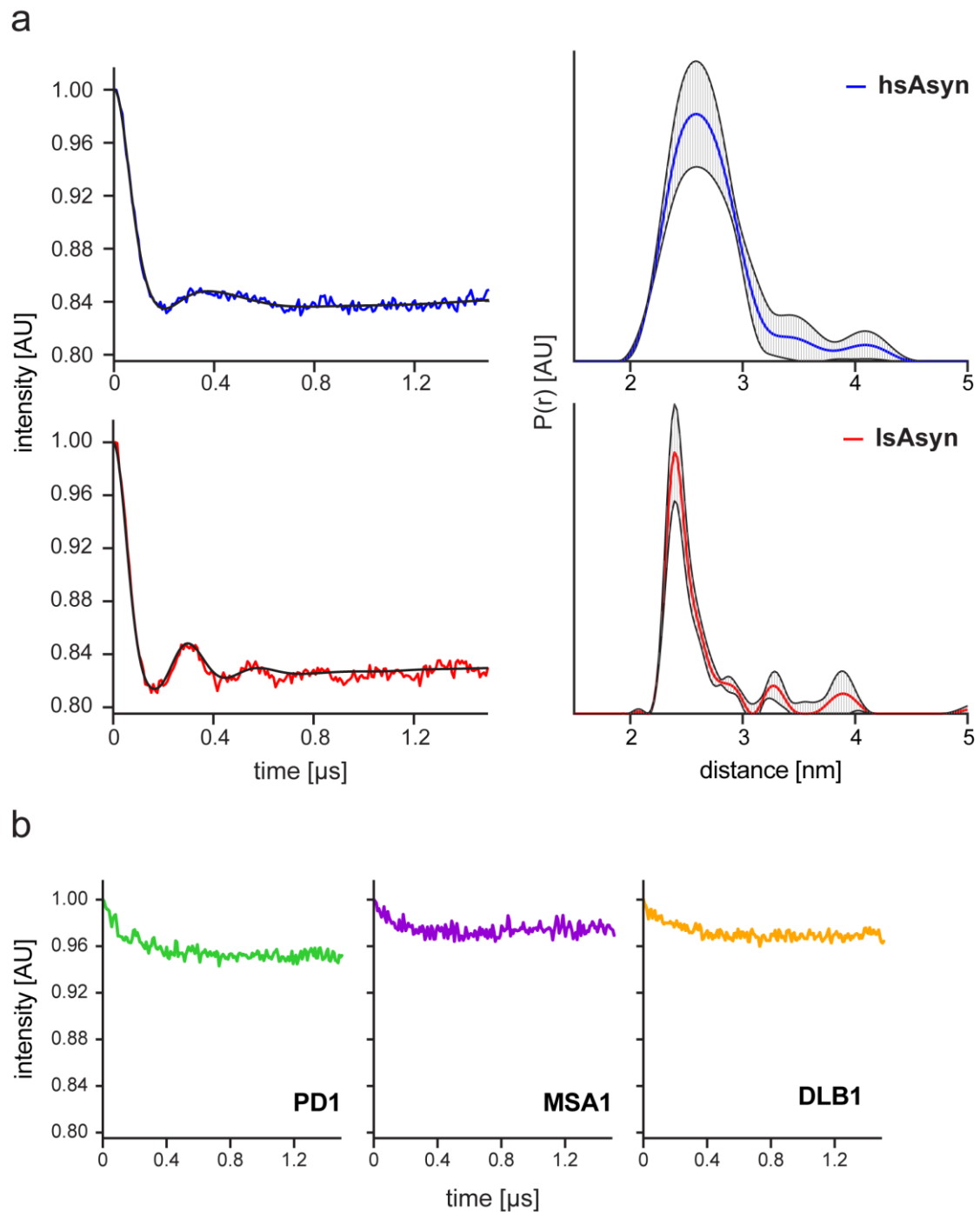
Figure 3-25. Dipolar modulation of aSyn fibrils.

(a) Dipolar modulation (a; corrected for background; fit in blue/red) and normalized distance distribution determined by 34 GHz four-pulse PELDOR experiments for hsAsyn (top, blue) and lsAsyn (bottom, red). (b) Background-corrected PELDOR traces of aSyn fibrils amplified from PD, MSA and DLB brain extracts. Electron micrographs of the aSyn fibrils are shown in Figure 3-5.

Results

Pulsed EPR distance measurements determined the distance between the two MTSL-labels at position 54 and 90 of the hsAsyn polymorph to be ~2.4-2.6 nm (Figure 3-25 a), in agreement with the structure of hsAsyn (Figure 2-8 b) and previous EPR data[165]. A similar yet slightly shorter distance was determined for lsAsyn (Figure 3-25 a). In contrast, no pronounced dipolar modulation was observed for any of the aSyn fibrils amplified from the brain extracts (Figure 3-25 b and Figure 3-26), despite the identical experimental parameters and comparable signal-to-noise ratios (Figure 3-26). The lack of dipolar modulations for the T54C/A90C-interaction in aSyn fibrils amplified from brain extracts suggests that these two residues do not have a single, defined distance in these fibrils (Figure 3-5). This could be caused by a number of reasons (alone or combined), including higher flexibility of the MTSL side chains, increased flexibility of the backbone, and larger heterogeneity/polymorphism in aSyn fibril conformations in these samples. Consistent with increased backbone flexibility/polymorphism, protonation levels of A85-G93 were lower in aSyn fibrils amplified from brain extracts when compared to the two *in vitro* polymorphs (Figure 3-22 a,b). In addition, estimation of MTSL mobility on the basis of continuous wave EPR spectra suggested that at least one of the two MTSL labels was more flexible in aSyn fibrils amplified from brain extract when compared to aSyn *in vitro* polymorphs (Figure 3-24 a,b). Because HD-exchange studies showed that the cross-β-structure of residues A85-G93 is destabilized in fibrils amplified from patient brain extracts (Figure 3-21 b, Figure 3-24 a), the MTSL with higher flexibility could be located at position 90.
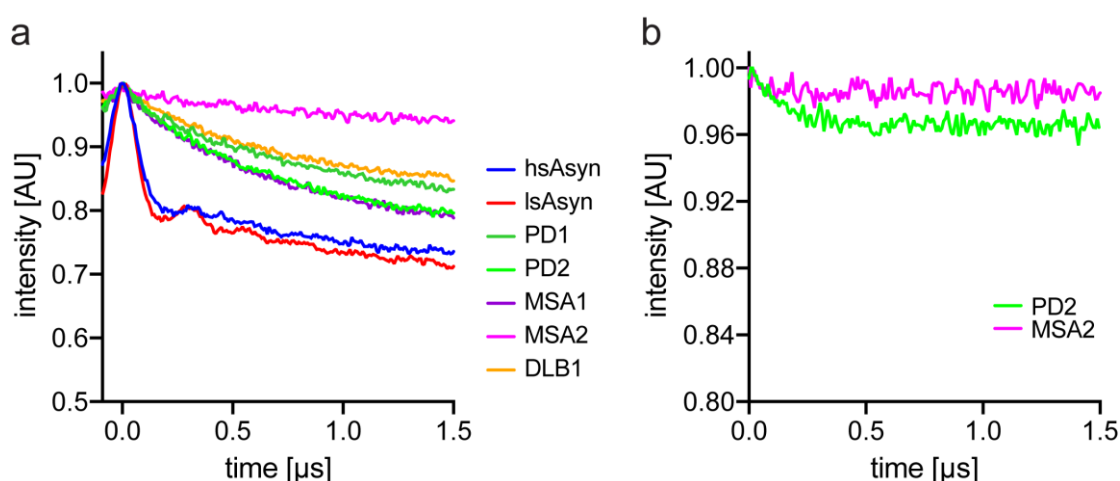
Figure 3-26. Dipolar modulation of aSyn fibrils, extended information.

(a) 34 GHz four-pulse PELDOR traces (without background correction) of different aSyn fibrils. (b) Background-corrected PELDOR traces of aSyn fibrils amplified from PD2 and MSA2 brain extracts.

4   Discussion

4.1   Evaluation HD exchange coupled to NMR spectroscopy

HD exchange coupled to NMR spectroscopy previously identified distinct cross-β-sheet cores in two prion strains[177]. A strength of the HD exchange method is that all molecules contribute to the NMR-observed protonation levels, which therefore characterize the full spectrum of fibril conformations present in each sample. This is important, because aSyn fibrils purified from patient brains are often polymorphic[4,54].

4.1.1   Accessibility of structural polymorphism by HD exchange
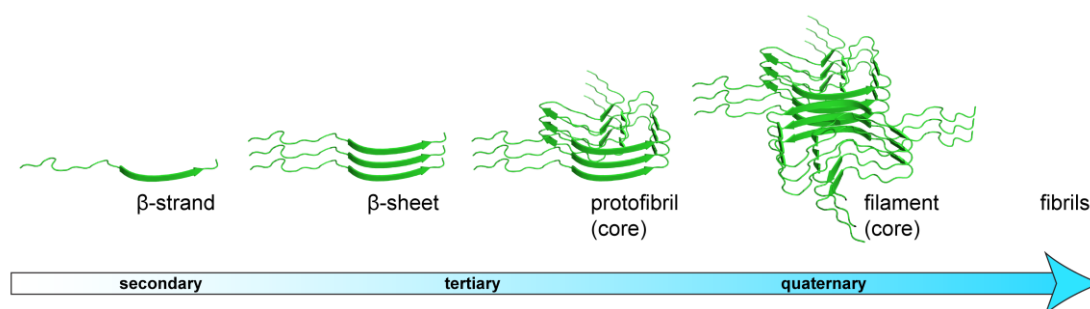
Figure 4-1 Structural complexity of aSyn fibrils.
High salt synuclein cryo-EM structure was used (PDB code: 6A6B). Increase in structural complexity from left to right indicated by arrow. The terms "secondary", "tertiary" and "quaternary" do not strictly follow the conventions of globular proteins, see Fitzpatrick et al.[178].

All levels of the structural complexity of aSyn fibrils (Figure 4-1) potentially influence hydrogen-bonding networks and solvent accessibility of the amide backbone. In-register intermolecular β-sheets strongly protect amide protons from hydrogen-deuterium forward exchange, as well as the tertiary architecture of the aSyn monomer perpendicular to the fibril axis. Quaternary effects such as protofibril interfaces may also influence hydrogen-deuterium forward exchange. HD exchange coupled to NMR spectroscopy also provides information about more flexible regions in amyloid fibrils. In contrast, aSyn fibril structures obtained by cryo-electron microscopy[134,135] are limited to the highly ordered fibrillar core region, e.g. residues V37-Q99 (PDB code: 6A6B) and L38-V95 (PDB code: 6H6B) respectively.

As shown in Figure 3-21 b, aSyn fibrils seeded by brain extract of MSA showed consistently higher protonation levels within residues A18-V48 than fibrils obtained from PD patients, with DLB aSyn fibrils lying in between. Taking into consideration a much stronger effect for the protonation level of the ~30 residue N-terminus of lsAsyn

Discussion

in vitro fibrils (Figure 3-19 a) with respect to the hsAsyn polymorph, aSyn fibril polymorphism among brain extract seeded aSyn fibrils may be due to extension of the central fibrillar core region. Specially for MSA brain extract-seeded fibrils it is not clear, if the higher protonation level from A18-V48 reflect a pure fibril conformation or the effect is due to a superimposition of aSyn fibrils showing high protonation levels and aSyn fibrils of lower protonation levels within the same region.

HD exchange coupled to NMR spectroscopy is an orthogonal method to high-resolution cryo-electron microscopy as shown for the mapping of hsAsyn fibril protonation levels to the fibrillar core of the cryo-EM structure of hsAsyn fibrils (Figure 3-17 a). However, in the absence of high molecular cryo-EM structures for aSyn fibrils seeded by brain-extracts, the interpretation of the observed protonation levels on the tertiary and quaternary structural level remains partially speculative. Nevertheless, the mapping of the protonation level differences to the hsAsyn polymorph for aSyn fibrils seeded by PD patients' brain, clearly identified sequential patches within the protofibril core that differ, hinting at conformational differences in particular for residues A85-G93 (Figure 3-22 a,b). In addition, changes in the protonation levels for residues A53-A56 in case of MSA- and DLB-seeded aSyn fibrils might reflect changes in quaternary structure (Figure 3-22 c,d).

4.1.2 Protonation levels in aSyn fibrils seeded by brain extracts

Li et al.[173] have recently solved the cryo-EM structure of two main conformations for the aggregation product of *in vitro* aggregated full-length aSyn fibrils, the "rod" and "twister" polymorph. They suggested a model (Figure 4-2) where the protofibril interface determines the fibrillar core structure. This model would explain why aSyn fibrils seeded from brain extract of MSA – and to a smaller extent also DLB-seeded aSyn fibrils – differ from aSyn fibrils of PD patients in the interface as well as the protonation level within the C-terminus of the fibrillar core.

As noted for aSyn fibrils seeded by brain extracts of MSA, an additional level of structural variability/heterogeneity occurs in regions proximal to the central core region. Proteinase-K digestion of aSyn fibrils purified from the brain of an individual pathologically confirmed with MSA resulted in three major bands migrating at 7, 8 and 9 kDa with the 7 and 8 kDa bands starting at G31[179]. The N-terminus of the 9 kDa band was mapped to A19/E20[179], in agreement with the finding that the protonation levels of residues A19-A29 exceed 50% in aSyn fibrils amplified from MSA brain extracts (Figure 3-21 b).
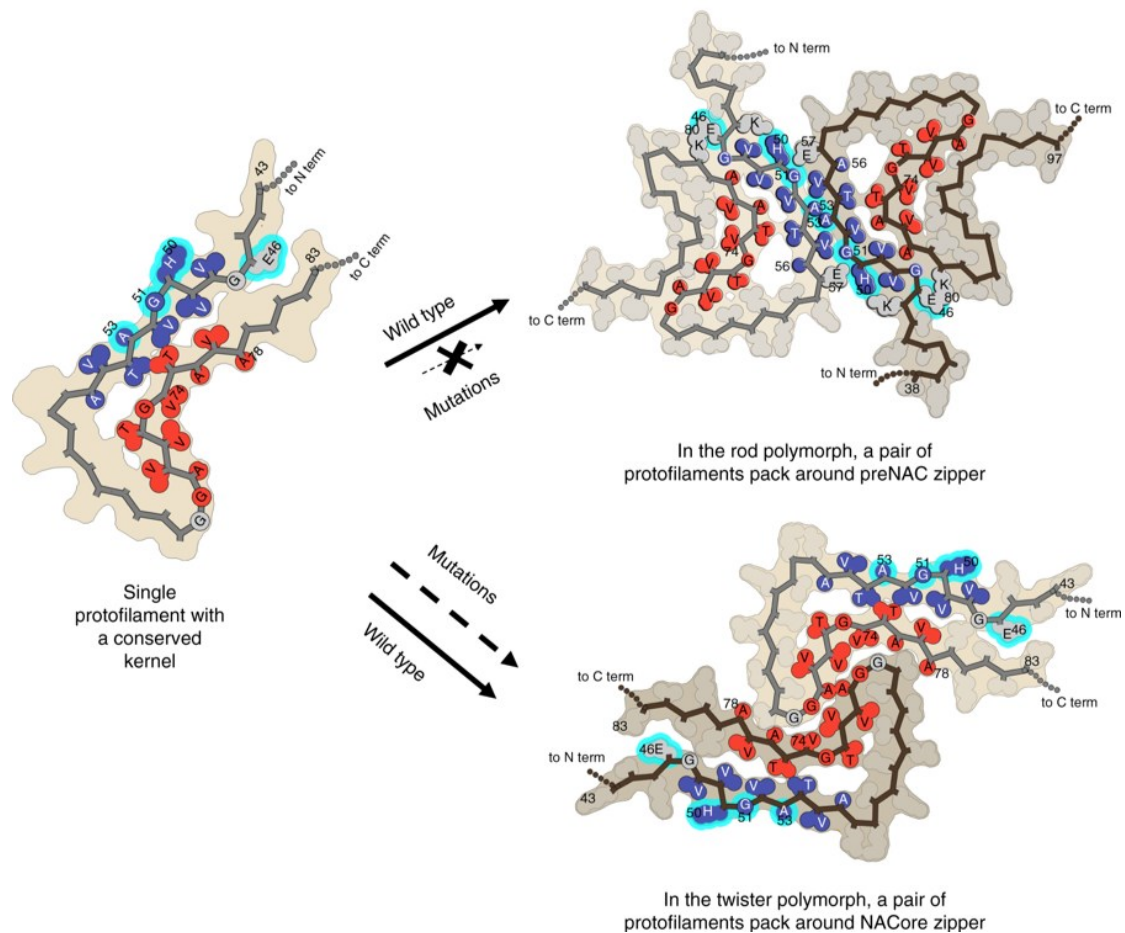
Figure 4-2. Different packing arrangements of the same protofilament kernel lead to polymorphic structures.

Model suggesting that protofilaments sharing a generic β-arch conformation (left) can assemble into aSyn filaments of different polymorphic structures, by forming distinct protofilament interfaces. The *rod* fibril polymorph forms the protofilament interface via the preNAC sequence (upper right), the *twister* fibril polymorph through the NACcore region (bottom right). The figure was taken from Li et al.[173].

4.1.3   Analysis of a broad range of aSyn fibrils

The comparison of aSyn fibrils seeded by brain extract of several patients from three different synucleinopathies (PD, MSA and DLB) in combination with the characterization of two *in vitro* polymorphs, hsAsyn and lsAsyn, presented a major challenge. Including the control experiments a high number of aSyn fibrils had to be structurally characterized. I therefore chose a unique approach of combining several techniques applied in the field for structural elucidation of amyloid fibrils.

The chosen strategy centered on the residue-specific determination of protonation levels by HD exchange coupled to NMR spectroscopy. A particular

strength of HD exchange coupled to NMR spectroscopy is the feasibility to study a larger number of fibrils in a justifiable amount of time. Transmission electron microscopy (TEM) was very helpful in addressing questions about the general morphology of the fibrils. The fibrillar core diameter observed by TEM already permitted important insights in quaternary structure of amyloid fibrils, reporting the number of protofibrils (~5 nm) the amplified fibrils contained. Circular dichroism allowed a qualitative read-out of the fibril aggregation assay, the formation of cross-β aggregates and the consumption of intrinsically disordered aSyn monomers.

With the fluorescence dyes, established molecular probes were used to look into the fine structure of aSyn fibrils. The combination of curcumin, FSB and HS-68 not only led to clear distinction of *in vitro* polymorphs from brain-extract seeded aSyn fibrils, it also hinted at more subtle differences among the different synucleinopathies (PD, MSA and DLB).

Electron paramagnetic resonance on MTSL-labeled aSyn mutant (aSyn T54C/A90C) incorporated into *in vitro* aSyn polymorphs yielded distance constraints for the tertiary protofibril architecture of aSyn. In addition, continuous wave (CW) EPR spectra provided information about the flexibility of the MTSL-labels and acted as atomic probes of the local environment of the MTSL-label within the aSyn fibrils. The absence of dipolar modulation of EPR was important for cross-validation of the HD exchange data. The broad EPR lines in CW spectra also directly reported on MTSL-labeled aSyn T54C/A90C mutant incorporation into fibrils, for both *in vitro* aSyn polymorphs as well as brain-extract seeded aSyn fibrils[165].

A structural characterization of the different amyloid fibrils by cryo-electron microscopy[134] or solid-state NMR spectroscopy[133,135] will be the target of future studies.

4.2 Amyloid polymorphism in other neurodegenerative diseases

4.2.1 Alzheimer's disease

In Alzheimer's disease (AD) two distinct morphologies of neurofibrillary tangles (NFTs) of tau are found in AD patients, paired helical filaments (PHFs) and straight filaments (SFs)[180]. Fitzpatrick et al.[181] solved the cryo-EM structure for the fibrillar core of the two tau polymorphs directly isolated from an AD patient's brain. The study showed that paired helical and straight filaments differ in their protofibril interface with the cores formed mainly by residues V306-F378 of R3 and R4 repeat of tau (Figure 4-3 a,b).
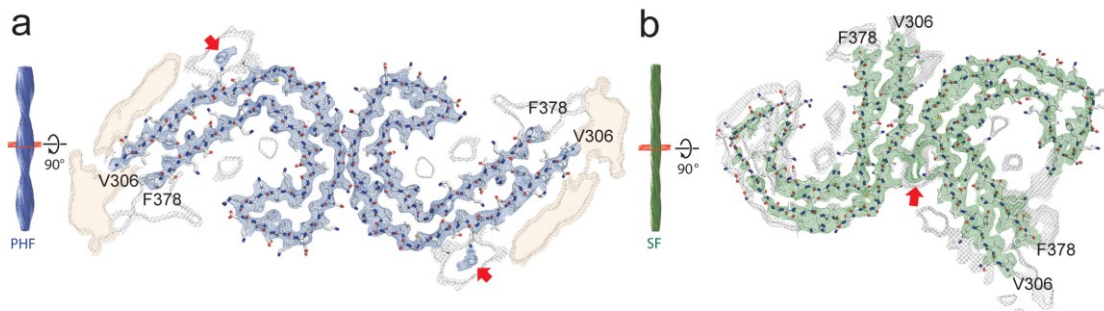
Figure 4-3. Cross-sections of the PHF and SF cryo-EM structures.
Atomic models of (a) PHF and (b) SFs overlaid with cryo-EM density. High resolution maps are shown in blue (PHFs) and green (SFs), additional high-resolution electron density that could not be assigned is indicated by red arrows. Lower resolution electron density is shown in grey, for PHF electron density in orange represents less ordered β-sheet accommodating 16 additional amino acids of potentially R1 and/or R2 tau repeats. Taken from Fitzpatrick et al.[181].

The work by Fitzpatrick et al. is currently the strongest evidence for structural polymorphs in tauopathies. A particular strength of this work is the structural elucidation of NTFs directly isolated from a single patient's brains, thus not requiring any amplification step. The scheme proposed by Li et al.[173] for two aSyn fibril *in vitro* polymorphs (Figure 4-2) that the protofibril interface determines the fibril packing and drives polymorphism seems to hold also true for NTFs of tau. Both types of tau NTFs, PHFs and SFs, occur in parallel within neuronal cells of a patient affected by AD. There is lack of information if upon propagation the structural information of PHFs and SFs is conserved. This would be required to support a true prion-like behavior[182]. In addition, Fitzpatrick et al.[181] conducted their research on a single AD patient, intersubject variability could therefore not be assed. Because more than 20 neurodegenerative disorders are linked to tau inclusions[183], structural tau polymorphism might be an underlying disease-defining phenomenon.

4.2.2 Tau inclusions in Pick's disease

Pick's disease (PiD) is associated with tau inclusions formed by the human 3R tau isoform lacking R2 repeat (Figure 4-4 a). Two polymorphs were observed in patients, the narrow pick filament (NPF) and wide pick filament (WPF). The wide pick filament consists of two NPFs, shown by Falcon et al.[184]. This is different from AD, where both SFs and PHFs consist of two protofibrils with distinct interfaces and packing (Figure 4-3).

Discussion

a

b
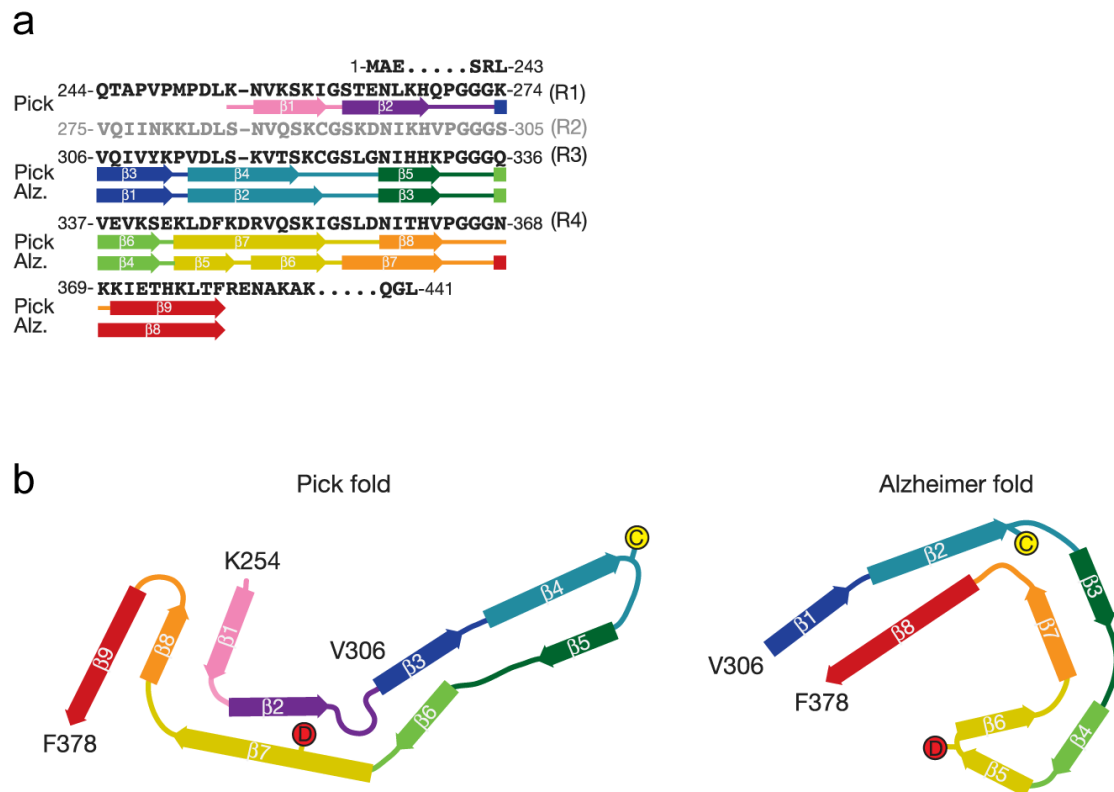
Figure 4-4. Polymorphic structure of tau inclusions in AD and PiD in comparison.

(a) Sequence alignment of the β-strands present in tau inclusions of Alzheimer's disease (Alz.) and Pick's disease (Pick). R2 repeat is missing in 3R tau isoform for PiD, numbering follows hTau40. (b) Pick fold of NPF on the left, protofibril of SFs and PHFs of AD on the right from Fitzpatrick et al.[181]. Figure was taken from Falcon et al.[184].

In addition to the quaternary differences, the tau protofibril fold in Pick's disease is distinct from Alzheimer's disease (Figure 4-4 b). Notable is the absence of a triangular arrangement of β-strands in the Pick fold formed by residues from K343 to I354, named β6 and β7 in the Pick fold (corresponding to β4-6 for the AD fold). The triangular arrangement is similar to β-helices, that were associated with amyloid fibrils of prion disease[185]. Another distinct feature of the Pick fold is the β-hairpin following C322 between β4 and β5, which is not observed for the Alzheimer fold. The interaction of β7 and β3 of R3 tau repeat in AD occurs in a similar way for β8 and β of R1 in Pick's disease.

The fibrillar core of the AD fold is comprised by R3 and R4, whereas R2 and R1 are part of the fuzzy coat. The Pick's fold, that is only associated with the 3R tau isoform shows a very distinct fold architecture in the absence of R2, most strikingly R1 is part of the fibrillar core, not observed in Alzheimer's disease. This led to the hypothesis, that tau might also be able to show disease-specific fibrillar core folds in

tau pathologies associated with the same 4R tau isoform composition as in AD[184] such as for example progressive supranuclear palsy.

4.2.3 Disease-associated amyloid polymorphism in tauopathies and synucleinopathies

The high resolution cryo-EM structures of ordered fibril cores in Alzheimer's disease (4R tau), both paired helical and straight filaments, and the fibrillar core fold of Pick's disease (3R tau) together show strong evidence for structural polymorphism in tauopathies. Polymorphism on the level of changes between the tertiary structure of the protofibril fold, AD fold versus Pick fold, as well as quaternary changes in the packing with different protofibril interfaces, as observed for PHFs vs SFs in Alzheimer's disease. To finally evaluate the disease-specific role of structural polymorphism in tauopathies, the same tau isoform (4R and/or 3R) has to be observed in different conformations for at least two distinct neurodegenerative diseases associated with tau aggregates.

The current state of the field does not sufficiently address the "fuzzy coat" of tau fibrils, comprising R1 entirely and most likely also parts of R2 for Alzheimer's disease and the N-terminus of R1 in Pick's disease. On top of that for PiD as well as AD, the core region of tau aggregates extends in the R' region of tau, extending beyond the R4 tau repeat (Figure 4-4 a).

In the current study on aSyn fibrils amplified from patient brain material, differences in the protonation levels were observed in a disease-specific manner for residues preceding the fibrillar core region, which was described by cryo-EM for *in vitro* aSyn fibrils. In case of aSyn fibrils amplified from brain material of a patient pathologically confirmed with MSA, residues A18 to V48 showed slower amide proton exchange when compared to DLB- and PD-seeded fibrils. The aSyn fibrils seeded by PD brain extract, vary also from MSA-seeded and to a lesser extent from DLB-seeded aSyn fibrils in the C-terminus of the core region from E83 to K96. Similar to tau aggregates, the aSyn fibril core-flanking regions and the absolute core extension itself might differ disease-specifically.

In the field of synucleinopathies, there are so far no high-resolution structures of fibrils isolated from patient brains available. In that sense, tau aggregates are much better characterized. This might have to do with the higher abundance of tau aggregates in the brain cortex compared to aSyn fibrils in synucleinopathies. On the other hand, the disease-specificity and strain-like behavior of aSyn pathology in disease progression models is better characterized in the α-synuclein field due to the

studies of Prusiner et al.[124], Bernis et al.[125] and Peng et al.[186]. In addition, direct spread of amyloid pathology from host-to-grafted tissue in patients, as shown for Lewy body pathology by Kordower et al.[114] and Li et al.[115], have so far not been reported for tauopathies.

The amplification of aSyn fibrils seeded by brain-extracts of patients, as achieved in the current work by PMCA, introduces an additional level of complexity when compared to amyloid fibrils purified from patient brain and characterized by cryo-EM. However, amplification of aSyn fibrils by PMCA is connected to and the resulting structural polymorphism observed follows strictly the prion-like definition, implying that structural differences between amyloid fibrils must be maintained during seeded protein aggregation.

4.2.4   Structural characterization of Aβ aggregates from AD patient brain material

The amyloid precursor protein (APP) derived peptides amyloid-β 40 (Aβ40) and amyloid-β 42 (Aβ42) are the most common cleavage products obtained by enzymatic proteolytic cleavage of APP trough α-, β- and γ-secretases[187]. Both isoforms form extracellular amyloid plaques in Alzheimer's disease with Aβ42 being the most aggregation prone isoform *in vitro*[188].

For Aβ40, two distinct *in vitro* polymorphs[189,190,191] were observed by solid-state NMR spectroscopy under the same buffer condition, protein concentration, ionic strength, pH and temperature (Figure 4-5 b,c). The "striated ribbon" polymorph was obtained by either *de novo* aggregation of Aβ40 under gentle agitation or seeded amplification using aforementioned *de novo* aggregated Aβ40 fibrils as seeds[190]. In the absence of agitation under quiescent conditions, Aβ40 formed a second polymorph that could also be amplified by seeded aggregation called "twisted ribbon", reflecting the twisted morphology in negative-stain transmission electron microscopy. Paravastu et al.[191] stated, that with this approach a polymorph homogeneity of *in vitro* Aβ fibrils higher than 90% was achieved for both polymorphs. The two polymorphs differ in their quaternary protofibril interfaces and the overall symmetry, the "striated ribbon" is formed by two Aβ40 units (Figure 4-5 b), the "twisted ribbon" shows a threefold symmetry formed by three Aβ40 units (Figure 4-5 c). The tertiary structure is highly conserved and both *in vitro* polymorphs show parallel in-register β-sheets. Both structural models start at residue G9, suggesting a flexible N-terminus. In addition to the "striated" and "twisted" *in vitro* polymorph of Aβ40, there exists another low resolution *in vitro* polymorph cryo-EM model for *de novo* aggregated Aβ40 fibrils

determined by Sachse et al.[192], comprised of two protofibrils with yet another suggested protofibril interface distinct from the "striated" and "twisted" polymorph. For the two *in vitro* polymorphs of Aβ40, variations in toxicity were observed in cell culture of primary neurons[189] which might indicate a potential prion-like behavior.
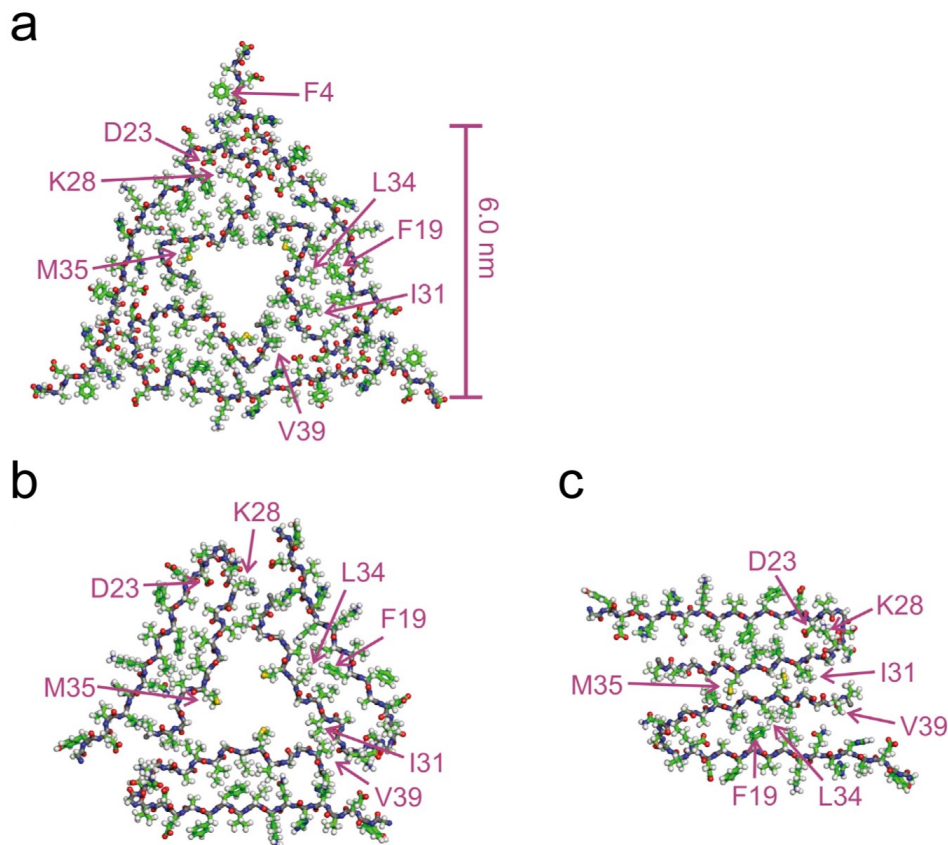
Figure 4-5. Aβ40 solid-state NMR structures.

(a) Aβ40 seeded by AD patient material (patient I). (b) *In vitro* aggregated Aβ40 fibrils, "twisted ribbon polymorph". (c) "Striated ribbon" polymorph obtained through *in vitro* aggregated of Aβ40. Figure taken from Lu et al.[193].

Aβ40 fibrils seeded by an aggregate-enriched fraction of brain extract from two AD patients were characterized and for a single patient (patient I) a high-resolution solid-state NMR structure was obtained (Figure 4-5 a)[193]. Upon seeding of Aβ40 with AD patient-derived material, Aβ40 fibrils of high homogeneity were obtained. The Aβ40 fibril seeded by aggregate-enriched brain fractions of patient I showed threefold symmetry similar to the "twisted ribbon" *in vitro* Aβ40 polymorph, but differs from both *in vitro* polymorphs, twisted and striated ribbon, in the protofibril tertiary fold. In contrast to the *in vitro* polymorphs, the N-terminus formed part of the cross-β fibrillar core of brain-extract amplified Aβ40 fibrils. Notably, no high-resolution model was determined

Discussion

for the second patient-derived Aβ40 fibrils, which were suggested to differ from those of patient I.

In case of Aβ42, high-resolution structures of amyloid fibrils, which were *in vitro* aggregated in different conditions, were determined. Two earlier studies reported different structural models, one obtained by cryo-EM for *de novo* aggregated *in vitro* fibrils at 5 Å resolution[194], the other one derived by solid-state NMR spectroscopy[195]. The cryo-EM model of the *in vitro* aggregated Aβ42 fibrils showed two-fold symmetry and consisted of two protofibrils reminiscent of the cryo-EM structure of Aβ40 *in vitro* fibrils[192]. The solid-state NMR structure of Aβ42 fibrils was obtained by a sequential repetitive seeding approach to amplify the dominant fibril polymorph. The structure revealed a single protofibril formed by three β-strands forming a "triple β-motif" starting at E11. Two independent research groups subsequently published highly similar refined structural models of *in vitro* Aβ42 fibrils also obtained by solid-state NMR spectroscopy[196,197] that confirmed the protofibril fold first described by Xiao et al.[195]. Differences in the tertiary protofibril fold between Xiao et al.'s model and the two more recent studies[196,197] are due to the newer studies being more refined with a higher number of intramolecular restraints. Wälti et al.[196] and Colvin et al.[197] independently suggested an identical protofibril interface for Aβ42 *in vitro* fibrils with two-fold symmetry. The intermolecular protofibril contacts are based on a number of intermolecular restraints. The hydrophobic residues L34, M35 and V36 form intermolecular contacts with V18, L17, K16 and Q15 and define the protofibril interface. For both dimeric solid-state structures, the N-terminus is highly flexible and not involved in cross-β fibril core. In a cryo-electron study of Aβ42 fibrils obtained by *in vitro* aggregation under quiescent conditions, a different fibril quaternary architecture was found[198]. The protofibril interface was also formed by a dimer, however the intermolecular contacts are mainly due to interactions of the C-terminus with the C-terminus of the adjacent protofibril, showing a unique quaternary fibril architecture. Strong differences were also observed on the tertiary level of the Aβ42 protofibril fold. Though the cryo-EM structure by Gremer et al.[198] is in agreement with the C-terminus of the solid-state NMR structures from residue S26 to A42, the N-terminus in contrast strongly deviates and forms part of the protofibril core.

Qiang et al.[199] compared Aβ40 fibrils obtained by seeding with patient material of AD patients diagnosed with distinct clinical disease subtypes and suggested the presence of a single dominant Aβ40 fibril structure. This however might be due to the chosen amplification protocol and does not rule out the existence of distinct disease-relevant polymorphs *in vivo*. In addition, Qiang et al.[199] seeded Aβ42 peptides by brain

material from patients diagnosed with clinical subtypes of AD and identified two distinct fibril conformations using 2D solid-state NMR.

The currently available structures for Aβ40 and Aβ42 support the importance of structural polymorphism. The solid-state NMR structures of Aβ40 (Figure 4-5) are consistent and follow the observations for aSyn and tau, that the flanking regions of the fibrillar core are a source of polymorphism and that polymorphism occurs in the packing with distinct protofibril interfaces and quaternary cross-β folds.

5   Conclusions and perspectives

This study establishes a strong correlation between aSyn structure and disease phenotype. The disease-specific polymorphs characterized in this study are distinct from *in vitro* amplified aSyn fibrils obtained by seeded aggregation under high and low salt conditions, shown in detail by HD exchange coupled to NMR spectroscopy, EPR spectroscopy and fluorescent dye binding. The data suggest, that the high-resolution structures of *in vitro* aSyn fibrils available in the field of synucleinopathies may not fully reflect structural features of disease-relevant polymorphs and differences on the quaternary and tertiary structural level are likely.

Even more importantly, the patient's disease classification - Parkinson's disease (PD), multiple system atrophy (MSA) or dementia with Lewy body (DLB) - is reflected in the polymorphic structure of aSyn fibrils seeded by brain extracts of the individual patients (Table 3) shown by hydrogen-deuterium (HD) exchange coupled to NMR spectroscopy. This observation proofs that the seeds present in brain extracts of patients not only catalyze the misfolding and aggregation of recombinant aSyn monomer but imprint structural features by templated seeding in a prion-like manner. Disease-relevant prion-like behavior of aSyn strains was already observed earlier in glial cytoplasmatic inclusions (GCI) with respect to aSyn aggregates of Lewy body (LB) pathology[124,186]. This is the first study however, that shows structural polymorphism between distinct synucleinopathies on the level of residue-specific conformations of aSyn fibrils and simultaneously correlates the finding to available high-resolution structures and known structural features of genuine *in vitro* aSyn polymorphs in the field. Along the way, it was also confirmed that protein misfolding cyclic amplification[106] (PMCA) conserved key and disease-defining conformational properties of the initial patient-derived seeds characterized in this study at so far highest structural precision.

The implications of the data presented here are far-reaching. On one hand a further in-depth structural analysis of aSyn fibrils seeded by brain-extract of patients has to follow in subsequent studies to asses differences in the protofibril fold and quaternary aSyn structure, such as the fibrillar core symmetry and the exact protofibril interface. Cryo-electron microscopy as well as solid-state NMR spectroscopy are promising choices. On the other hand, it would be very interesting to know if the obtained disease-specific aSyn fibril polymorphs show also distinct toxicities in cell culture and animal models. This would be an important corner stone to shed further light on prion-like disease transmission and infectiousness of aSyn aggregates in synucleinopathies.

The approach might also be applicable to neurodegenerative diseases caused by other proteins that undergo misfolding and aggregation, such as e.g. tau and Aβ. Specially for tau the existence of *in vivo* tau polymorphs is very well established for Alzheimer's disease and Pick's disease, but the propagation of structural conformations through seeded aggregation has not been sufficiently shown yet.

The disease-specific structural conformations of aSyn fibrils seeded by brain-extracts of PD, MSA and DLB might open new targets for pharmaceutical research. This study is thus an important milestone in the understanding of aSyn pathology and contributes to the development of appropriate diagnostic and therapeutic agents in distinct synucleinopathies.

6 Bibliography

1   Abbott, A. Dementia: A problem for our age. *Nature* **475**, S2, (2011).

2   Sipe, J. D. & Cohen, A. S. Review: history of the amyloid fibril. *J Struct Biol* **130**, 88-98, (2000).

3   Parkinson, J. An essay on the shaking palsy. 1817. *J Neuropsychiatry Clin Neurosci* **14**, 223-236; discussion 222, (2002).

4   Spillantini, M. G., Crowther, R. A., Jakes, R., Hasegawa, M. & Goedert, M. alpha-Synuclein in filamentous inclusions of Lewy bodies from Parkinson's disease and dementia with lewy bodies. *Proc Natl Acad Sci U S A* **95**, 6469-6473, (1998).

5   Alzheimer, A., Stelzmann, R. A., Schnitzlein, H. N. & Murtagh, F. R. An English translation of Alzheimer's 1907 paper, "Uber eine eigenartige Erkankung der Hirnrinde". *Clin Anat* **8**, 429-431, (1995).

6   Hardy, J. & Allsop, D. Amyloid deposition as the central event in the aetiology of Alzheimer's disease. *Trends Pharmacol Sci* **12**, 383-388, (1991).

7   Morishima-Kawashima, M. *et al.* Hyperphosphorylation of tau in PHF. *Neurobiol Aging* **16**, 365-371; discussion 371-380, (1995).

8   Rowland, L. P. How amyotrophic lateral sclerosis got its name: The clinical-pathologic genius of jean-martin charcot. *Archives of Neurology* **58**, 512-515, (2001).

9   Hardiman, O. *et al.* Amyotrophic lateral sclerosis. *Nat Rev Dis Primers* **3**, 17071, (2017).

10   Rosen, D. R. *et al.* Mutations in Cu/Zn superoxide dismutase gene are associated with familial amyotrophic lateral sclerosis. *Nature* **362**, 59-62, (1993).

11   George Huntington. On Chorea. *The Journal of Neuropsychiatry and Clinical Neurosciences* **15**, 109-112, (2003).

12   MacDonald, M. E. *et al.* A novel gene containing a trinucleotide repeat that is expanded and unstable on Huntington's disease chromosomes. *Cell* **72**, 971-983, (1993).

13   Katscher, F. It's Jakob's disease, not Creutzfeldt's. *Nature* **393**, 11, (1998).

14   Prusiner, S. B. Novel proteinaceous infectious particles cause scrapie. *Science* **216**, 136-144, (1982).

15   Walker, L. C. Proteopathic Strains and the Heterogeneity of Neurodegenerative Diseases. *Annu Rev Genet* **50**, 329-346, (2016).

16   Wood, L. B., Winslow, A. R. & Strasser, S. D. Systems biology of neurodegenerative diseases. *Integr Biol (Camb)* **7**, 758-775, (2015).

17   Wu, Y. T. *et al.* Dementia in western Europe: epidemiological evidence and implications for policy making. *Lancet Neurol* **15**, 116-124, (2016).

18   Shibasaki, Y., Baillie, D. A., St Clair, D. & Brookes, A. J. High-resolution mapping of SNCA encoding alpha-synuclein, the non-A beta component of Alzheimer's disease amyloid precursor, to human chromosome 4q21.3-->q22 by fluorescence in situ hybridization. *Cytogenet Cell Genet* **71**, 54-55, (1995).

19   Maroteaux, L., Campanelli, J. T. & Scheller, R. H. Synuclein: a neuron-specific protein localized to the nucleus and presynaptic nerve terminal. *J Neurosci* **8**, 2804-2815, (1988).

20   Nakajo, S. *et al.* Purification and characterization of a novel brain-specific 14-kDa protein. *J Neurochem* **55**, 2031-2038, (1990).

21   Nakajo, S., Tsukada, K., Omata, K., Nakamura, Y. & Nakaya, K. A new brain-specific 14-kDa protein is a phosphoprotein. Its complete amino acid sequence and evidence for phosphorylation. *Eur J Biochem* **217**, 1057-1063, (1993).

22   Ueda, K. *et al.* Molecular cloning of cDNA encoding an unrecognized component of amyloid in Alzheimer disease. *Proc Natl Acad Sci U S A* **90**, 11282-11286, (1993).

23   Jakes, R., Spillantini, M. G. & Goedert, M. Identification of two distinct synucleins from human brain. *FEBS Lett* **345**, 27-32, (1994).

24   Ji, H. *et al.* Identification of a breast cancer-specific gene, BCSG1, by direct differential cDNA sequencing. *Cancer Res* **57**, 759-764, (1997).

25   Ohtake, H. *et al.* Beta-synuclein gene alterations in dementia with Lewy bodies. *Neurology* **63**, 805-811, (2004).

26   Fujita, M. *et al.* A beta-synuclein mutation linked to dementia produces neurodegeneration when expressed in mouse brain. *Nat Commun* **1**, 110, (2010).

27   Eliezer, D., Kutluay, E., Bussell, R., Jr. & Browne, G. Conformational properties of alpha-synuclein in its free and lipid-associated states. *J Mol Biol* **307**, 1061-1073, (2001).

28   Fauvet, B. *et al.* alpha-Synuclein in central nervous system and from erythrocytes, mammalian cells, and Escherichia coli exists predominantly as disordered monomer. *J Biol Chem* **287**, 15345-15364, (2012).

29   Theillet, F. X. *et al.* Structural disorder of monomeric alpha-synuclein persists in mammalian cells. *Nature* **530**, 45-50, (2016).

30   Bertoncini, C. W. *et al.* Release of long-range tertiary interactions potentiates aggregation of natively unstructured alpha-synuclein. *Proc Natl Acad Sci U S A* **102**, 1430-1435, (2005).

31   Allison, J. R., Varnai, P., Dobson, C. M. & Vendruscolo, M. Determination of the free energy landscape of alpha-synuclein using spin label nuclear magnetic resonance measurements. *J Am Chem Soc* **131**, 18314-18326, (2009).

32   Ulmer, T. S., Bax, A., Cole, N. B. & Nussbaum, R. L. Structure and dynamics of micelle-bound human alpha-synuclein. *J Biol Chem* **280**, 9595-9603, (2005).

33   Fusco, G. *et al.* Structural basis of synaptic vesicle assembly promoted by alpha-synuclein. *Nat Commun* **7**, 12563, (2016).

34   Dobson, C. M. Protein folding and misfolding. *Nature* **426**, 884-890, (2003).

35   Sunde, M. & Blake, C. The structure of amyloid fibrils by electron microscopy and X-ray diffraction. *Adv Protein Chem* **50**, 123-159, (1997).

36   Astbury, W. T., Dickinson, S. & Bailey, K. The X-ray interpretation of denaturation and the structure of the seed globulins. *Biochem J* **29**, 2351-2360 2351, (1935).

37   Bradbury, E. M. *et al.* The "Cross-β" structure in polypeptides of low molecular weight. *Journal of Molecular Biology* **2**, 276-IN271, (1960).

38   Hoyer, W. *et al.* Dependence of alpha-synuclein aggregate morphology on solution conditions. *J Mol Biol* **322**, 383-393, (2002).

39   Uversky, V. N. A protein-chameleon: conformational plasticity of alpha-synuclein, a disordered protein involved in neurodegenerative disorders. *J Biomol Struct Dyn* **21**, 211-234, (2003).

40   Fernandez, C. O. *et al.* NMR of alpha-synuclein-polyamine complexes elucidates the mechanism and kinetics of induced aggregation. *EMBO J* **23**, 2039-2046, (2004).

41   Kim, H. Y. *et al.* Structural properties of pore-forming oligomers of alpha-synuclein. *J Am Chem Soc* **131**, 17482-17489, (2009).

42   Henderson, M. X. *et al.* Unbiased Proteomics of Early Lewy Body Formation Model Implicates Active Microtubule Affinity-Regulating Kinases (MARKs) in Synucleinopathies. *J Neurosci* **37**, 5870-5884, (2017).

43   Cookson, M. R. alpha-Synuclein and neuronal cell death. *Mol Neurodegener* **4**, 9, (2009).

44   Bengoa-Vergniory, N., Roberts, R. F., Wade-Martins, R. & Alegre-Abarrategui, J. Alpha-synuclein oligomers: a new hope. *Acta Neuropathol* **134**, 819-838, (2017).

45   Cox, D., Carver, J. A. & Ecroyd, H. Preventing alpha-synuclein aggregation: the role of the small heat-shock molecular chaperone proteins. *Biochim Biophys Acta* **1842**, 1830-1843, (2014).

46   Lee, S. J., Jeon, H. & Kandror, K. V. Alpha-synuclein is localized in a subpopulation of rat brain synaptic vesicles. *Acta Neurobiol Exp (Wars)* **68**, 509-515, (2008).

47   Vargas, K. J. *et al.* Synucleins regulate the kinetics of synaptic vesicle endocytosis. *J Neurosci* **34**, 9364-9376, (2014).

48   George, J. M., Jin, H., Woods, W. S. & Clayton, D. F. Characterization of a novel protein regulated during the critical period for song learning in the zebra finch. *Neuron* **15**, 361-372, (1995).

49   Burre, J. *et al.* Alpha-synuclein promotes SNARE-complex assembly in vivo and in vitro. *Science* **329**, 1663-1667, (2010).

50   Burre, J., Sharma, M. & Sudhof, T. C. alpha-Synuclein assembles into higher-order multimers upon membrane binding to promote SNARE complex formation. *Proc Natl Acad Sci U S A* **111**, E4274-4283, (2014).

51   Spillantini, M. G. *et al.* Alpha-synuclein in Lewy bodies. *Nature* **388**, 839-840, (1997).

52   Biere, A. L. *et al.* Parkinson's disease-associated alpha-synuclein is more fibrillogenic than beta- and gamma-synuclein and cannot cross-seed its homologs. *J Biol Chem* **275**, 34574-34579, (2000).

53   Nakazato, Y., Yamazaki, H., Hirato, J., Ishida, Y. & Yamaguchi, H. Oligodendroglial microtubular tangles in olivopontocerebellar atrophy. *J Neuropathol Exp Neurol* **49**, 521-530, (1990).

54   Spillantini, M. G. *et al.* Filamentous alpha-synuclein inclusions link multiple system atrophy with Parkinson's disease and dementia with Lewy bodies. *Neurosci Lett* **251**, 205-208, (1998).

55   Tretiakoff, C. Contribution a l'etude de l'Anatomie pathologique du Locus Niger de Soemmering avec quelques deduction relatives a la pathogenie

des troubles du tonus musculaire et de la maladie de Parkinson. *Theses de Paris*, (1919).

56   Okazaki, H., Lipkin, L. E. & Aronson, S. M. Diffuse intracytoplasmic ganglionic inclusions (Lewy type) associated with progressive dementia and quadriparesis in flexion. *J Neuropathol Exp Neurol* **20**, 237-244, (1961).

57   Kalia, L. V. & Lang, A. E. Parkinson disease in 2015: Evolving basic, pathological and clinical concepts in PD. *Nat Rev Neurol* **12**, 65-66, (2016).

58   Alafuzoff, I. & Hartikainen, P. Alpha-synucleinopathies. *Handb Clin Neurol* **145**, 339-353, (2017).

59   McCann, H., Stevens, C. H., Cartwright, H. & Halliday, G. M. alpha-Synucleinopathy phenotypes. *Parkinsonism Relat Disord* **20 Suppl 1**, S62-67, (2014).

60   Anderson, J. P. *et al.* Phosphorylation of Ser-129 is the dominant pathological modification of alpha-synuclein in familial and sporadic Lewy body disease. *J Biol Chem* **281**, 29739-29752, (2006).

61   Hasegawa, M. *et al.* Phosphorylated alpha-synuclein is ubiquitinated in alpha-synucleinopathy lesions. *J Biol Chem* **277**, 49071-49076, (2002).

62   Wakabayashi, K. *et al.* The Lewy body in Parkinson's disease and related neurodegenerative disorders. *Mol Neurobiol* **47**, 495-508, (2013).

63   Xia, Q. *et al.* Proteomic identification of novel proteins associated with Lewy bodies. *Front Biosci* **13**, 3850-3856, (2008).

64   Hirtz, D. *et al.* How common are the "common" neurologic disorders? *Neurology* **68**, 326-337, (2007).

65   Wirdefeldt, K., Adami, H. O., Cole, P., Trichopoulos, D. & Mandel, J. Epidemiology and etiology of Parkinson's disease: a review of the evidence. *Eur J Epidemiol* **26 Suppl 1**, S1-58, (2011).

66   Dorsey, E. R. *et al.* Projected number of people with Parkinson disease in the most populous nations, 2005 through 2030. *Neurology* **68**, 384-386, (2007).

67   Gibb, W. R. & Lees, A. J. The relevance of the Lewy body to the pathogenesis of idiopathic Parkinson's disease. *J Neurol Neurosurg Psychiatry* **51**, 745-752, (1988).

68   Kruger, R. *et al.* Ala30Pro mutation in the gene encoding alpha-synuclein in Parkinson's disease. *Nat Genet* **18**, 106-108, (1998).

69   Zarranz, J. J. *et al.* The new mutation, E46K, of alpha-synuclein causes Parkinson and Lewy body dementia. *Ann Neurol* **55**, 164-173, (2004).

70   Appel-Cresswell, S. *et al.* Alpha-synuclein p.H50Q, a novel pathogenic mutation for Parkinson's disease. *Mov Disord* **28**, 811-813, (2013).

71   Kiely, A. P. *et al.* alpha-Synucleinopathy associated with G51D SNCA mutation: a link between Parkinson's disease and multiple system atrophy? *Acta Neuropathol* **125**, 753-769, (2013).

72   Polymeropoulos, M. H. *et al.* Mutation in the alpha-synuclein gene identified in families with Parkinson's disease. *Science* **276**, 2045-2047, (1997).

73   Proukakis, C. *et al.* A novel alpha-synuclein missense mutation in Parkinson disease. *Neurology* **80**, 1062-1064, (2013).

74   Chartier-Harlin, M. C. *et al.* Alpha-synuclein locus duplication as a cause of familial Parkinson's disease. *Lancet* **364**, 1167-1169, (2004).

75   Singleton, A. B. *et al.* alpha-Synuclein locus triplication causes Parkinson's disease. *Science* **302**, 841, (2003).

76   Connolly, B. S. & Lang, A. E. Pharmacological treatment of Parkinson disease: a review. *JAMA* **311**, 1670-1683, (2014).

77   Williams, A. *et al.* Deep brain stimulation plus best medical therapy versus best medical therapy alone for advanced Parkinson's disease (PD SURG trial): a randomised, open-label trial. *Lancet Neurol* **9**, 581-591, (2010).

78   Heidebrink, J. L. Is dementia with Lewy bodies the second most common cause of dementia? *J Geriatr Psychiatry Neurol* **15**, 182-187, (2002).

79   Gilman, S. *et al.* Second consensus statement on the diagnosis of multiple system atrophy. *Neurology* **71**, 670-676, (2008).

80   Asi, Y. T. *et al.* Alpha-synuclein mRNA expression in oligodendrocytes in MSA. *Glia* **62**, 964-970, (2014).

81   Peng, C., Gathagan, R. J. & Lee, V. M. Distinct alpha-Synuclein strains and implications for heterogeneity among alpha-Synucleinopathies. *Neurobiol Dis* **109**, 209-218, (2018).

82   Uchikado, H., Lin, W. L., DeLucia, M. W. & Dickson, D. W. Alzheimer disease with amygdala Lewy bodies: a distinct form of alpha-synucleinopathy. *J Neuropathol Exp Neurol* **65**, 685-697, (2006).

83   Hamilton, R. L. Lewy bodies in Alzheimer's disease: a neuropathological review of 145 cases using alpha-synuclein immunohistochemistry. *Brain Pathol* **10**, 378-384, (2000).

84   Liao, Y. C., Lebo, R. V., Clawson, G. A. & Smuckler, E. A. Human prion protein cDNA: molecular cloning, chromosomal mapping, and biological implications. *Science* **233**, 364-367, (1986).

85   Schmitt-Ulms, G., Ehsani, S., Watts, J. C., Westaway, D. & Wille, H. Evolutionary descent of prion genes from the ZIP family of metal ion transporters. *PLoS One* **4**, e7208, (2009).

86   Riek, R. *et al.* NMR structure of the mouse prion protein domain PrP(121-231). *Nature* **382**, 180-182, (1996).

87   Haire, L. F. *et al.* The crystal structure of the globular domain of sheep prion protein. *J Mol Biol* **336**, 1175-1183, (2004).

88   Smirnovas, V. *et al.* Structural organization of brain-derived mammalian prions examined by hydrogen-deuterium exchange. *Nat Struct Mol Biol* **18**, 504-506, (2011).

89   Gambetti, P., Kong, Q., Zou, W., Parchi, P. & Chen, S. G. Sporadic and familial CJD: classification and characterisation. *Br Med Bull* **66**, 213-239, (2003).

90   Goldfarb, L. G., Korczyn, A. D., Brown, P., Chapman, J. & Gajdusek, D. C. Mutation in codon 200 of scrapie amyloid precursor gene linked to Creutzfeldt-Jakob disease in Sephardic Jews of Libyan and non-Libyan origin. *Lancet* **336**, 637-638, (1990).

91   George, S. & Brundin, P. Solving the conundrum of insoluble protein aggregates. *Lancet Neurol* **16**, 258-259, (2017).

92   Powell-Jackson, J. *et al.* Creutzfeldt-Jakob disease after administration of human growth hormone. *Lancet* **2**, 244-246, (1985).

93   Hill, A. F. *et al.* The same prion strain causes vCJD and BSE. *Nature* **389**, 448-450, 526, (1997).

94   Urwin, P. J., Mackenzie, J. M., Llewelyn, C. A., Will, R. G. & Hewitt, P. E. Creutzfeldt-Jakob disease and blood transfusion: updated results of the UK Transfusion Medicine Epidemiology Review Study. *Vox Sang* **110**, 310-316, (2016).

95   Safar, J. *et al.* Eight prion strains have PrP(Sc) molecules with different conformations. *Nat Med* **4**, 1157-1165, (1998).

96   Tamguney, G. & Korczyn, A. D. A critical review of the prion hypothesis of human synucleinopathies. *Cell Tissue Res* **373**, 213-220, (2018).

97   Hashimoto, M. *et al.* Human recombinant NACP/alpha-synuclein is aggregated and fibrillated in vitro: relevance for Lewy body disease. *Brain Res* **799**, 301-306, (1998).

98   Wood, S. J. *et al.* alpha-synuclein fibrillogenesis is nucleation-dependent. Implications for the pathogenesis of Parkinson's disease. *J Biol Chem* **274**, 19509-19512, (1999).

99   Narkiewicz, J., Giachin, G. & Legname, G. In vitro aggregation assays for the characterization of alpha-synuclein prion-like properties. *Prion* **8**, 19-32, (2014).

100   Buell, A. K. *et al.* Solution conditions determine the relative importance of nucleation and growth processes in alpha-synuclein aggregation. *Proc Natl Acad Sci U S A* **111**, 7671-7676, (2014).

101   Castilla, J., Saa, P., Hetz, C. & Soto, C. In vitro generation of infectious scrapie prions. *Cell* **121**, 195-206, (2005).

102   Atarashi, R., Sano, K., Satoh, K. & Nishida, N. Real-time quaking-induced conversion: a highly sensitive assay for prion detection. *Prion* **5**, 150-153, (2011).

103   Saborio, G. P., Permanne, B. & Soto, C. Sensitive detection of pathological prion protein by cyclic amplification of protein misfolding. *Nature* **411**, 810-813, (2001).

104   Fairfoul, G. *et al.* Alpha-synuclein RT-QuIC in the CSF of patients with alpha-synucleinopathies. *Ann Clin Transl Neurol* **3**, 812-818, (2016).

105   Herva, M. E. *et al.* Anti-amyloid compounds inhibit alpha-synuclein aggregation induced by protein misfolding cyclic amplification (PMCA). *J Biol Chem* **289**, 11897-11905, (2014).

106   Jung, B. C. *et al.* Amplification of distinct alpha-synuclein fibril conformers through protein misfolding cyclic amplification. *Exp Mol Med* **49**, e314, (2017).

107   Braak, H. & Braak, E. Neuropathological stageing of Alzheimer-related changes. *Acta Neuropathol* **82**, 239-259, (1991).

108   Braak, H. *et al.* Staging of brain pathology related to sporadic Parkinson's disease. *Neurobiol Aging* **24**, 197-211, (2003).

109   Braak, H. & Del Tredici, K. Neuropathological Staging of Brain Pathology in Sporadic Parkinson's disease: Separating the Wheat from the Chaff. *J Parkinsons Dis* **7**, S71-S85, (2017).

110   McKeith, I. G. *et al.* Consensus guidelines for the clinical and pathologic diagnosis of dementia with Lewy bodies (DLB): report of the consortium on DLB international workshop. *Neurology* **47**, 1113-1124, (1996).

111   Beach, T. G. *et al.* Unified staging system for Lewy body disorders: correlation with nigrostriatal degeneration, cognitive impairment and motor dysfunction. *Acta Neuropathol* **117**, 613-634, (2009).

112   Goedert, M., Spillantini, M. G., Del Tredici, K. & Braak, H. 100 years of Lewy pathology. *Nat Rev Neurol* **9**, 13-24, (2013).

113   Braak, H., Rub, U., Gai, W. P. & Del Tredici, K. Idiopathic Parkinson's disease: possible routes by which vulnerable neuronal types may be subject to neuroinvasion by an unknown pathogen. *J Neural Transm (Vienna)* **110**, 517-536, (2003).

114   Kordower, J. H., Chu, Y., Hauser, R. A., Freeman, T. B. & Olanow, C. W. Lewy body-like pathology in long-term embryonic nigral transplants in Parkinson's disease. *Nat Med* **14**, 504-506, (2008).

115   Li, J. Y. *et al.* Lewy bodies in grafted neurons in subjects with Parkinson's disease suggest host-to-graft disease propagation. *Nat Med* **14**, 501-503, (2008).

116   Steiner, J. A., Quansah, E. & Brundin, P. The concept of alpha-synuclein as a prion-like protein: ten years after. *Cell Tissue Res* **373**, 161-173, (2018).

117   Peelaerts, W. *et al.* alpha-Synuclein strains cause distinct synucleinopathies after local and systemic administration. *Nature* **522**, 340-344, (2015).

118   Abdelmotilib, H. *et al.* alpha-Synuclein fibril-induced inclusion spread in rats and mice correlates with dopaminergic Neurodegeneration. *Neurobiol Dis* **105**, 84-98, (2017).

119   Rey, N. L. *et al.* Widespread transneuronal propagation of alpha-synucleinopathy triggered in olfactory bulb mimics prodromal Parkinson's disease. *J Exp Med* **213**, 1759-1778, (2016).

120   Stopschinski, B. E. & Diamond, M. I. The prion model for progression and diversity of neurodegenerative diseases. *Lancet Neurol* **16**, 323-332, (2017).

121   Guo, J. L. *et al.* Distinct alpha-synuclein strains differentially promote tau inclusions in neurons. *Cell* **154**, 103-117, (2013).

122   Bousset, L. *et al.* Structural and functional characterization of two alpha-synuclein strains. *Nat Commun* **4**, 2575, (2013).

123   Beekes, M., Thomzig, A., Schulz-Schaeffer, W. J. & Burger, R. Is there a risk of prion-like disease transmission by Alzheimer- or Parkinson-associated protein particles? *Acta Neuropathol* **128**, 463-476, (2014).

124   Prusiner, S. B. *et al.* Evidence for alpha-synuclein prions causing multiple system atrophy in humans with parkinsonism. *Proc Natl Acad Sci U S A* **112**, E5308-5317, (2015).

125   Bernis, M. E. *et al.* Prion-like propagation of human brain-derived alpha-synuclein in transgenic mice expressing human wild-type alpha-synuclein. *Acta Neuropathol Commun* **3**, 75, (2015).

126   Vassar, P. S. & Culling, C. F. Fluorescent stains, with special reference to amyloid and connective tissues. *Arch Pathol* **68**, 487-498, (1959).

127   Puchtler, H., Sweat, F. & Levine, M. On the binding of Congo red by amyloid. *Journal of Histochemistry & Cytochemistry* **10**, 355-364, (1962).

128   Higuchi, M. *et al.* 19F and 1H MRI detection of amyloid beta plaques in vivo. *Nat Neurosci* **8**, 527-533, (2005).

129 Velasco, A. *et al.* Detection of filamentous tau inclusions by the fluorescent Congo red derivative FSB [(trans,trans)-1-fluoro-2,5-bis(3-hydroxycarbonyl-4-hydroxy)styrylbenzene]. *FEBS Lett* **582**, 901-906, (2008).

130 Condello, C. *et al.* Structural heterogeneity and intersubject variability of Abeta in familial and sporadic Alzheimer's disease. *Proc Natl Acad Sci U S A* **115**, E782-E791, (2018).

131 Sigurdson, C. J. *et al.* Prion strain discrimination using luminescent conjugated polymers. *Nat Methods* **4**, 1023-1030, (2007).

132 Klingstedt, T. *et al.* The structural basis for optimal performance of oligothiophene-based fluorescent amyloid ligands: conformational flexibility is essential for spectral assignment of a diversity of protein aggregates. *Chemistry* **19**, 10179-10192, (2013).

133 Tuttle, M. D. *et al.* Solid-state NMR structure of a pathogenic fibril of full-length human alpha-synuclein. *Nat Struct Mol Biol* **23**, 409-415, (2016).

134 Guerrero-Ferreira, R. *et al.* Cryo-EM structure of alpha-synuclein fibrils. *Elife* **7**, (2018).

135 Li, Y. *et al.* Amyloid fibril structure of alpha-synuclein determined by cryo-electron microscopy. *Cell Res* **28**, 897-903, (2018).

136 Delaglio, F. *et al.* NMRPipe: a multidimensional spectral processing system based on UNIX pipes. *J Biomol NMR* **6**, 277-293, (1995).

137 Jeschke, G. *et al.* DeerAnalysis2006 - a comprehensive software package for analyzing pulsed ELDOR data. *Appl Magn Reson* **30**, 473-498, (2006).

138 Worswick, S. G., Spencer, J. A., Jeschke, G. & Kuprov, I. Deep neural network processing of DEER data. *Sci Adv* **4**, eaat5218, (2018).

139 Vranken, W. F. *et al.* The CCPN data model for NMR spectroscopy: development of a software pipeline. *Proteins* **59**, 687-696, (2005).

140 Johnson, M., Coulton, A. T., Geeves, M. A. & Mulvihill, D. P. Targeted amino-terminal acetylation of recombinant proteins in E. coli. *PLoS One* **5**, e15801, (2010).

141 Xu, R. Light scattering: A review of particle characterization applications. *Particuology* **18**, 11-21, (2015).

142 Minton, A. P. Recent applications of light scattering measurement in the biological and biopharmaceutical sciences. *Anal Biochem* **501**, 4-22, (2016).

143 Burre, J. *et al.* Properties of native brain alpha-synuclein. *Nature* **498**, E4-6; discussion E6-7, (2013).

144 Naiki, H., Higuchi, K., Hosokawa, M. & Takeda, T. Fluorometric determination of amyloid fibrils in vitro using the fluorescent dye, thioflavin T1. *Anal Biochem* **177**, 244-249, (1989).

145 Greenfield, N. J. Using circular dichroism spectra to estimate protein secondary structure. *Nat Protoc* **1**, 2876-2890, (2006).

146 Farid, R. S. *Circular Dichroism (CD) Spectroscopy*, www.proteinchemist.com/cd/cdspec.html, (2003).

147 Klingstedt, T. *et al.* Distinct Spacing Between Anionic Groups: An Essential Chemical Determinant for Achieving Thiophene-Based Ligands to Distinguish beta-Amyloid or Tau Polymorphic Aggregates. *Chemistry* **21**, 9072-9082, (2015).

148 Bodenhausen, G. & Ruben, D. J. Natural abundance nitrogen-15 NMR by enhanced heteronuclear spectroscopy. *Chemical Physics Letters* **69**, 185-189, (1980).

149 Palmer, A. G., Cavanagh, J., Wright, P. E. & Rance, M. Sensitivity improvement in proton-detected two-dimensional heteronuclear correlation NMR spectroscopy. *Journal of Magnetic Resonance (1969)* **93**, 151-170, (1991).

150 Kay, L., Keifer, P. & Saarinen, T. Pure absorption gradient enhanced heteronuclear single quantum correlation spectroscopy with improved sensitivity. *Journal of the American Chemical Society* **114**, 10663-10665, (1992).

151 Schleucher, J. *et al.* A general enhancement scheme in heteronuclear multidimensional NMR employing pulsed field gradients. *Journal of Biomolecular NMR* **4**, 301-306, (1994).

152 Grzesiek, S. & Bax, A. Improved 3D triple-resonance NMR techniques applied to a 31 kDa protein. *Journal of Magnetic Resonance (1969)* **96**, 432-440, (1992).

153 Schleucher, J., Sattler, M. & Griesinger, C. Coherence Selection by Gradients without Signal Attenuation: Application to the Three-Dimensional HNCO Experiment. *Angewandte Chemie International Edition in English* **32**, 1489-1491, (1993).

154 Kay, L. E., Xu, G. Y. & Yamazaki, T. Enhanced-Sensitivity Triple-Resonance Spectroscopy with Minimal H2O Saturation. *Journal of Magnetic Resonance, Series A* **109**, 129-133, (1994).

155 Clubb, R. T., Thanabal, V. & Wagner, G. A constant-time three-dimensional triple-resonance pulse scheme to correlate intraresidue 1HN, 15N, and 13C′ chemical shifts in 15N-13C-labelled proteins. *Journal of Magnetic Resonance (1969)* **97**, 213-217, (1992).

156 Wittekind, M. & Mueller, L. HNCACB, a High-Sensitivity 3D NMR Experiment to Correlate Amide-Proton and Nitrogen Resonances with the Alpha- and Beta-Carbon Resonances in Proteins. *Journal of Magnetic Resonance, Series B* **101**, 201-205, (1993).

157 Muhandiram, D. R. & Kay, L. E. Gradient-Enhanced Triple-Resonance Three-Dimensional NMR Experiments with Improved Sensitivity. *Journal of Magnetic Resonance, Series B* **103**, 203-216, (1994).

158 Bax, A. Multidimensional Nuclear-Magnetic-Resonance Methods for Protein Studies. *Curr Opin Struc Biol* **4**, 738-744, (1994).

159 Mobli, M. & Hoch, J. C. Nonuniform sampling and non-Fourier signal processing methods in multidimensional NMR. *Prog Nucl Magn Reson Spectrosc* **83**, 21-41, (2014).

160 Ying, J., Delaglio, F., Torchia, D. A. & Bax, A. Sparse multidimensional iterative lineshape-enhanced (SMILE) reconstruction of both non-uniformly sampled and conventional NMR data. *J Biomol NMR* **68**, 101-118, (2017).

161 Schwarzinger, S. *et al.* Sequence-dependent correction of random coil NMR chemical shifts. *J Am Chem Soc* **123**, 2970-2978, (2001).

162 Cho, M. K., Kim, H. Y., Fernandez, C. O., Becker, S. & Zweckstetter, M. Conserved core of amyloid fibrils of wild type and A30P mutant alpha-synuclein. *Protein Sci* **20**, 387-395, (2011).

163 Hoshino, M. *et al.* Mapping the core of the beta(2)-microglobulin amyloid fibril by H/D exchange. *Nat Struct Biol* **9**, 332-336, (2002).

164 Vilar, M. *et al.* The fold of alpha-synuclein fibrils. *Proc Natl Acad Sci U S A* **105**, 8637-8642, (2008).

165 Pornsuwan, S. *et al.* Long-range distances in amyloid fibrils of alpha-synuclein from PELDOR spectroscopy. *Angew Chem Int Ed Engl* **52**, 10290-10294, (2013).

166 Stoll, S. & Schweiger, A. EasySpin, a comprehensive software package for spectral simulation and analysis in EPR. *J Magn Reson* **178**, 42-55, (2006).

167 Jeschke, G. Conformational dynamics and distribution of nitroxide spin labels. *Prog Nucl Magn Reson Spectrosc* **72**, 42-60, (2013).

168 Pannier, M., Veit, S., Godt, A., Jeschke, G. & Spiess, H. W. Dead-time free measurement of dipole-dipole interactions between electron spins. *Journal of Magnetic Resonance* **142**, 331-340, (2000).

169 Ree, R., Varland, S. & Arnesen, T. Spotlight on protein N-terminal acetylation. *Exp Mol Med* **50**, 90, (2018).

170 Bartels, T., Choi, J. G. & Selkoe, D. J. alpha-Synuclein occurs physiologically as a helically folded tetramer that resists aggregation. *Nature* **477**, 107-110, (2011).

171 Maltsev, A. S., Ying, J. & Bax, A. Impact of N-terminal acetylation of alpha-synuclein on its random coil and lipid binding properties. *Biochemistry* **51**, 5004-5013, (2012).

172 Miotto, M. C. *et al.* Copper binding to the N-terminally acetylated, naturally occurring form of alpha-synuclein induces local helical folding. *J Am Chem Soc* **137**, 6444-6447, (2015).

173 Li, B. *et al.* Cryo-EM of full-length alpha-synuclein reveals fibril polymorphs with a common structural kernel. *Nat Commun* **9**, 3609, (2018).

174 Krishna, M. M., Hoang, L., Lin, Y. & Englander, S. W. Hydrogen exchange methods to study protein folding. *Methods* **34**, 51-64, (2004).

175 Rodriguez, J. A. *et al.* Structure of the toxic core of alpha-synuclein from invisible crystals. *Nature* **525**, 486-490, (2015).

176 Chen, M., Margittai, M., Chen, J. & Langen, R. Investigation of alpha-synuclein fibril structure by site-directed spin labeling. *J Biol Chem* **282**, 24970-24979, (2007).

177 Toyama, B. H., Kelly, M. J., Gross, J. D. & Weissman, J. S. The structural basis of yeast prion strain variants. *Nature* **449**, 233-237, (2007).

178 Fitzpatrick, A. W. *et al.* Atomic structure and hierarchical assembly of a cross-beta amyloid fibril. *Proc Natl Acad Sci U S A* **110**, 5468-5473, (2013).

179 Miake, H., Mizusawa, H., Iwatsubo, T. & Hasegawa, M. Biochemical characterization of the core structure of alpha-synuclein filaments. *J Biol Chem* **277**, 19213-19219, (2002).

180 Crowther, R. A. Straight and paired helical filaments in Alzheimer disease have a common structural unit. *Proc Natl Acad Sci U S A* **88**, 2288-2292, (1991).

181 Fitzpatrick, A. W. P. *et al.* Cryo-EM structures of tau filaments from Alzheimer's disease. *Nature* **547**, 185-190, (2017).

182   Jucker, M. & Walker, L. C. Propagation and spread of pathogenic protein assemblies in neurodegenerative diseases. *Nat Neurosci* **21**, 1341-1349, (2018).

183   Spillantini, M. G. & Goedert, M. Tau pathology and neurodegeneration. *Lancet Neurol* **12**, 609-622, (2013).

184   Falcon, B. *et al.* Structures of filaments from Pick's disease reveal a novel tau protein fold. *Nature* **561**, 137-140, (2018).

185   Govaerts, C., Wille, H., Prusiner, S. B. & Cohen, F. E. Evidence for assembly of prions with left-handed beta-helices into trimers. *Proc Natl Acad Sci U S A* **101**, 8342-8347, (2004).

186   Peng, C. *et al.* Cellular milieu imparts distinct pathological alpha-synuclein strains in alpha-synucleinopathies. *Nature* **557**, 558-563, (2018).

187   Wang, J., Gu, B. J., Masters, C. L. & Wang, Y. J. A systemic view of Alzheimer disease - insights from amyloid-beta metabolism beyond the brain. *Nat Rev Neurol* **13**, 703, (2017).

188   Murphy, M. P. & LeVine, H., 3rd. Alzheimer's disease and the amyloid-beta peptide. *J Alzheimers Dis* **19**, 311-323, (2010).

189   Petkova, A. T. *et al.* Self-propagating, molecular-level polymorphism in Alzheimer's beta-amyloid fibrils. *Science* **307**, 262-265, (2005).

190   Petkova, A. T., Yau, W. M. & Tycko, R. Experimental constraints on quaternary structure in Alzheimer's beta-amyloid fibrils. *Biochemistry* **45**, 498-512, (2006).

191   Paravastu, A. K., Leapman, R. D., Yau, W. M. & Tycko, R. Molecular structural basis for polymorphism in Alzheimer's beta-amyloid fibrils. *Proc Natl Acad Sci U S A* **105**, 18349-18354, (2008).

192   Sachse, C., Fandrich, M. & Grigorieff, N. Paired beta-sheet structure of an Abeta(1-40) amyloid fibril revealed by electron microscopy. *Proc Natl Acad Sci U S A* **105**, 7462-7466, (2008).

193   Lu, J. X. *et al.* Molecular structure of beta-amyloid fibrils in Alzheimer's disease brain tissue. *Cell* **154**, 1257-1268, (2013).

194   Schmidt, M. *et al.* Peptide dimer structure in an Abeta(1-42) fibril visualized with cryo-EM. *Proc Natl Acad Sci U S A* **112**, 11858-11863, (2015).

195   Xiao, Y. *et al.* Abeta(1-42) fibril structure illuminates self-recognition and replication of amyloid in Alzheimer's disease. *Nat Struct Mol Biol* **22**, 499-505, (2015).

196   Walti, M. A. *et al.* Atomic-resolution structure of a disease-relevant Abeta(1-42) amyloid fibril. *Proc Natl Acad Sci U S A* **113**, E4976-4984, (2016).

197   Colvin, M. T. *et al.* Atomic Resolution Structure of Monomorphic Abeta42 Amyloid Fibrils. *J Am Chem Soc* **138**, 9663-9674, (2016).

198   Gremer, L. *et al.* Fibril structure of amyloid-beta(1-42) by cryo-electron microscopy. *Science* **358**, 116-119, (2017).

199   Qiang, W., Yau, W. M., Lu, J. X., Collinge, J. & Tycko, R. Structural variation in amyloid-beta fibrils from Alzheimer's disease clinical subtypes. *Nature* **541**, 217-221, (2017).

200   Wilkins, M. R. *et al.* Protein identification and analysis tools in the ExPASy server. *Methods Mol Biol* **112**, 531-552, (1999).

201 Spillantini, M. G., Divane, A. & Goedert, M. Assignment of human alpha-synuclein (SNCA) and beta-synuclein (SNCB) genes to chromosomes 4q21 and 5q35. *Genomics* **27**, 379-381, (1995).

202 Masaracchia, C. *et al.* Membrane binding, internalization, and sorting of alpha-synuclein in the cell. *Acta Neuropathol Commun* **6**, 79, (2018).

203 Miotto, M. C. *et al.* Bioinorganic Chemistry of Parkinson's Disease: Affinity and Structural Features of Cu(I) Binding to the Full-Length beta-Synuclein Protein. *Inorg Chem* **56**, 10387-10395, (2017).

204 Pfefferkorn, C. M. & Lee, J. C. Tryptophan probes at the alpha-synuclein and membrane interface. *J Phys Chem B* **114**, 4615-4622, (2010).

7 Appendix

7.1 Human *wt* α-synuclein sequence

7.1.1 Fasta sequence from Uniprot

```
>sp|P37840|SYUA_HUMAN Alpha-synuclein OS=Homo sapiens OX=9606 GN=SNCA
PE=1 SV=1
MDVFMKGLSKAKEGVVAAAEKTKQGVAEAAGKTKEGVLYVGSKTKEGVVHGVATVAEKTK
EQVTNVGGAVVTGVTAVAQKTVEGAGSIAAATGFVKKDQLGKNEEGAPQEGILEDMPVDP
DNEAYEMPSEEGYQDYEPEA
```

7.1.2 Physical and chemical parameters of α-synuclein

Number of amino acids: 140

Molecular weight: 14,460 Da

Theoretical pI: 4.67

Additional weight due to N-terminal acetylation: 42 Da

$H_3C-C=O$: 43 Da

Molecular weight of aSyn: 14,502 Da

Data obtained using FASTA sequences and ProtParam of SIB ExPASy server[200].

7.2 Resonance assignment of aSyn in dissociation buffer

#	Residue	H	N	C'	CA	CB
1	Met	8.18	126.14	176.51	56.34	33.22
2	Asp	8.39	119.59	174.87	53	38.03
3	Val	7.74	119.46	175.78	62.87	32.77
4	Phe	8.07	123.09	-	58.17	39.6
5	Met	8.03	121.74	175.92	55.73	33.12
6	Lys	8.06	122.27	177.06	57.28	33.25
7	Gly	8.22	110.02	174.06	45.67	-
8	Leu	7.95	121.68	177.5	55.32	42.62
9	Ser	8.18	116.72	174.64	58.57	64.14
10	Lys	8.21	123.45	176.52	56.93	33.16
11	Ala	8.13	124.64	-	53.06	19.46
12	Lys	8.1	120.53	176.68	56.84	33.19
13	Glu	8.19	120.96	175.98	56.27	-

15	Val	7.86	119.61	176.41	62.7	33.08
16	Val	8.02	123.75	176.04	62.5	33.12
17	Ala	8.21	127.63	177.7	53.01	19.39
18	Ala	8.11	123.16	177.76	53.1	19.38
19	Ala	8.1	122.67	177.84	52.96	19.47
20	Glu	8.08	119.02	176.15	56.12	28.92
21	Lys	8.15	122.33	176.76	57	33.31
22	Thr	8.03	114.56	174.63	61.88	70.48
23	Lys	8.19	123.62	176.58	57.05	33.21
26	Val	7.89	119.28	176.17	62.51	33.03
27	Ala	8.24	127.18	177.84	53.07	19.37
28	Glu	8.15	119.72	175.93	56.16	28.87
29	Ala	8.16	124.93	177.45	52.85	19.47
30	Ala	8.14	123.27	178.22	53.06	19.5
31	Gly	8.18	108.21	174.04	45.55	-
32	Lys	8.07	121.19	176.84	56.73	33.51
33	Thr	8.08	114.91	174.6	61.86	70.52
34	Lys	8.22	123.66	176.53	56.98	33.22
35	Glu	8.24	120.99	176.48	56.23	29.02
37	Val	7.86	119.09	176.02	62.5	32.98
38	Leu	8.05	125.06	176.69	55.32	42.51
39	Tyr	8	121.68	175.71	58.05	39
40	Val	7.91	122.27	176.21	62.5	32.98
41	Gly	7.87	112.04	173.94	45.49	-
42	Ser	8.14	115.77	174.75	58.57	64.37
43	Lys	8.32	123.53	176.76	57.06	33.22
44	Thr	8.03	114.48	174.62	61.88	-
45	Lys	8.2	123.53	176.68	57.01	33.23
47	Gly	8.25	110.37	173.75	45.56	-
48	Val	7.85	119.45	176.14	62.3	33.16
49	Val	8.05	123.92	175.82	62.61	32.99
50	His	8.4	122.13	174.56	55.3	29.53
51	Gly	8.32	110.75	-	45.56	-
52	Val	7.99	119.21	175.91	62.21	33.23
53	Ala	8.28	127.71	177.76	52.81	19.63
54	Thr	8	113.49	174.66	61.71	70.48

55	Val	8.01	121.58	176.07	62.72	32.98
56	Ala	8.21	127.09	177.76	53.06	19.46
57	Glu	8.1	119.77	176.26	56.27	28.95
58	Lys	8.22	122.31	176.89	57.03	33.36
59	Thr	8.07	114.7	174.68	62.12	70.37
60	Lys	8.16	123.32	176.7	57.16	33.2
62	Gln	8.24	121.54	175.99	56.27	29.68
63	Val	8.1	121.04	176.27	62.65	33.2
64	Thr	8.09	116.79	174.1	61.75	70.33
65	Asn	8.34	121.61	175.18	53.24	39.1
66	Val	8.07	120.01	176.68	62.78	32.8
67	Gly	8.34	112.33	174.58	45.6	-
68	Gly	8.15	109.18	173.75	45.35	-
69	Ala	8.12	124.16	177.64	52.72	19.66
70	Val	8.02	119.87	176.2	62.59	32.96
71	Val	8.11	124.3	176.17	62.35	32.97
72	Thr	8.12	117.35	174.96	61.76	70.41
73	Gly	8.24	111.29	173.94	45.55	-
74	Val	7.96	119.19	176.43	62.53	33.09
75	Thr	8.09	117.33	174.19	61.75	70.3
76	Ala	8.17	126.68	177.57	52.88	19.61
77	Val	7.93	118.99	175.98	62.42	33.07
78	Ala	8.19	127.51	177.58	52.88	19.44
79	Gln	8.21	120.04	175.95	56.16	29.78
80	Lys	8.23	122.67	176.65	56.96	33.44
81	Thr	8.09	115.42	174.5	61.86	70.45
82	Val	8.05	122.05	176.15	62.52	33.02
83	Glu	8.29	123.74	176.48	56.2	28.93
84	Gly	8.28	110.62	173.89	45.54	-
85	Ala	8.20	124.15	178.28	53.17	19.59
86	Gly	8.34	108.53	174.13	45.49	-
87	Ser	8.09	115.97	174.73	58.41	64.37
88	Ile	8.09	122.57	176.27	61.84	38.91
89	Ala	8.18	127.51	177.64	52.97	19.44
90	Ala	8.05	123.02	177.67	52.92	19.46
91	Ala	8.13	123.26	177.91	-	-

92	Thr	7.97	111.85	175.1	61.92	70.34
93	Gly	8.16	110.91	173.5	45.44	-
94	Phe	8.02	120.78	175.44	58.1	40.03
95	Val	7.87	122.89	175.57	62.14	33.27
96	Lys	8.15	125.86	176.66	56.96	-
97	Lys	8.18	122.6	176.43	57.22	33.24
98	Asp	8.29	119.29	175.03	53.2	38.13
99	Gln	8.22	120.74	175.94	56.23	29.58
100	Leu	8.05	122.63	177.84	55.59	42.41
101	Gly	8.21	109.73	174.22	45.59	-
102	Lys	8.09	121.06	176.52	57	33.45
103	Asn	8.39	119.52	175.21	53.49	38.9
107	Ala	8.07	124.88	175.62	50.91	18.44
108	Pro	-	-	176.92	63.59	32.27
109	Gln	8.37	120.53	175.88	56.16	29.56
110	Glu	8.25	121.15	176.33	56.15	29.12
111	Gly	8.29	110.43	173.96	45.61	-
112	Ile	7.87	119.93	176.42	61.63	39
113	Leu	8.09	125.34	177.36	55.52	42.03
114	Glu	8.11	120.36	175.62	56.12	28.74
115	Asp	8.25	119.48	174.45	52.83	38.33
116	Met	8.05	121.37	174.09	53.7	32.68
117	Pro	-	-	176.51	63.28	32.45
118	Val	8.07	120.27	175.45	62.66	33
119	Asp	8.38	122.39	173.15	51.05	38.34
120	Pro	-	-	176.69	64.03	32.32
121	Asp	8.23	117.78	174.89	53.15	37.96
122	Asn	8.15	119.17	175.25	53.45	38.96
123	Glu	8.1	120.3	175.79	56.87	28.68
124	Ala	8.13	124.45	177.34	53.03	19.38
125	Tyr	7.89	119.09	175.55	58.18	38.97
126	Glu	7.96	121.61	175.16	55.45	29.3
127	Met	8.14	122.55	174.36	53.74	32.71
128	Pro	-	-	176.88	63.77	32.32
129	Ser	8.27	115.92	174.74	58.67	64.06
130	Glu	8.29	122.09	175.97	56.09	28.81

131	Glu	8.27	120.85	176.42	56.3	28.89
132	Gly	8.21	110.11	173.85	45.48	-
133	Tyr	7.99	120.49	175.97	58.49	38.99
134	Gln	8.21	121.47	175.31	56.13	29.41
135	Asp	8.15	119.76	174.37	52.93	38.23
136	Tyr	7.98	121.3	175.11	58.18	39.07
137	Glu	8.00	123.23	173.53	53.3	28.75
138	Pro	-	-	176.7	63.45	32.35
139	Glu	8.26	120.15	175.57	55.88	28.94
140	Ala	8.19	126.58	179.39	52.04	19.22

Table 5. Resonance assignment of aSyn in dissociation buffer.

7.3 HS-68 synthesis report

a

Dioxan

1.91 2.94
1.07 1.09

1.98
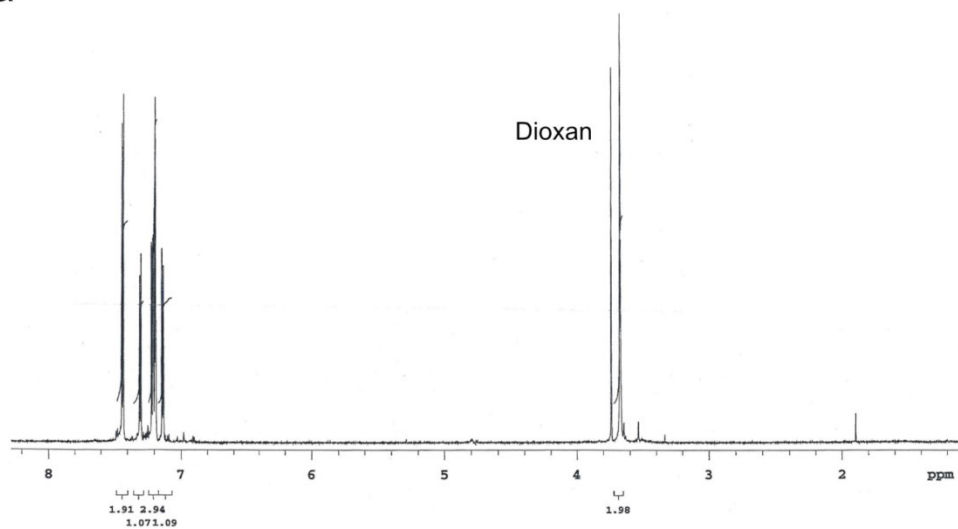
b
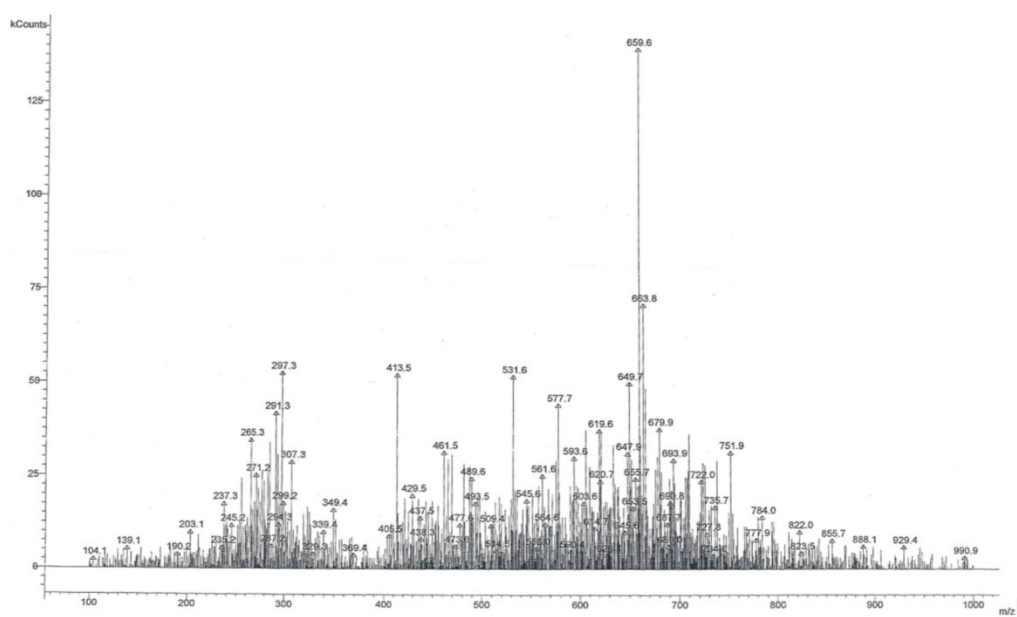
Figure 7-1. Synthesis report of HS-68.

(a) ^{1}H NMR spectrum and (b) mass spectrum of HS-68.

7.4 Mass spectrometry of non-acetylated α-synuclein

a

b

c
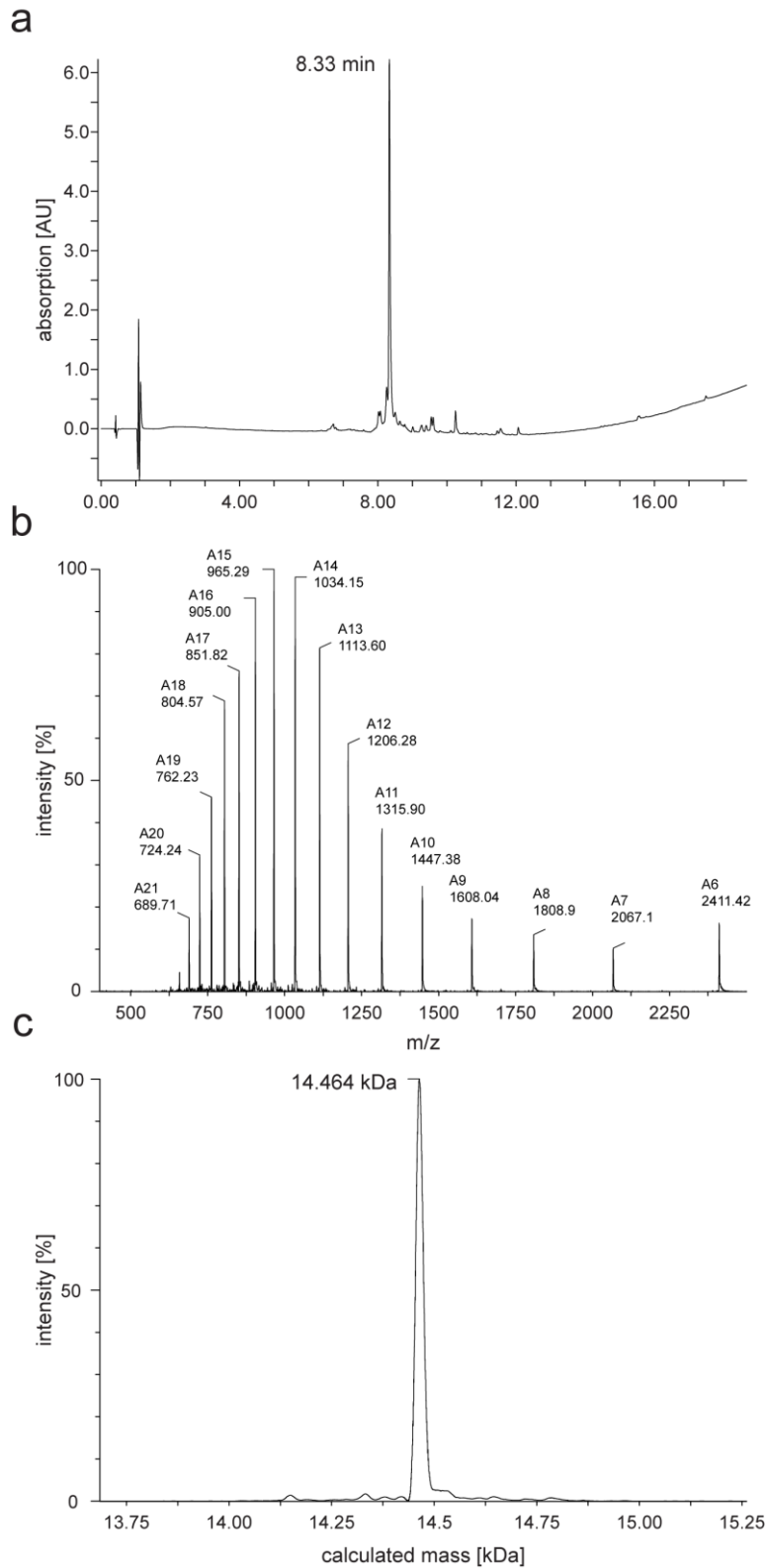
Figure 7-2. Mass spectrometry of non-acetylated α-synuclein

(a) HPLC run of non-acetylated α-synuclein. (b) M/z spectrum of α-synuclein. (c) Calculated average mass for HPLC elution.

7.5   Pulse sequence used for real-time HD back-exchange

7.5.1   HSQC pulse program

```
;hsqcetf3gpsi
;avance-version (12/01/11)
;HSQC
;2D H-1/X correlation via double inept transfer
;   using sensitivity improvement
;phase sensitive using Echo/Antiecho-TPPI gradient selection
;with decoupling during acquisition
;using trim pulses in inept transfer
;using f3 - channel
;
;A.G. Palmer III, J. Cavanagh, P.E. Wright & M. Rance, J. Magn.
;   Reson. 93, 151-170 (1991)
;L.E. Kay, P. Keifer & T. Saarinen, J. Am. Chem. Soc. 114,
;   10663-5 (1992)
;J.  Schleucher,  M.  Schwendinger,  M.  Sattler,  P.  Schmidt,  O.
Schedletzky,
;   S.J. Glaser, O.W. Sorensen & C. Griesinger, J. Biomol. NMR 4,
;   301-306 (1994)
;
;$CLASS=HighRes
;$DIM=2D
;$TYPE=
;$SUBTYPE=
;$COMMENT=

#include <Avance.incl>
#include <Grad.incl>
#include <Delay.incl>

"p2=p1*2"
"p22=p21*2"
"d11=30m"
"d26=1s/(cnst4*4)"

"d0=3u"

"in0=inf1/2"

"DELTA1=p16+d16-p1*0.78+de+8u"

#   ifdef LABEL_CN
"DELTA=p16+d16+larger(p2,p14)+d0*2"
#   else
"DELTA=p16+d16+p2+d0*2"
#   endif /*LABEL_CN*/


"acqt0=0"
baseopt_echo

1 ze
  d11 pl16:f3
2 d1 do:f3
3 (p1 ph1)
  d26 pl3:f3
  (center (p2 ph1) (p22 ph6):f3 )
```

```
  d26 UNBLKGRAD
  p28 ph1
  4u
  (p1 ph2)
  3u
  p16:gp1
  d16
  (p21 ph3):f3
  d0

#   ifdef LABEL_CN
  (center (p2 ph7) (p14:sp3 ph1):f2 )
#   else
  (p2 ph7)
#   endif /*LABEL_CN*/

  d0
  p16:gp2*EA
  d16
  (p22 ph4):f3
  DELTA
  (center (p1 ph1) (p21 ph4):f3 )
  d24
  (center (p2 ph1) (p22 ph1):f3 )
  d24
  (center (p1 ph2) (p21 ph5):f3 )
  d26
  (center (p2 ph1) (p22 ph1):f3 )
  d26
  (p1 ph1)
  DELTA1
  (p2 ph1)
  4u
  p16:gp3
  d16 pl16:f3
  4u BLKGRAD
  go=2 ph31 cpd3:f3
  d1 do:f3 mc #0 to 2
     F1EA(calgrad(EA)  &  calph(ph5,  +180),  caldel(d0,  +in0)  &
calph(ph3, +180) & calph(ph6, +180) & calph(ph31, +180))
exit

ph1=0
ph2=1
ph3=0 2
ph4=0 0 2 2
ph5=1 1 3 3
ph6=0
ph7=0 0 2 2
ph31=0 2 2 0


;pl1 : f1 channel - power level for pulse (default)
;pl3 : f3 channel - power level for pulse (default)
;pl16: f3 channel - power level for CPD/BB decoupling
;sp3: f2 channel - shaped pulse 180 degree (adiabatic)
;p1 : f1 channel -  90 degree high power pulse
;p2 : f1 channel - 180 degree high power pulse
;p14: f2 channel - 180 degree shaped pulse for inversion (adiabatic)
;p16: homospoil/gradient pulse                          [1 msec]
;p21: f3 channel -  90 degree high power pulse
;p22: f3 channel - 180 degree high power pulse
```

```
;p28: f1 channel - trim pulse                    [1 msec]
;d0 : incremented delay (2D)                     [3 usec]
;d1 : relaxation delay; 1-5 * T1
;d11: delay for disk I/O                         [30 msec]
;d16: delay for homospoil/gradient recovery
;d24: 1/(4J)YH for YH
;     1/(8J)YH for all multiplicities
;d26: 1/(4J(YH))
;cnst4: = J(YH)
;inf1: 1/SW(X) = 2 * DW(X)
;in0: 1/(2 * SW(X)) = DW(X)
;nd0: 2
;ns: 1 * n
;ds: >= 16
;td1: number of experiments
;FnMODE: echo-antiecho
;cpd3: decoupling according to sequence defined by cpdprg3
;pcpd3: f3 channel - 90 degree pulse for decoupling sequence


;use gradient ratio:    gp 1 : gp 2 : gp 3
;                 50 :   80 : 20.1       for C-13
;                 50 :   80 :  8.1       for N-15


;for z-only gradients:
;gpz1: 50%
;gpz2: 80%
;gpz3: 20.1% for C-13, 8.1% for N-15


;use gradient files:
;gpnam1: SMSQ10.100
;gpnam2: SMSQ10.100
;gpnam3: SMSQ10.100


                                        ;preprocessor-flags-start
;LABEL_CN: for C-13 and N-15 labeled samples start experiment with
;           option -DLABEL_CN (eda: ZGOPTNS)
                                        ;preprocessor-flags-end

;$Id: hsqcetf3gpsi,v 1.7 2012/01/31 17:49:26 ber Exp $
```

7.5.2 HSQC acquisition parameters

AQ_mod	DQD	
FnTYPE	traditional(planes)	
FnMODE	Echo-Antiecho	
TD	F2: 2048	F1:128
DS	4	
NS	4	
SW [ppm]	F2: 10.78	F1: 22.04
O1P [ppm]	F2: 4.69	F1: 118.00

Table 6. HSQC acquisition parameters.

7.6 Residue-specific protonation levels of aSyn fibrils

7.6.1 aSyn fibrils seeded by brain extract of patient brain

ID	AA	PD1	PD2	PD3	DLB1	DLB2	DLB1_rep	MSA1	MSA2
1	M	30.1	24.3	36.6	30.1	34.0	35.8	18.4	33.3
3	V	21.1	16.3	17.4	17.5	13.2	23.1	7.6	14.0
4	F	17.7	14.7	19.2	19.1	13.4	13.6	8.9	13.2
5	M	20.4	15.9	15.4	18.8	11.3	20.3	11.1	10.6
6	K	28.5	22.0	25.2	19.1	19.1	24.9	16.8	19.9
7	G	11.3	16.5	14.5	14.7	7.1	17.8	5.5	9.0
9	S	20.4	15.5	16.9	17.6	12.5	22.8	9.5	15.3
11	A	9.9	8.6	12.9	8.3	5.7	8.7	-0.3	11.8
12	K	6.8	10.3	12.1	7.9	7.1	13.3	1.4	7.7
15	V	27.2	26.5	38.0	38.9	34.7	38.2	47.7	46.1
16	V	32.3	36.7	45.3	49.2	55.5	50.2	65.6	63.3
17	A	36.2	38.2	49.2	53.1	56.1	55.9	68.0	66.2
18	A	37.4	38.9	43.8	50.0	52.6	52.3	63.5	62.4
19	A	32.0	42.6	38.5	46.4	46.4	45.6	59.1	52.4
20	E	30.7	30.7	40.2	49.4	51.5	42.6	62.1	59.7
21	K	30.3	28.0	39.0	48.0	45.9	41.4	60.5	58.8
22	T	29.4	32.9	39.5	43.8	44.1	43.8	66.4	54.9
26	V	24.1	27.9	31.5	35.8	37.5	26.1	52.0	53.9
27	A	32.1	32.5	39.4	53.5	45.9	43.2	60.0	63.3
29	A	29.9	33.4	37.2	49.3	45.6	44.1	60.0	59.5
31	G	33.5	32.3	44.2	47.8	46.2	40.9	56.3	60.7
32	K	23.4	27.1	33.6	34.2	28.9	19.7	47.7	49.3
33	T	7.1	11.5	5.5	5.9	3.7	3.0	5.0	9.2
34	K	27.7	31.0	34.3	39.5	38.5	35.7	56.5	54.6
35	E	32.6	36.5	43.9	46.6	45.1	44.5	63.5	62.7
37	V	43.7	47.7	50.0	49.2	54.0	51.1	61.5	67.7
38	L	47.7	54.4	67.7	58.3	56.7	67.2	68.9	66.5
40	V	63.1	58.2	64.2	74.4	66.7	62.6	80.5	83.2
41	G	47.3	47.2	54.6	58.3	46.3	47.8	61.0	56.5
42	S	30.8	38.4	51.2	47.6	47.6	48.5	58.3	61.5
43	K	33.0	33.5	50.3	53.7	48.2	52.1	63.5	62.5
44	T	31.6	33.6	48.8	55.5	54.8	57.9	67.6	61.7
48	V	44.7	40.9	50.4	56.2	45.6	64.4	61.8	60.1
49	V	80.4	86.3	75.8	80.9	78.6	72.8	83.6	81.6
50	H	73.5	70.6	66.5	77.0	64.8	75.4	76.6	75.6
51	G	65.5	74.1	69.4	73.8	63.6	65.1	75.4	69.5
52	V	92.6	94.6	84.0	92.0	90.7	86.5	90.0	89.0
53	A	84.5	97.4	88.6	79.9	86.6	77.9	81.3	84.8

54	T	96.2	96.1	84.0	86.0	87.9	76.9	83.2	87.5
56	A	96.7	89.0	83.6	81.9	74.5	76.8	80.8	83.9
57	E	72.2	65.3	75.9	59.6	55.6	44.0	51.5	56.4
58	K	87.8	85.3	77.5	79.8	70.2	71.6	79.4	81.7
59	T	71.2	74.7	75.0	66.7	70.4	66.4	80.5	65.7
60	K	34.5	31.9	24.6	22.7	16.5	13.9	14.9	11.5
62	Q	84.6	81.4	72.8	78.0	71.7	57.5	64.4	71.7
64	T	91.1	90.7	83.6	84.7	84.9	88.7	89.8	88.9
65	N	100.8	96.7	77.9	87.7	85.2	99.3	81.8	87.6
66	V	99.4	96.5	104.9	104.8	94.4	94.3	102.6	99.4
67	G	99.9	101.5	98.4	78.5	93.2	82.9	88.5	97.4
68	G	72.1	81.4	71.6	74.5	76.0	76.4	73.8	79.9
69	A	74.0	74.7	76.4	66.1	41.6	77.8	80.6	80.7
70	V	99.6	100.3	95.7	100.6	97.6	96.9	96.5	101.7
71	V	100.2	93.6	92.3	100.4	105.6	111.4	106.9	102.1
72	T	93.9	92.6	98.0	93.7	92.6	91.3	91.0	94.0
73	G	73.2	72.3	63.6	55.7	56.8	64.9	40.6	46.9
74	V	93.2	100.8	90.5	85.2	91.0	93.8	72.7	80.0
75	T	92.7	97.9	99.7	92.1	100.9	98.2	98.3	97.8
76	A	96.6	99.0	95.6	97.3	101.5	87.4	95.2	99.1
77	V	99.5	98.4	95.9	96.9	91.8	85.5	93.6	96.0
79	Q	90.0	88.4	93.2	90.3	86.2	83.3	95.6	91.8
80	K	94.5	92.5	99.0	82.3	77.4	86.1	81.9	85.4
81	T	85.1	80.3	82.3	85.1	81.1	71.1	90.1	78.5
82	V	78.7	82.2	79.6	74.3	70.2	73.3	69.8	77.5
83	E	47.6	43.7	51.6	69.8	55.3	60.3	74.0	61.9
84	G	34.2	39.0	44.6	55.3	53.1	44.6	74.8	67.7
85	A	34.3	32.5	37.7	46.5	45.2	36.8	59.1	58.5
86	G	35.5	36.7	53.1	54.8	55.7	51.8	71.9	63.2
87	S	38.0	35.9	39.6	55.3	50.9	56.0	70.5	66.0
88	I	36.8	43.1	52.4	68.0	57.0	54.0	69.3	70.1
90	A	35.2	34.0	40.5	51.4	34.1	51.2	60.3	55.9
92	T	24.4	24.5	26.2	38.6	28.5	46.5	34.2	37.5
93	G	23.4	24.1	29.3	37.4	23.2	30.6	30.1	35.4
94	F	22.8	19.0	25.6	37.9	26.9	26.3	27.0	31.8
95	V	22.5	18.1	29.6	35.5	23.0	37.2	28.0	32.1
96	K	17.1	21.9	29.4	31.2	23.2	31.2	25.5	28.7
97	K	10.5	13.6	18.8	18.4	17.4	15.1	13.1	14.7
98	D	1.5	7.8	8.8	7.7	5.2	0.1	0.5	2.8
99	Q	10.4	7.0	7.6	5.9	2.7	3.1	3.2	7.4
100	L	5.0	4.2	5.9	2.7	6.2	3.6	1.9	6.4
101	G	0.2	5.9	8.7	6.4	1.4	4.5	5.7	2.1
107	A	24.3	21.6	20.6	21.2	22.0	36.0	4.4	20.0

109	Q	9.6	8.5	18.3	9.2	5.1	1.4	8.4	9.1
110	E	7.7	13.4	14.2	17.2	9.1	13.7	9.5	12.0
111	G	8.9	5.3	9.7	15.8	7.9	0.4	9.4	9.3
112	I	8.7	7.1	9.1	5.7	6.2	0.8	5.3	7.7
113	L	3.0	2.3	1.1	2.6	-2.0	-0.3	3.7	2.3
115	D	8.2	8.3	7.6	13.1	6.9	-6.1	4.1	6.8
116	M	-3.1	0.7	-1.9	-1.1	-0.5	0.6	0.6	-1.4
118	V	9.1	7.4	0.0	7.1	4.9	6.8	6.4	5.3
119	D	12.5	10.8	16.0	18.2	7.4	13.3	12.0	12.2
121	D	5.9	13.5	10.9	9.9	9.7	3.5	5.8	16.3
122	N	2.4	4.4	7.6	5.7	0.1	-4.5	4.3	1.5
127	M	0.0	2.7	-0.5	0.7	-0.6	-0.5	0.8	-2.3
129	S	2.1	6.9	7.8	3.2	7.6	14.7	5.0	5.4
130	E	6.1	4.8	1.5	6.2	3.9	1.9	5.3	4.8
131	E	6.6	3.6	5.5	7.0	5.6	4.2	8.5	11.7
132	G	10.3	10.6	9.4	10.6	7.2	7.7	7.5	5.3
133	Y	7.5	7.7	3.9	8.8	6.1	7.4	10.0	6.3
134	E	7.1	7.6	0.7	-0.1	5.8	9.1	-1.1	3.7
136	Y	4.3	4.9	6.0	2.0	4.1	6.8	2.5	7.0
137	E	5.0	0.6	3.9	5.1	3.4	5.4	2.5	6.1
139	E	11.8	11.7	9.7	8.5	5.4	3.8	10.1	9.2
140	A	8.0	7.4	10.4	6.2	4.9	8.3	10.2	5.3

Table 7. Back-fitted initial protonation levels of brain-extract seeded aSyn fibrils.

Values report the residue-specific protonation levels [% ^{1}H] of brain-extract seeded aSyn fibrils amplified from distinct patient brains (Table 1) after 1.5 days of forward-exchange in 99.9 % D_2O supplemented with 0.1% formic acid (pD 4.0) at 37 °C.

7.6.2   *In vitro* aSyn polymorph fibrils

ID	AA	*de novo* hsAsyn	hsAsyn I	hsAsyn II	high salt [HEPES]	lsAsyn I	lsAsyn II
1	M	31.5	30.8	31.5	22.3	43.6	43.4
3	V	22.2	26.2	24.5	37.8	85.2	77.9
4	F	17.9	21.1	21.3	34.3	89.4	85.5
5	M	19.0	20.1	20.8	39.2	91.0	85.7
6	K	28.1	28.5	25.9	47.7	85.2	88.2
7	G	18.0	21.7	20.2	27.4	72.4	68.2
9	S	19.7	20.0	19.0	36.5	86.7	76.4
11	A	13.6	6.9	3.5	27.5	94.9	91.9
12	K	4.5	14.9	13.0	25.4	84.5	75.7
15	V	22.6	26.5	21.3	37.0	79.1	75.8
16	V	22.3	24.9	21.1	38.2	97.8	88.4
17	A	27.2	25.5	23.9	40.4	94.5	94.6
18	A	31.9	31.3	27.6	42.1	87.0	86.8
20	E	19.3	6.2	5.0	34.4	91.3	90.6
21	K	18.4	15.4	13.5	36.3	93.4	85.5
22	T	30.6	27.1	27.0	35.0	78.8	75.8
26	V	16.1	28.9	26.0	36.7	79.0	82.8
27	A	17.9	28.8	26.7	35.5	75.9	71.6
29	A	15.4	27.9	25.8	34.0	52.8	54.4
31	G	18.7	30.3	26.0	33.9	18.9	18.7
32	K	18.7	26.4	25.2	31.0	17.6	19.6
33	T	8.4	23.4	20.1	22.6	25.9	21.6
34	K	12.6	8.5	8.7	30.6	17.5	19.6
37	V	42.2	46.2	41.2	35.0	32.6	34.6
38	L	84.9	70.2	70.8	67.2	89.9	85.6
40	V	88.9	78.8	74.8	74.4	85.8	88.1
41	G	91.3	77.2	66.5	48.4	85.3	95.7
42	S	69.7	65.9	69.6	55.3	88.6	87.6
43	K	79.6	85.3	85.5	70.6	85.4	91.1
44	T	68.0	75.2	77.6	76.8	100.4	98.9
49	V	94.3	97.3	92.5	93.3	94.6	91.4
50	H	94.0	86.8	89.9	90.9	87.6	90.2
51	G	87.9	92.0	89.7	84.9	88.7	91.9
52	V	99.1	101.4	101.4	99.9	99.4	104.7
53	A	91.8	93.9	87.8	95.3	91.8	89.4
54	T	96.6	94.9	97.5	94.4	92.3	95.5
56	A	96.1	93.8	93.2	94.6	89.8	98.1
57	E	84.7	86.6	90.3	85.3	73.9	81.8
58	K	91.3	89.0	87.5	80.5	87.8	86.3

59	T	62.4	37.1	36.0	46.2	77.2	78.1
60	K	72.6	80.7	88.7	58.7	34.2	36.7
62	Q	84.9	84.2	89.2	85.3	81.8	86.3
64	T	94.0	93.8	96.9	92.3	86.8	89.8
65	N	95.4	91.3	87.6	88.3	88.4	93.3
66	V	99.9	99.5	94.7	88.1	92.7	92.1
67	G	91.4	90.0	89.6	94.3	64.1	69.8
68	G	83.8	83.4	80.9	64.6	33.1	28.2
69	A	76.1	79.5	85.4	74.9	38.7	37.4
70	V	100.8	96.9	99.9	92.0	91.4	97.2
71	V	98.5	94.5	88.8	104.5	93.9	90.5
72	T	98.5	96.6	94.9	98.4	91.4	84.4
73	G	68.7	48.3	48.6	82.4	87.9	81.5
74	V	99.6	104.0	100.4	97.7	98.3	97.4
75	T	92.1	95.9	95.0	95.9	94.4	96.5
76	A	99.4	96.6	97.4	98.2	98.1	100.9
77	V	88.6	88.2	85.3	85.2	94.8	87.8
79	Q	94.7	94.1	95.0	91.8	103.7	85.8
80	K	97.5	92.9	97.2	90.5	94.2	92.3
81	T	100.3	97.8	100.8	98.9	89.6	96.2
82	V	87.6	91.0	87.1	82.8	84.1	86.2
83	E	94.0	92.2	90.9	70.9	88.7	85.4
84	G	53.5	66.7	62.6	41.8	69.1	65.7
85	A	20.2	7.3	5.7	9.2	64.2	60.9
86	G	85.3	92.2	90.8	76.4	91.1	91.8
87	S	88.9	92.6	91.9	89.8	82.5	85.3
88	I	84.2	83.4	81.9	78.4	89.1	89.8
90	A	78.1	78.4	77.7	75.4	81.4	86.2
92	T	88.0	82.2	80.9	95.7	86.5	91.5
93	G	69.5	54.6	55.9	87.1	88.5	86.6
94	F	69.8	50.2	51.7	76.9	85.3	83.0
95	V	65.6	45.8	48.7	75.9	89.2	90.6
96	K	61.6	37.2	37.1	67.4	87.1	86.5
97	K	38.7	16.5	15.7	34.1	37.9	37.2
98	D	5.6	6.5	4.0	8.0	0.6	5.7
99	Q	14.1	9.4	6.8	7.8	15.0	17.5
100	L	9.7	8.4	7.5	10.1	12.2	16.0
101	G	8.6	6.5	4.1	7.3	10.0	9.5
107	A	18.9	14.5	13.9	13.4	23.0	13.7
109	Q	7.2	9.2	7.6	10.1	13.3	13.7
110	E	22.9	22.6	15.6	10.6	19.4	20.9
111	G	11.9	12.0	11.0	9.9	12.7	10.5
112	I	5.2	7.8	5.3	9.9	19.4	16.5

| 113	L	3.2	3.0	3.2	0.9	10.8	11.0
115	D	11.9	11.3	12.4	14.4	13.4	12.3
116	M	-2.3	-1.8	-1.3	0.1	-3.5	-3.0
118	V	5.2	5.2	5.6	11.7	9.9	5.7
119	D	14.5	11.7	8.6	11.0	13.3	14.7
121	D	8.4	8.7	6.1	10.3	15.8	8.5
122	N	2.0	1.1	1.5	3.1	-2.0	-1.5
127	M	-0.8	0.1	0.5	-1.2	0.6	-4.0
129	S	7.1	6.4	4.3	7.5	5.8	5.7
130	E	5.4	7.8	5.1	9.9	8.4	7.9
131	E	9.0	8.1	7.4	9.3	9.6	8.2
133	Y	5.7	7.3	4.5	8.1	8.9	6.0
134	E	6.2	7.1	6.6	7.2	4.1	7.0
136	Y	9.6	5.9	6.1	6.4	6.3	6.5
137	E	4.3	6.1	5.4	5.0	7.4	9.2
139	E	9.1	8.8	7.2	9.5	6.9	7.6
140	A	8.0	6.6	7.9	7.2	6.9	7.6

Table 8. Back-fitted initial protonation levels of aSyn *in vitro* polymorph fibrils.

Values report the residue-specific protonation levels [% ^{1}H] of *in vitro* aSyn polymorph fibrils after 1.5 days of forward-exchange in 99.9 % D_2O supplemented with 0.1% formic acid (pD 4.0) at 37 °C.

7.7 Dipolar modulation of aSyn *in vitro* polymorphs analyzed by DEERNet neural network

Here, an alternative processing of PELDOR experiments to the standard Tikhonov regularization with L-curve selection (Figure 3-25 a) is shown for the two *in vitro* aSyn polymorphs, hsAsyn and lsAsyn (Figure 7-3). The approach is based on the DEERNet neural network included in DEERAnalysis2018 and described in detail by Worswick et al.[138].
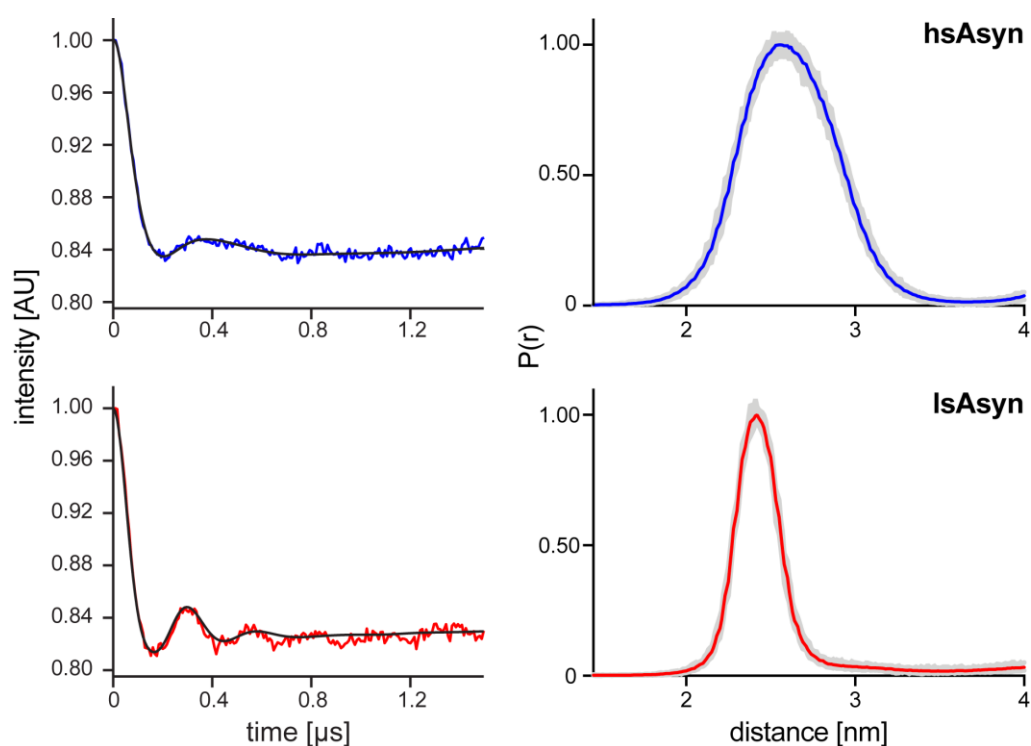
Figure 7-3. Dipolar modulation of aSyn fibrils using DEERNet.
Dipolar modulation (corrected for background; fit in blue/red, same as in Figure 3-25 a) and normalized distance distribution determined by 34 GHz four-pulse PELDOR experiments for hsAsyn (top, blue) and lsAsyn (bottom, red) analyzed by deep neural network processing[138] using DEERAnalysis2018 and DEERNet with "broad peak" model.

The distance distribution obtained by Tikhonov regularization with L-curve selection is faithfully reproduced on the same raw dataset with highly efficient suppression of distance artifacts.

7.8 Biophysical characterization of α-synuclein membrane interactions and the close homologue β-synuclein

A biophysical characterization of N-terminally acetylated α-synuclein and its close homologue β-synuclein[201] in the presence of mildly negatively charged small unilamellar vesicles (SUVs) of DOPE/DOPS/DOPC[202] (5:3:12, w/w) by two-dimensional ^{1}H-^{15}N NMR correlation spectroscopy and circular dichroism (CD) was conducted. N-terminally acetylated β-synuclein (bSyn) was expressed and purified as described by Miotto et al.[203]. The SUVs were generated following a published procedure[202] using a 1:1 mixture of DOPC and coagulation reagent I containing DOPE/DOPS/DOPC (5:3:12, w/w), both purchased from Avanti Polar Lipids. The total phospholipid concentration of the SUV stock was 85 mM (6.6% w/v).

7.8.1 Protein-membrane interactions by NMR spectroscopy

The ^{1}H-^{15}N HSQC spectra of the SUV titration experiment (Figure 7-4) were acquired on a 600 MHz Bruker NMR spectrometer equipped with a cryoprobe. MES was used as a buffer system (20 mM MES, 100 mM NaCl, pH 6.5, 0.02% NaN$_3$). The assignment for α- and β-synuclein was kindly provided by Dr. Fernández.

a
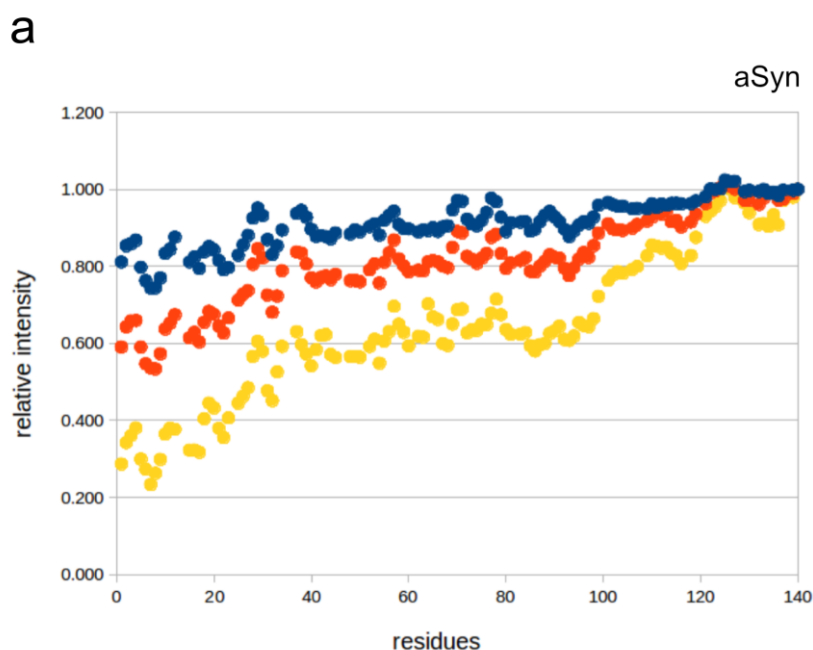
b
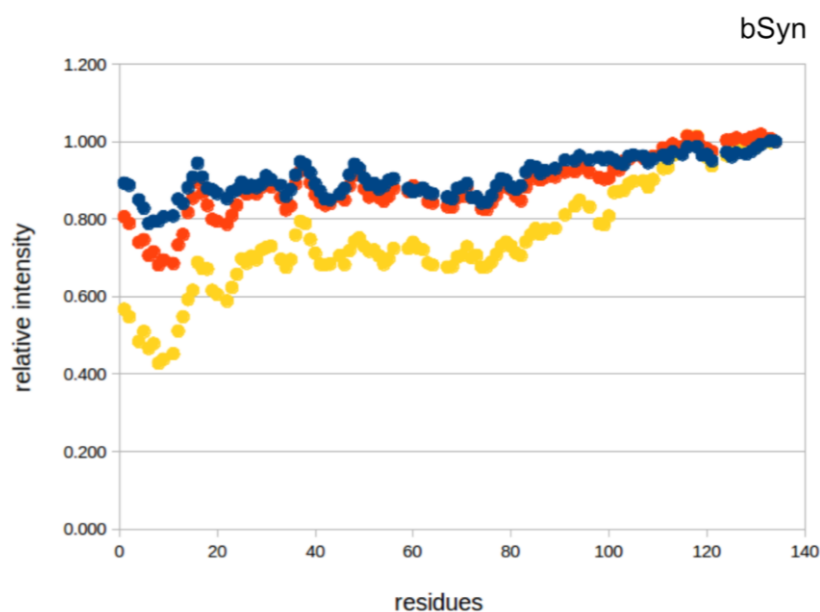
Figure 7-4. SUV titration of α- and β-synuclein by NMR spectroscopy.

(a) 100 µM aSyn and (b) 100 µM bSyn in MES buffer (20 mM MES, 100 mM NaCl, pH 6.5, 0.02 % NaN$_3$) was titrated at 25 °C with 25-fold (blue), 50-fold (red) and 100-fold (yellow) excess of SUVs, DOPE/DOPS/DOPC (5:3:12, w/w). The ^{1}H-^{15}N HSQC spectra were acquired at 600 MHz and the intensity values of free aSyn (a) as well as free bSyn (b) residues (I$_0$) were used to determine the relative intensity ratio (I/I$_0$). The relative intensity values were averaged over the residues i-1, i and i+1. The non-perturbed C-terminal A140 for aSyn and A134 for bSyn were set to 1.

7.8.2 Protein-membrane interactions by CD spectroscopy

To further characterize the binding of α- and β-synuclein to the phospholipid bilayer of SUVs, mimicking biological membranes, CD spectroscopy was chosen. The membrane bound population of α- and β-synuclein forms an α-helical conformation[32,33], while unbound populations remain intrinsically disordered. Monitoring the buildup of mean residue ellipticity (θ_{MR}) at 222 nm, due to the formation of α-helical membrane bound conformations (Figure 7-5 a), an apparent dissociation constant ($K_{D,app}$) can be derived (Figure 7-5 b) established and shown for aSyn by Pfefferkorn et al.[204]. For a quantitative analysis, the spectra do not meet the required quality. The α- and β-synuclein CD spectra (Figure 7-5 a) do not show a single isodichroic point that would indicate a two-state conformational change from intrinsically disordered to α-helical. This might be due to weak protein-lipid interactions, the DOPE/DOPS/DOPC (5:3:12, w/w) SUV system is only weakly negatively charged in its DOPS moiety, requiring high excess of SUVs (up to 700-fold). The derived values

for $K_{D,app}$ can only be used qualitatively, for aSyn a value of 10.6 mM and for bSyn a value of 9.2 mM was derived.

a

b
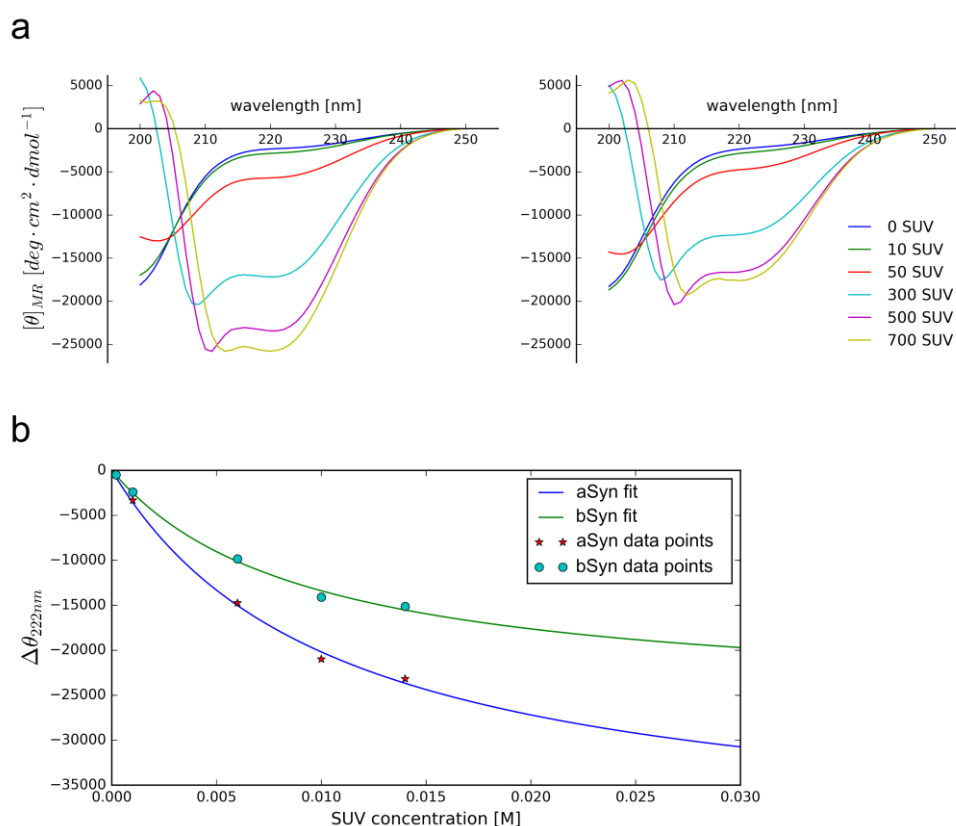
Figure 7-5. SUV titration of α- and β-synuclein by CD spectroscopy.
(a) 20 µM aSyn (left) and 20 µM bSyn (right) in low ionic strength NaP buffer (10 mM NaP, pH 6.5) were titrated at 25 °C with 10- to 700-fold excess of SUVs, DOPE/DOPS/DOPC (5:3:12, w/w). Reference spectrum in blue, 10- (green), 50- (red), 300- (cyan), 500- (purple) and 700-fold (olive). (b) The mean residue ellipticity values are plotted against the absolute SUV concentration in mol/l. The datasets were fitted as described by Pfefferkorn et al.[204]. Analysis and plotting were performed using Jupyter notebook (Python 2.7, SciPy's least-square fitting library "curve_fit"). All experiments were recorded on a JASCO J-1500 CD spectrometer.

The data obtained by NMR spectroscopy suggest that there are differences in the binding mode to this particular system of SUVs between aSyn and bSyn. The intensity decrease is more pronounced for membrane-interacting residues of aSyn than for bSyn. This might suggest a higher population of aSyn bound to SUVs. CD spectroscopy also reports less α-helical content for bSyn. Counterintuitively, the interaction of aSyn and bSyn with SUVs occur though with similar affinities. Additional experiments are required to better characterize interactions with SUVs and work out robust differences between α- and β-synuclein.